Characterization of Shape Memory Alloys via Transmission Electron Microscopy

Dissertation

zur Erlangung des akademischen Grades
Doktor der Ingenieurwissenschaften (Dr.-Ing.)

der Technischen Fakultät der Christian-Albrechts-Universität zu Kiel

Rasit Burak Erkartal

aus
Istanbul
Oktober 2013

Die vorgelegte Arbeit wurde von August 2010 bis Oktober 2013 am Institut für Materialwissenschaft in der Arbeitsgruppe Synthese und Real Struktur von Feststoffen an der Christian-Albrechts-Universität zu Kiel unter Anleitung von Herrn Professor Dr. Lorenz Kienle angefertigt.

Gutachter:
Herr Professor Dr. Lorenz Kienle
Herr Professor Dr. –Ing. Jeffrey McCord
Tag der Disputation: 11.12.2013

Contents

Abbreviation List

A°	Angstrom
ACOM	Automated Crystal Orientation Mapping
bcc	Body Centered Cubic
bct	Body Centered Tetragonal
BF	Bright Field
°C	Degree Celsius
DF	Dark Field
EDX	Energy Dispersive X-Ray
EFTEM	Energy Filtered Transmission Electron Microscopy
fcc	Face Centered Cubic
fct	Face Centered Tetragonal
FFT	Fast Fourier Transform
FIB	Focus Ion Beam
GP zone	Guinier-Preston Zone
HAADF	High Annular Angular Dark Field
HRTEM	High Resolution Transmission Electron Microscopy
K	Kelvin
LTEM	Lorentz Microscopy
M	Modulation
MBE	Molecular Beam Epitaxy
nm	Nanometer
PE	Pseudoelasticity
PED	Precession Electron Diffraction
RT	Room Temperature
SAED	Selected Area Electron Diffraction
SMA	Shape Memory Alloy
SME	Shape Memory Effect
STEM	Scanning Transmission Electron Microscopy
TEM	Transmission Electron Microscope
XRD	X-Ray Diffraction
ZA	Zone Axis
µm	Micrometer

Abstract

Shape memory alloys are a unique class of metal alloys that can recover from permanent strain when they are heated above a certain temperature. These alloys also exhibit pseudoelastic properties: they can sustain large deformations at a constant temperature and return to their original undeformed shape when the stress is released. Ferromagnetic shape memory materials can undergo similar shape changes in response to a magnetic field; however, their magnetic properties change following physical deformation by an external mechanical stress (the so-called ferromagnetic shape memory effect). These ferromagnetic materials are now used in a variety of applications, including military, medical, safety, and sensor uses. In the last decade, they have also been considered for use in ferroic cooling devices.

However, several problems have to be overcome in order to achieve high efficiency in functional devices. This thesis addresses these problems with the aid of advanced transmission electron microscopy (TEM) techniques, and explores the structure-function interrelationship of ferromagnetic shape memory materials. Two ferromagnetic shape memory alloys, $Fe_{70}Pd_{30}$ and Fe-Pd-Pt thin films, were structurally and chemically investigated at the nanoscale by TEM, including in situ measurements for evaluating specific phase transformations. Ferroic cooling systems were examined using Ni-Ti and Ni-Mn-In-Co thin films, which were selected for their high potential for use in magnetocaloric and elastocaloric devices. In situ TEM measurements were combined with ex situ studies in order to mimic the in-function status. Some TEM techniques, such as automated crystal orientation mapping and electron tomography in the scanning TEM mode, were also performed for the first time on these alloys.

The first problem addressed was how to obtain functional thin films in order to integrate them into the micro/nano systems. Currently, the magnetic shape memory effect has not been reported in thin films. These effects are only obtained in single crystalline fct bulk materials in Fe-Pd systems; this means that fully epitaxially grown $Fe_{70}Pd_{30}$ films with high thicknesses are required. Single variant fct thick films were obtained by sputtering $Fe_{70}Pd_{30}$ alloys on (100)-oriented substrates with different buffer layers (Au, Mn-Ir, Ir-Rh, and Ir). Films prepared on an Au buffer layer without any adhesion promoting layer were polycrystalline and bcc type. The use of a Cr adhesion promoter resulted in a <110> bcc texture of the sputtered film. Changing the sputtering parameters (i.e., selecting lower sputtering rates) created an artificial, single variant bct martensitic state, reported here for the first time. The tetragonal distortion of the bct unit cell was 7%. This experiment was repeated using a

similar approach, but with different metallic buffer layers with various lattice parameters close to those of the desired fct phase of $Fe_{70}Pd_{30}$. Buffer layers consisting of $Mn_{80}Ir_{20}$, Rh, or Cr, gave similar results: The films grew to a limited thickness with a bct structure and all films relaxed to a polycrystalline bcc structure. The relaxation mechanism in all films was a misfit dislocation. Only the Ir buffer layer yielded the desired fct phase, although, with a very limited thickness (100 nm). Films were also produced with a Fe-Pd-Pt system by combinatorial material development, and the formation of complete ternary phases was investigated using TEM. A completely ternary region was found which exhibited an fcc structure. In situ cooling of the sample also resulted in successful fcc-fct transformation. These films also showed diffuse scattering similar to that seen in the $Fe_{70}Pd_{30}$ films, indicating a premartensitic phase.

Effective magnetocaloric thin films were identified via investigations of 300 nm thick magnetocaloric Ni-Mn-In-Co films by TEM. Different regions with dissimilar structures and chemistry were observed. Modulated (i.e., nanotwinned) structures with different stacking periodicities (i.e., 5M, 6M, 7M, and 8M) coexisted with non-modulated structures that were twinned on a larger (microscopic) scale. The Cr of the adhesion layer was diffused into the functional layer, so that In was replaced in some spatially confined regions by Cr and Co, compared to the neighboring Cr-free regions.

Cycled and uncycled Ni-Ti and Ni-Ti-Cu alloys were compared in the case of elastocaloric thin films. Binary elastocaloric Ni-Ti thin films had a microstructure consisting of Ni_4Ti_3 precipitates and an R-Phase. The size of the precipitates was determined by electron tomography techniques and tilting. The length of the austenitic grains was measured at several micrometers. Deformation of the austenitic matrix was observed after mechanical cycling of the specimen ex situ. This led to an incomplete transformation from austenite to martensite during cycling, resulting in a low fatigue endurance that made these alloys unsuitable for functional caloric devices. On the other hand, the metals exhibiting a grain size of more than 1 µm showed that an increase in grain size generally resulted in a reduction in the fatigue endurance limit. The most common size and volume of the Ni_4Ti_3 precipitates were determined using various techniques. Tilting the sample to a different zone axis allowed determination of the average distribution of the precipitates. The results were verified by electron tomography measurements.

Ternary Ni-Ti-Cu films, unlike the binary alloys, showed stable mechanical cycles, as well as a temperature change of 5 K. These positive characteristics of caloric devices were correlated with the microstructure. TEM investigations showed that the grain sizes of the ternary phase films were significantly smaller than were those of Ni-Ti films. Mechanical

cycling caused no significant changes in the microstructure. Small grain sizes minimized the generation of dislocations inside the grains. These dislocations are introduced during the cycling, and accumulate at the highly energetic grain boundaries. The density of the newly introduced dislocations decreased and the glide movement of the grains was enhanced by smaller grain sizes; thus, the number of stable mechanical cycles was increased.

These results are encouraging for achieving SME in $Fe_{70}Pd_{30}$ thin films, and for fabricating functional caloric devices based on magnetic or elastic responses.

MOTIVATION

Shape memory alloys (SMAs) have unique characteristics such as pseudoelasticity and the ability to regain their original shapes by heating after initial deformations. These effects were first reported by Otsuka and Wayman[1] in 1930 and Ölander[2,3] in 1932, but serious research was only undertaken in the early 1960s. Alloys in this category that are in wide use include Ni-Ti, Cu-Zn-Al, and Cu-Al-Ni. The principle of these shape memory effects is described in more detail in the following chapter.

In the last decade, the use of these alloys was envisaged for the fabrication of ferroic cooling systems, since the structural changes during the shape memory/pseudoelastic transitions are related to entropy changes[4]. The entropy change in Ni-Ti based shape memory alloys leads to a temperature change in their environment, due to the loading and unloading of the material – the so called elastocaloric effect. However, scientific research regarding this phenomenon is lacking. The present study investigated the structural/compositional characteristics of Ni-Ti SMA thin films, and found a slight temperature change (5 K) after mechanical cycling, which was subsequently related to the caloric function of those alloys. Microstructural changes were monitored and were compared before and after the mechanical cycling processes. Although Ni-Ti is a well-known system in electron microscopy, some of the techniques were applied to these alloys for the first time, for example, automatic texture measurements (ACOM) and electron tomography, and are of importance to the fundamental research.

An adiabatic temperature change, defined by the heating or cooling of magnetic materials due to the application of a magnetic field, is called a magnetocaloric effect[5]. Recently, Heusler-type Ni–Mn–(In, Sn, and Sb)-based magnetic shape-memory alloys have been proposed as solid-state energy-efficient refrigerants, owing to their remarkable first-order transition feature[6,7]. However, application of the concept of shape memory and magnetocaloric effects to micro/nanosystem technology requires epitaxial thin films with a high surface to volume ratio in order to provide the desired fast heat transport. The absence of grain boundaries also enhances heat transport. In the present study, we focused on the metamagnetic Ni-Mn-In-Co system, since the strong differences in the magnetization of austenite and martensite allow for field induced actuation with high forces and an immense magnetocaloric effect[8]. This film also exhibits magnetocaloric properties at room temperature[9]. The TEM analyses were focused on the different microstructures and their dependence on film composition. The combination of spatial confinement and the presence of nanoscale structural and chemical features like domains and precipitates, also required

electron microscopy techniques for identification and characterization at close to atomic resolution.

Another focus of the thesis was the characterization of so-called ferromagnetic shape memory alloys (FSMAs) via transmission electron microscopy (TEM). These ferromagnetic materials exhibit large strains under the influence of an applied magnetic field[10]. $Fe_{70}Pd_{30}$ alloys are one of the best materials known, showing ferromagnetic shape memory behavior in the bulk state[11]; however, this effect has not been previously observed in thin films (Note: thin films are required for the integration of these alloys into micro/nanosystem technology). The TEM investigations were carried out after sputtering the thin films on sacrificial buffer layers. The choice of buffer layer can lead to a distortion of the $Fe_{70}Pd_{30}$ unit cell. The variation of the in-plane lattice parameters of the buffer layers (ranging from Rh to Cr) also caused epitaxial growth of the $Fe_{70}Pd_{30}$ martensites with different c/a ratios, which were stable at higher thicknesses. Therefore, interface analyses and structural details along the growth direction of the film were monitored in order to obtain functional (fct-phase) freestanding $Fe_{70}Pd_{30}$ thin films (see section 1.1 for details).

However, despite their superior microstructure, epitaxial films exhibit disadvantages, such as the use of costly substrates, the requirement for heating during deposition, more complicated fabrication, limited film thicknesses, and significantly lower deposition rates. In this regard, polycrystalline films are preferable as inexpensive amorphous Si substrates without any need for heating. Therefore, this study examined the effect of different heat treatments on sputtered films for the fabrication of polycrystalline films with an optimized microstructure for magnetic shape memory actuation. In situ heating experiments were performed in order to study the intermediate phases occurring during the bcc-fcc transformation.

PART I

1. $Fe_{70}Pd_{30}$ Ferromagnetic Shape Memory Thin Films

1.0 Vocabulary: Shape Memory Alloys

Shape memory alloys (SMAs) are a unique class of metals that can “remember” their original shapes after initial deformation. They undergo a change of metric (by a transition of the unit cell) at a certain temperature called the transformation temperature. Above this temperature, the material exhibits a highly symmetric crystal structure, while below this temperature it undergoes a martensitic transformation. It is the low temperature structure of these types of materials that allows the severe deformations. However, heating restores the material to its high temperature structure, which has only one possible shape – the original highly symmetric crystal. Thus, the material “remembers” its shape.

These two stable phases of SMAs are referred to as: 1) the high-temperature phase, called **austenite** and 2) the low-temperature phase, called **martensite**. The **martensite** phase can exist in one of two states: **twinned** and **detwinned**. The common effects related to the SMA phase transformation are **pseudoelasticity** and the **shape memory effect**.

SMA materials transform from austenite into self-accommodated twinned martensite when cooled in the absence of an applied load. These twins are aligned by the same twin law, and are accommodated in parallel as so-called polysynthetic twins. Heating a material with the martensitic phase causes a reverse phase transformation, and the material transforms to austenite. This process is schematized in Figure 1.

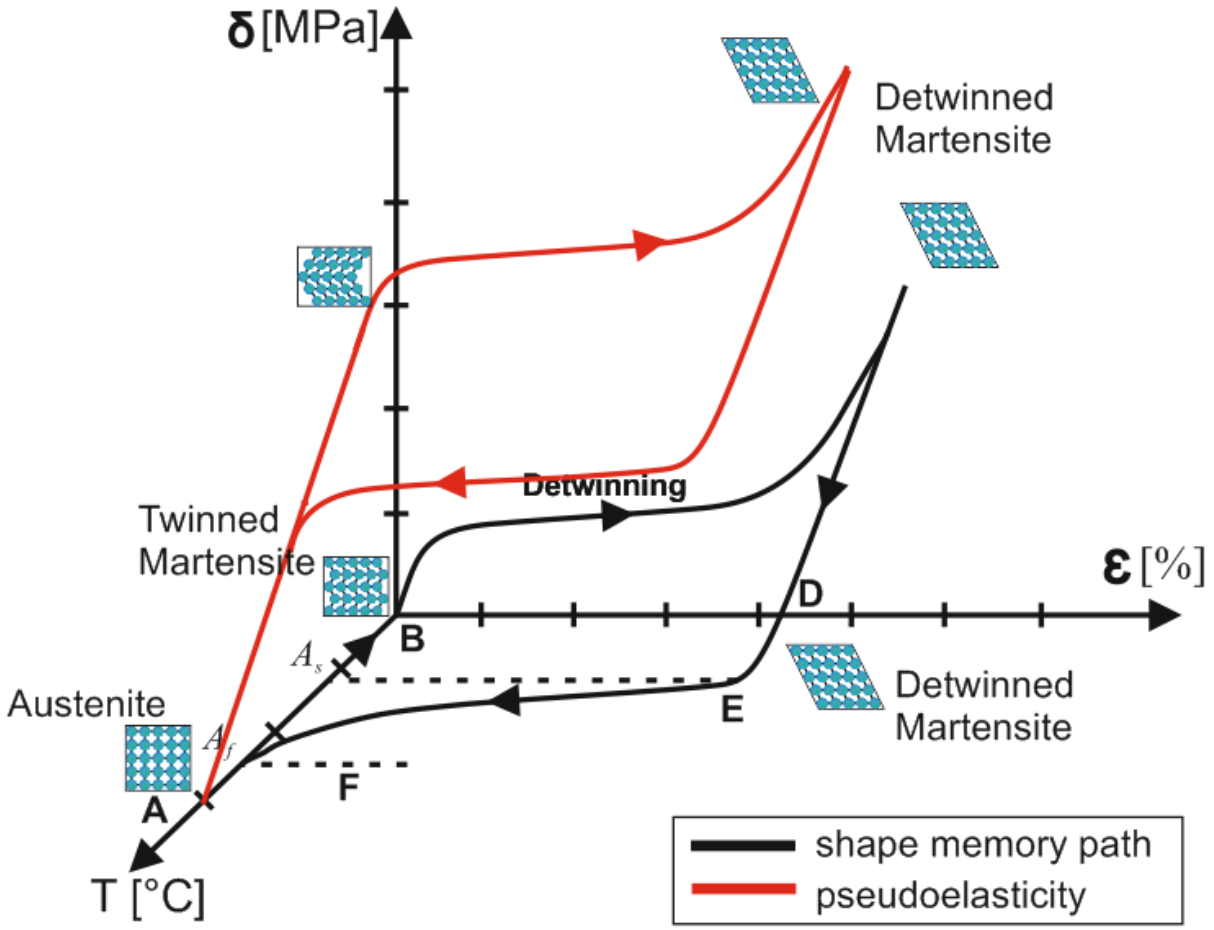

Figure 1: Schematic depiction of possible states occurring during shape memory (black) and pseudoelastic (red) transitions[12].

Four characteristic temperatures are defined in Figure 1:

- **martensitic start temperature (M^s):** the temperature at which the material starts transforming from austenite to martensite
- **martensitic finish temperature (M^f):** the temperature at which the material is entirely martensitic and the transformation is completed
- **austenite start temperature (A^s):** the temperature at which the reverse transformation (austenite to martensite) initiates and
- **austenite finish temperature (A^f):** the temperature at which the material is entirely austenitic and the reverse phase transformation is completed.

Application of a mechanical load to a material in the state of twinned martensite (at low temperatures) can cause detwinning. In this case, the material remains deformed when the load is released. As shown in Figure 1, a subsequent heating of the material to a temperature above A^f will result in the reverse phase transformation (martensite to austenite), and a complete shape recovery. This process results in the expression of the **shape memory effect (SME)**.

A martensitic transformation that leads directly to detwinned martensite can also be induced if the material is cooled and a load is applied in the austenitic phase. In this case, the phase transformation will result in detwinned martensite and very large strains (in the order of 5-8%) will be observed. Reheating the material again results in complete shape recovery (black labeled path). Note that in this case, the transformation temperatures are strongly dependent on the magnitude of the applied load. Applied loads that are larger will lead to higher values for the transformation temperatures.

Application of a purely mechanical load can also induce a phase transformation. The result of this load application is fully detwinned martensite, and very large strains are observed. Unlike the twins occurring in the shape memory path, these twins are not polysynthetic: they occur by a onetime shear process. The unit cell shears and no repetitive behavior of the twins is observed in the microstructure. If the temperature of the material is above A^f, a complete shape recovery occurs upon unloading. This behavior resembles elasticity (red labeled path), and the effect is referred to as the **pseudoelastic effect (or superelasticity)**.

The microstructure of martensitic materials is shaped by differently oriented domains (martensitic variants). These variants can be also internally modulated with different propagation lengths, such as 5M or 7M modulations and are interconnected by twin boundaries Ferromagnetic forms of these materials usually have a specific crystallographic direction favorable for the magnetization (the so-called **easy axis**). **Magnetically induced reorientation** (**MIR**) can occur when the twin boundaries are easily moveable and are not pinned; hence, an external magnetic field can move those boundaries, leading to changes in microstructure and external shape.

The potential applications for SMAs, particularly as actuators and sensors, have widened the spectrum of scientific interest in these materials.

1.1 $Fe_{70}Pd_{30}$ Ferromagnetic Shape Memory Alloys

The Fe-Pd system is the first system that is examined in this thesis.

$Fe_{70}Pd_{30}$ has several advantages for particular applications, especially because of its high ductility and the orientation of its easy axis of magnetization along the long c-axis of the martensite. The growth direction of the film can be adjusted, which allows the use of an out-of-plane magnetic field in a thin-film-actuator[13]. Systematic studies of Fe-Pd bulk properties[14] have already been conducted, but Fe-Pd thin films with a $Fe_{70}Pd_{30}$ composition remain to be investigated more fully.

The thermal equilibrium phase diagram for this composition indicates that the disordered fcc phase austenite is only stable above 800 °C. At lower temperatures, the system demixes into the stable, ordered $L1_0$ phase ($Fe_{50}Pd_{50}$) and the stable, iron rich bcc Fe-Pd (Fe 50-60 at%.) solid solution. However, when the Fe-Pd is rapidly quenched from the austenite region, this arrangement of atoms and decomposition can be kinetically suppressed [15]. Metastable phases, which have been investigated in detail in bulk single crystals, occur under these non-equilibrium conditions. The metastable phases observable at room temperature with decreasing Pd content are: fcc austenite, fct and bct martensite, and the bcc phase (Figure 2).

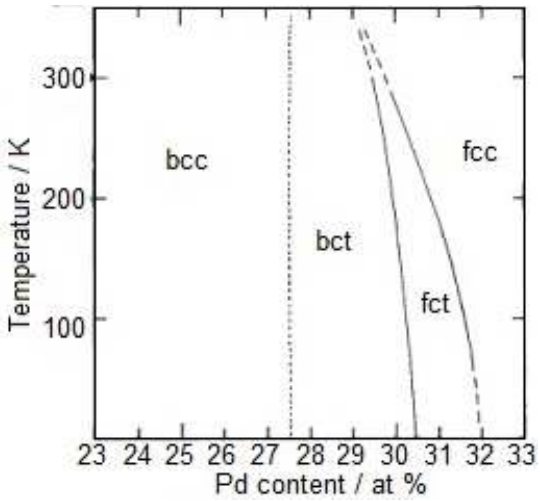

Figure 2: Phase diagram of bulk Fe-Pd[16].

The MSM effect occurs in the fct martensite phase. The metastable phase diagrams indicate that the fct martensite forms out of the fcc phase during cooling[17,14]. The stability region of the fct martensite in bulk material is very narrow, and is limited by the bct martensitic phase that forms at lower temperatures[18]. The martensite start temperature T_M of the fcc-fct transition strongly increases with the decreasing Pd content [19]. The same applies for the intermartensitic transition fct-bct (fct martensite is only observed between 29.3 and 29.7 at% Pd at room temperature)[20]. Rapid quenching, however, results in an expansion of the fct stability region to as much as 28–33 at% Pd, which indicates that a stabilization of the fct martensite by higher quenching rates might be possible[21].

Buschbeck et al. examined the epitaxial growth of Fe-Pd at room temperature and its limits (critical thickness) with the aid of XRD[22]. Epitaxial growth formed single crystalline films; thus, the structure and physical properties could be studied more precisely than could those of polycrystalline films. The composition range of the fct martensite was broader in thin films (50 nm) than in the bulk material, which was attributed to stabilization by the compressive film stress. Epitaxial growth was observed through the whole composition range due to martensite instability, which allowed for the accommodation of large misfit dislocations for

relaxation[23]. In thicker films, $(111)_{fcc}$ twinning was a second notable mechanism for relaxing stress.

Buschbeck et al. also presented an approach for achieving high strains in thicker films by using materials with inherent structural instabilities. They investigated $Fe_{70}Pd_{30}$ films on various 50 nm thick epitaxial buffer layers, where strained coherent growth on various substrates makes it possible to adjust the tetragonal distortion of the c/a ratio from 1.09 to 1.39 in the bct structure, covering most of the Bain transformation path[24]. This novel idea inspired the deposition of martensite directly onto a single crystalline substrate[25].

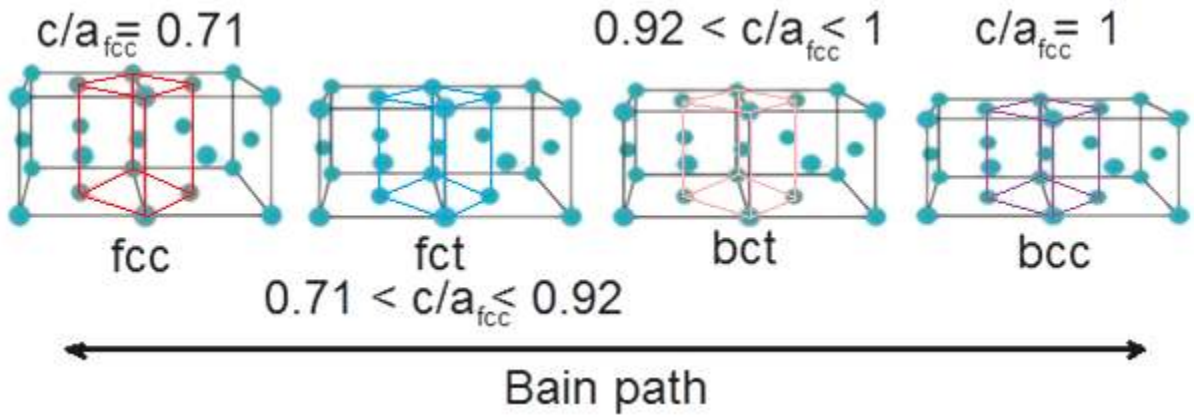

Figure 3: Schematic illustration of the phase transformation in $Fe_{70}Pd_{30}$ alloys. The transformation follows the Bain path, and the phase can be determined by the c/a_{fcc} ratio.

The Bain transformation can be illustrated by considering two neighboring fcc unit cells (indicated in blue in Figure 3). One bct unit cell can be introduced at the border of these two fcc cells, with a and b axes rotated 45° with respect to those of the fcc structure. This new bct unit can describe the fcc structure, and the tetragonal distortion can be calculated to c/a_{bct} = 1.41 (by simply taking √2 times the a_{fcc} parameter). The phase transformation c/a_{bct} ratio, following the Bain path, changes continuously from 1.41 to 1. The same ratio can be described for the a_{fcc} parameter, where the c/a_{fcc} ratio continuously changes from 1 (c_{fcc}/a_{fcc}) to 0.71 for the bcc structure (Figure 3). The conversion between these two settings can be made by $a/a_{bct} = \sqrt{2}c/a_{fcc}$.

2. METHODOLOGY

2.0 Experimental Techniques

This section briefly presents the experimental details for standard TEM characterization methods, such as high resolution TEM (HRTEM) imaging, scanning TEM (STEM), energy filtered TEM (EFTEM), and Energy Dispersive X-ray (EDX) spectroscopy. Project specific techniques, like automated texture measurements (ACOM), geometric phase analyses (GPAs), and precession electron diffraction (PED) are discussed in more detail.

2.1 Transmission Electron Microscopy (TEM)

TEM enables an almost complete characterization of inorganic materials, due to its capability for resolution in real space, nanofocusing, and the combination of these techniques in one instrument. Today's TEMs are the most versatile and efficient tools in materials science, with ranges extending from the micro scale down to the atomic scale. The experiments performed in this thesis were conducted using three different electron microscopes:

- **Tecnai F30 G^2 S-TWIN:** TEM Center at the Kieler Nanolab in CAU, Kaiser Strasse 2, 24143 Kiel
- **Tecnai F20 G^2:** Karlsruhe Institute of Technology, Karlsruhe Nano Mikro Facility, Hermann-von-Helmholtz-Platz,176344 Eggenstein-Leopoldshafen, Karlsruhe
- **Philips CM30 ST:** Max-Planck-Institute for Solid State Research, Nanochemistry Department, Heisenberg Straße 2, 70569, Stuttgart

The d-values (and the corresponding lattice parameters) were calculated using the Digital Microscope 3.6.1 program and were compared with values from the Inorganic Crystal Structure Database (ICSD)[26].

The following section briefly describes the main principles of some of the TEM techniques used in this research. More information on separate features can be obtained from the text book (Transmission Electron Microscopy- A textbook for materials science) by D. B. Williams and B. Carter[27].

- **HRTEM** allows the imaging of the crystallographic structure of a sample at an atomic scale[28]. The image is formed by the interference of the diffracted beams with the direct

beam (phase contrast). In many cases, the atomic structure of a specimen can be directly investigated by HRTEM. Image interpretation is performed via an iterative procedure by comparing simulated images with images acquired by the electron microscope. An average background subtraction filtering (**ABSF**) step is also applied for better contrast[29]. The Fourier transform of the original image is calculated and the power spectrum through the histogram is analyzed in order to estimate the magnitude of the noise in the image when using this filtering technique.

- **STEM** is a valuable tool for the characterization of nanostructures[30]. It offers a range of different imaging modes, with the ability to provide information on structural information and elemental composition. In this mode, the condenser lens system of the microscope is used to focus a small electron probe (around 1 nm in diameter) on the sample. Scan coils raster the probe across the sample, and the scattered electrons are collected by a high angle annular dark field (HAADF)-detector, which minimizes the diffraction and maximizes the atomic number (Z) contrast.

- Energy dispersive X-ray (**EDX)** analysis relies on the interaction of the specimen with the incident electron beam, which generates X-rays. The energies of the emitted X-rays are characteristic for each element. Measurement of the spectra determines the compositional variation at the nano-scale[31].

- Electron diffraction **(ED)** allows crystallographic characterization of solid structures using TEM[32]. In particular, the nature of defects can be understood from the ED patterns obtained from a selected area **(SAED)**.

2.2 Precession Electron Diffraction (PED)

Precession electron diffraction (PED) is a powerful method for improving the quality of electron diffraction data obtained from bulk crystals. X-ray diffraction is typically used to acquire intensities in bulk structure studies, a method that provides high quality datasets. High quality intensities are required for the method to work reliably.

Electron diffraction offers some advantages over X-ray methods, especially in terms of stronger scattering/interaction and spatial resolution (the ability to focus on smaller regions), which allows the study of the structure of very small crystals. However, multiple scattering (dynamical diffraction) degrades the quality of intensities from bulk electron diffraction so that atomic structures cannot be reliably resolved. Most of the standard programs work only with

the kinematical theory and overlook the forbidden reflections, which complicates space group determination. The PED[33] technique uses beam deflection prior to interaction with the specimen, in order to form tilted illumination conditions. After interaction with the sample, the diffracted beams are again deflected, using a complementary de-scan (de-tilt). Serial application of this tilt/de-tilt forms a hollow cone of illumination at the image plane, and a diffraction pattern occurs at the back focal plane, as shown in Figure 4. The pattern exhibits scattering intensity from the crystals that is more reliable, because the continuous tilting of the beam minimizes multiple scattering.

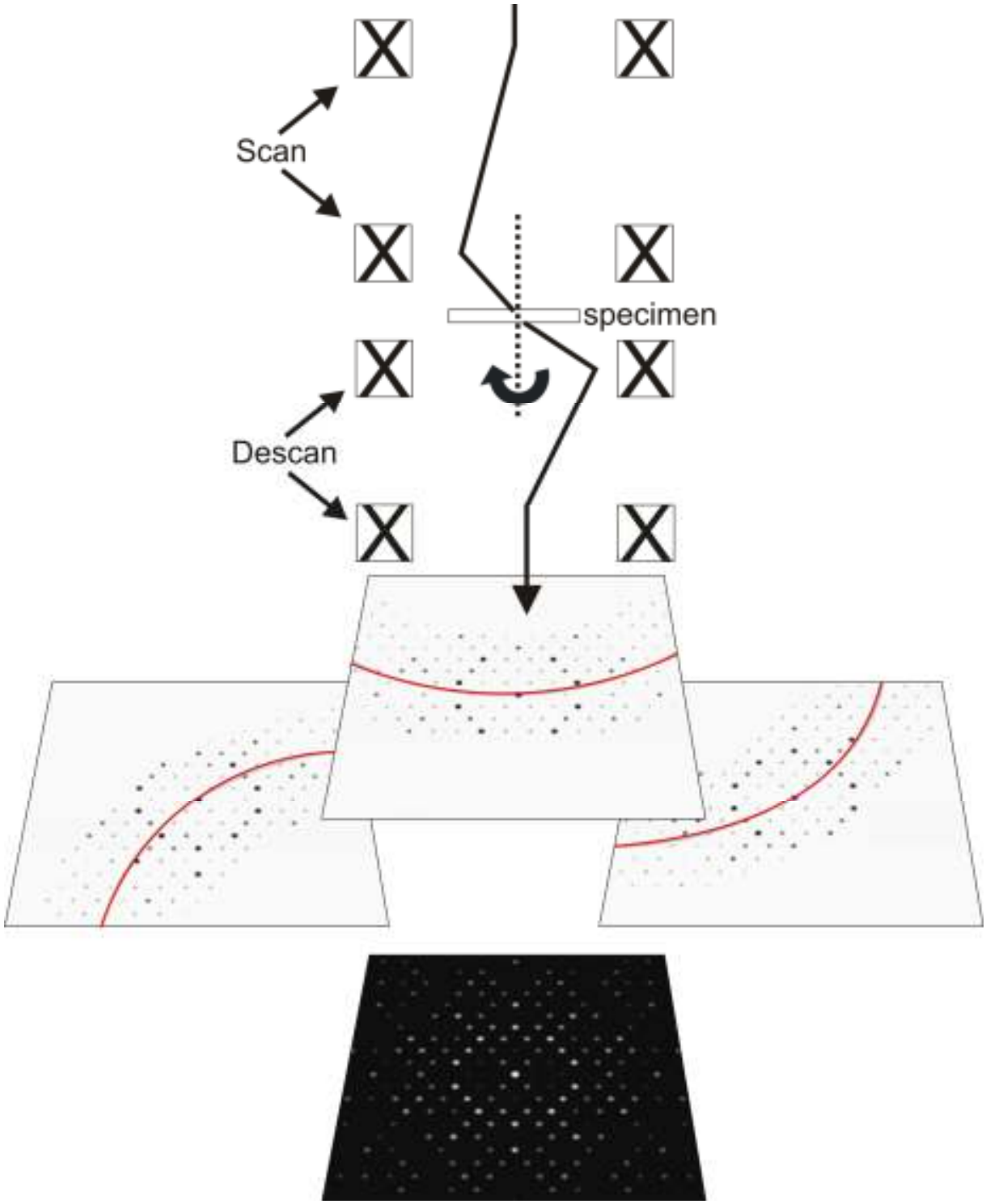

Figure 4: Ray diagram and the pattern formation in precession electron diffraction mode. With precession electron diffraction, kinematically forbidden reflection intensity and multiple scattering are greatly reduced, making space group identification easier, as well as reducing the sensitivity of ED intensities to crystal thickness and misorientation effects.

The $NiTi_2$ phase in the [101] zone axis is demonstrated in Figure 5. The intensity distribution obtained in the PED pattern recorded on the $NiTi_2$ phase agrees well with the calculated/simulated diffraction pattern.

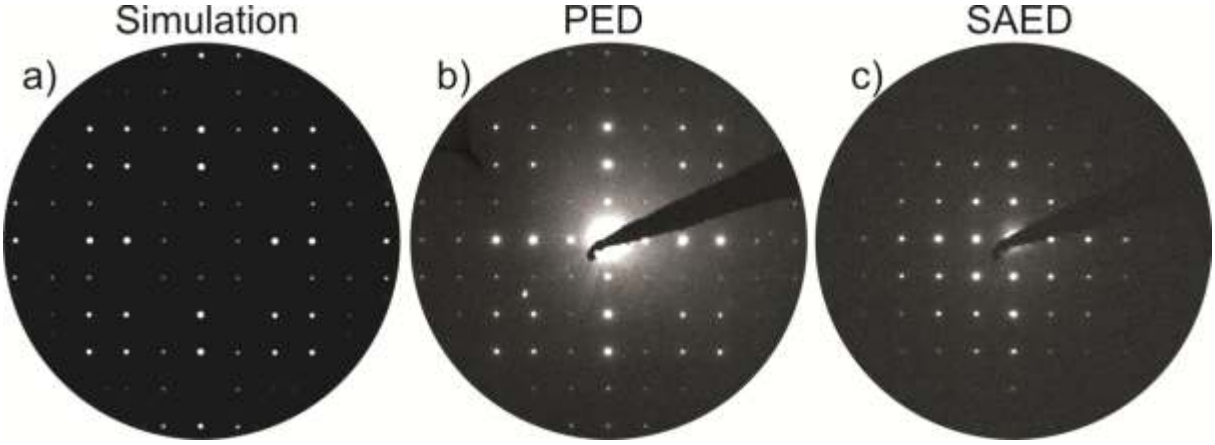

Figure 5: a) Kinematical simulation, b) PED, and c) SAED patterns recorded on $NiTi_2$ phase in [100] direction. The PED pattern is in very good agreement with the simulation, and resembles the patterns which obey the kinematic approximation.

2.3 Automated Crystal Orientation Mapping (ACOM)

The ASTAR equipment (Automatic Crystal Orientation and Phase Mapping package for TEM) delivered by Nanomegas generates orientation mappings of crystalline materials by collecting local diffraction patterns[34]. The limitation of spatial resolution of the orientation imaging via electron backscattered diffraction (EBSD) analysis in the scanning electron microscope (SEM) creates difficulties when investigating the microstructure of nanocrystalline materials. The use of the recently developed transmission electron microscope based technique[35] known as ACOM, offers the possibility of reliable orientation mapping with a spatial resolution of 5 nm. In ACOM, a nanoprobe electron beam is scanned over the specimen, and spot diffraction patterns are collected with a dedicated CCD camera mounted in front of the TEM screen. Individual spot ED patterns are compared with simulated patterns for all possible orientations via cross-correlation. This technique is valuable for the study of chemically and structurally inhomogeneous thin film materials. A proof of the principle is shown in Figure 6.

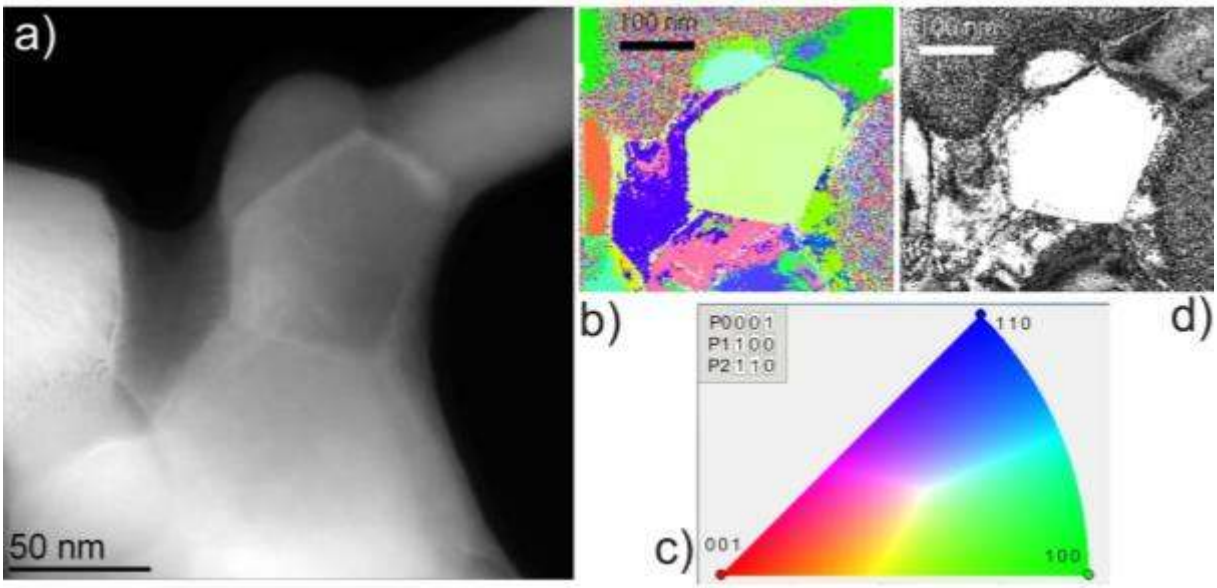

Figure 6: a) HAADF-STEM image of a Ni-Ti-Cu alloy with several grains; b) ACOM map on a section of this region with the colors defined in the color-coding in c); d) reliability map of the same section, with high reliability shown in the bright areas.

Figure 6a depicts the HAADF-STEM image of the studied region. Figure 6b displays the orientation map for the region, with the color coding for the different orientations shown in Figure 6c. The reliability map (Figure 6d) reveals that the collected diffraction pattern in some regions matches very well with the simulation of the $CuTi_2$ phase (bright = good matching, dark = weak matching). Other regions of the sample, as well as the regions without sample, show poor reliability. The sample material contains no $CuTi_2$ and no other phase matching was successful.

2.4 Geometric Phase Analyses (GPA)

Geometric phase analysis is a simple and efficient method for measuring relative strain. Nearly periodic images, particularly high resolution transmission electron microscopy (HRTEM) images, are analyzed[36]. In a few steps, GPA averages and fits the best lattice parameter in a given region. This method allows analysis of the variations from an ideal structure. The displacement of the lattice fringes are determined directly via the phase images, and can be used to measure the local reciprocal lattice vector.

Strong Bragg peaks are characteristic of the HRTEM lattice or structure images from crystalline materials. The location of a peak corresponds to the periodicity and orientation of the fringes in the image, while the phase of the Bragg peak corresponds to the location of the fringes in the image. Selection of an asymmetric region of the Fourier transform gives directional information. In the absence of lattice distortions, the phase corresponding to any reciprocal lattice vector **g** will be constant across the image. Lateral shifts of the fringes can

therefore be seen as changes in the phase image that correspond to **g**. The sensitivity of the technique to lattice distortions depends on the resolution of the image. Consequently, Cs corrected microscopes are advantageous for calculating these types of strain maps. The specific steps are:

1. Calculate the full-plane Fourier transform
2. Select the region around the particular reciprocal lattice vector of interest in the Fourier transform
3. Inverse transform the filtered Fourier spectrum to obtain a complex image
4. Subtract from this raw phase image a phase ramp image corresponding to the selected **g** vector.

The resulting phase image is a map of the deviations from regular periodicity in the image and can be used to obtain a strain map after suitable scaling. An example of this specific technique is given in Figure 7.

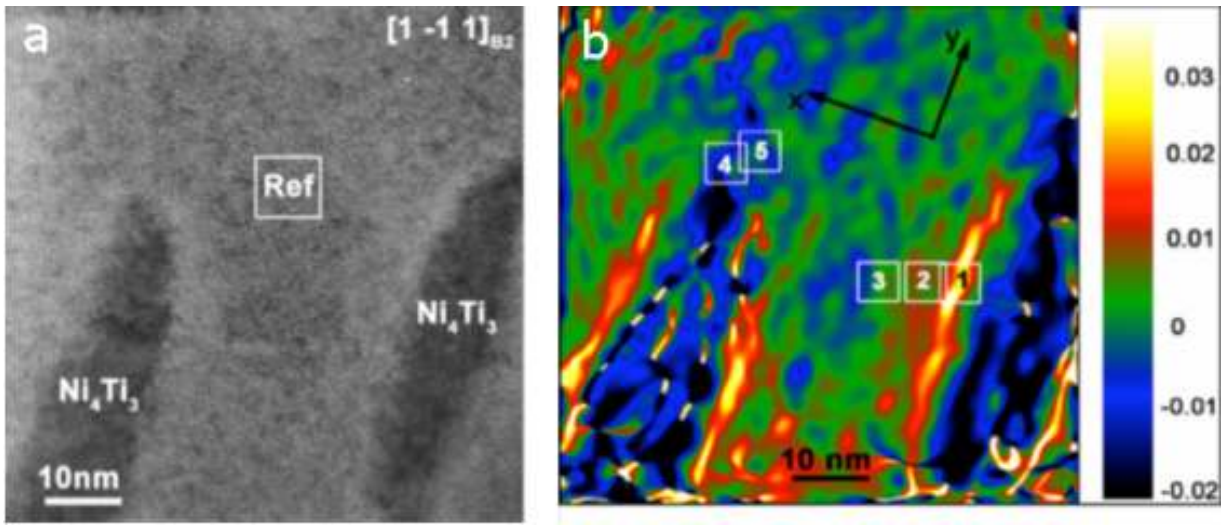

Figure 7: a) Observation of Ni_4Ti_3 precipitates in a $[1\text{-}11]_A$ [1] zone orientation b) plot of the ε_{xx} component obtained by GPA. x // $[121]_A$, y // $[10\text{-}1]_A$.

Schryvers et al. investigated these strain fields quantitatively for the case of bulk materials[37]. Figure 7a depicts a bright field TEM image showing the Ni_4Ti_3 precipitates in an austenitic matrix. The lattice mismatch introduced by the higher Ni content in the precipitates creates strain fields around the precipitates. Two different strain phenomena can be recognized in the GPA map shown in Figure 7b. The edges of the precipitates appear red in the calculated GPA map, showing a tensile stress in that direction ($[121]_A$). On the other hand, the tips of the precipitates appear blue, indicating a compressive strain ($[10\text{-}1]_A$). These local strains are expected to influence the local transformation temperatures, since they are elastic in nature (the presence of tensile and compressive stress in perpendicular directions).

[1] Subindex A stands for the austenitic cell settings in Ni-Ti alloys.

2.5 Specimen Preparation Techniques

The preparation of electron transparent samples sounds routine, and is perceived as being straightforward by scientists. However, it is the first and arguably the most crucial part of analysis. The three techniques used in this work are compared in the following section.

- **Focused Ion Beam (FIB)**

The Focused Ion Beam (FIB) system uses a Ga^+ ion beam to raster over the surface of a sample, in a similar way to the passing of the electron beam in a scanning electron microscope (SEM). The generated secondary electrons (or ions) are collected to form an image of the surface of the sample. The ion beam allows the milling of small holes in the sample at well localized sites, so that cross-sectional images of the structure can be obtained, or to indicate where modifications can be made in the structure. An example is shown in Figure 8, for the case of a $Fe_{70}Pd_{30}$ sample. After selecting the area of interest, a Pt protection layer is deposited, (Figure 8a). A cross sectional region is also cut stepwise from both sides of the selected area. Subsequently, the specimen is thinned via Ga^+ ions and is mounted onto the TEM grid (Figure 8a–d).

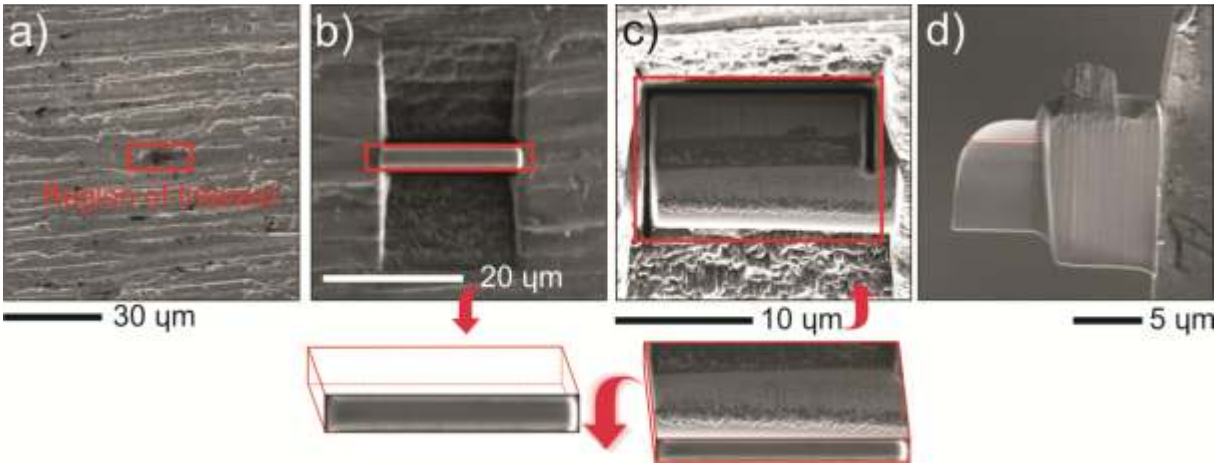

Figure 8: The four steps involved in the focused ion beam (FIB) cross-sectional specimen preparation for TEM investigations. a) The selection of the region of interest and the deposition of a Pt protection layer. b) Stepwise cutting of the edges of the specimen while rotating the sample stage. c) Final thinning of the specimen with Ga^+ ions. d) Mounting the specimen onto the TEM grid. The method is a so-called lift-out method.

This is a fast method; however, the high voltage and strong current of the ion beam can cause several artifact issues, such as surface roughness, deep ion implantation, amorphization, temperature rises, and undesired alterations in the recorded data.

- **Twin Jet Polishing**

Jet electropolishing is accomplished by pumping a stream of negatively charged electrolytes against the surface of a positively charged sample. This process is used to create a dished or dimpled area, and is continued until perforation of the specimen occurs, when the operation is automatically terminated. This technique can only be applied to conducting materials. Difficulties arise in the choice of electrolytic bath composition, voltage, current, and temperature settings. Investigation of Ni-Ti alloys uses an operating voltage of 18 V with an applied current of 60 mA at -20 °C. The electrolyte is a mixture of 95% acetic acid and 5% perchloric acid. A comparison of different preparation methods is depicted in Figure 9. The same Ni-Ti-Cu sample is prepared using two different techniques. The FIB preparation uses thicker samples, which restricts high resolution imaging. The jet polished samples produce thinner samples; however, selective etching is observed for the ternary Ni-Ti-Cu alloys. Hence, twin jet polishing was the method of choice for binary Ni-Ti alloys, whereas FIB was required for ternary Ni-Ti-Cu alloys, in order to prevent perforation of the specimens. In the last decade, very thin Ni-Ti binary thin films have also been achieved with the FIB technique by avoiding preferential etching by using a very low extraction voltage (2kV)[38].

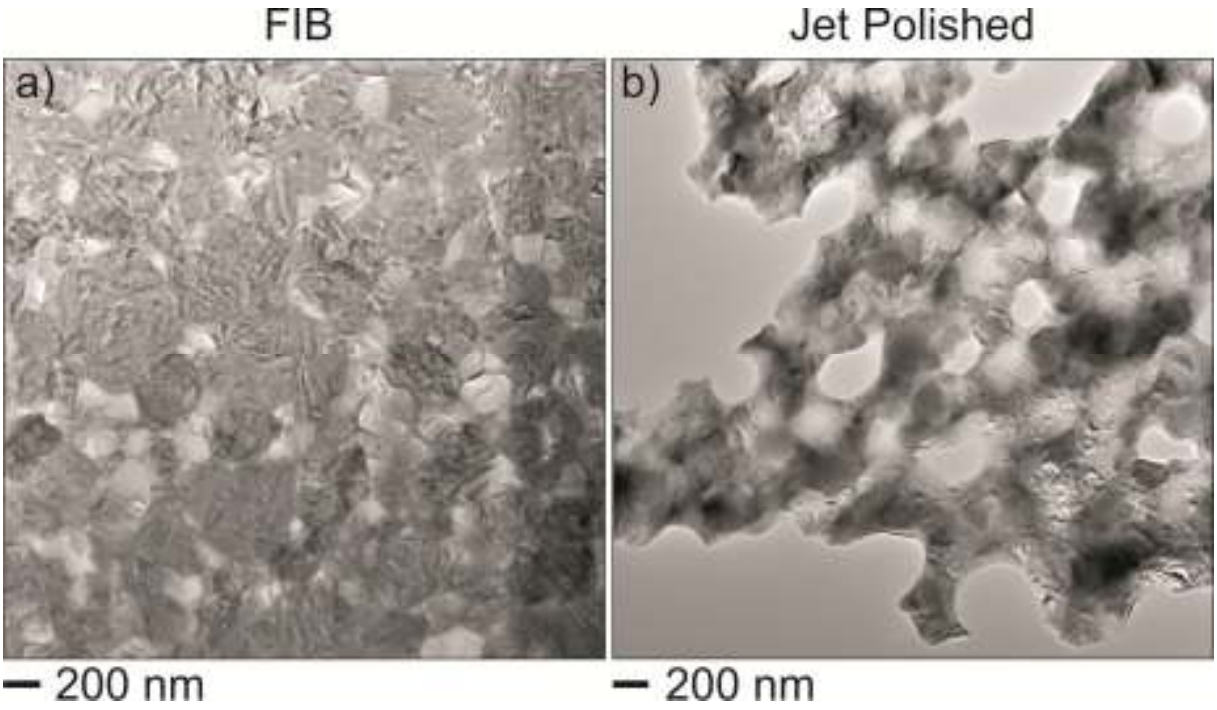

Figure 9: Ni-Ti-Cu specimens prepared by two different techniques. The specimen prepared by FIB (a) is quite thick compared to the jet polished sample (b). However, selective etching occurred during jet polishing.

- **Low Dose Ion Polishing (precision ion polishing system - PIPS)**

This technique is based on abrasion by ion bombardment. The interaction of an accelerated ion beam with the specimen causes the removal of surface atoms, leading to relief polishing and to suppression of the possible mechanical damage introduced during the preparation. Ion beam thinning can be used to plane longitudinal or cross sections, and to create wedges. All types of compact single-phase or multiphase materials can be ion thinned. Porous materials or materials consisting of multiple pieces must be impregnated or embedded beforehand. This method was first used on polycrystalline Fe-Pd samples on Si substrates; however, the large volume of these magnetic specimens caused the samples to be sucked into the objective lens of TEM and to be stacked on the pole piece. This technique was therefore avoided in the subsequent research.

3.0 RESULTS

The highest mobility of the twin boundaries, and thus the most pronounced shape memory effect, is achieved with single crystalline materials. Therefore, coherent growth of epitaxial films is required for the integration of these materials into microsystem technology. For this purpose, $Fe_{70}Pd_{30}$ was deposited by magnetron sputtering onto substrates coated with different metallic buffer layers, in order to obtain a variable degree of tetragonal distortion of the body centered martensite $Fe_{70}Pd_{30}$ unit cell. We collaborated with the research groups under Prof. Quandt from CAU Kiel and Dr. Fähler from IFW Dresden for the preparation of the multilayers. Multilayers containing Au, $Mn_{80}Ir_{20}$, and Rh were prepared at CAU Kiel, while an Ir containing a heterostructure was sputtered at IFW Dresden. Varying the in-plane parameter of the buffer layer was expected to affect the growth behavior of the $Fe_{70}Pd_{30}$ film. Note that an MSM effect is only observed in the fct phase, and the main goal of the research was to obtain this phase at a high thickness.

We focused on TEM investigations of epitaxial films grown on MgO (100) substrates. Cr, Au, $Mn_{80}Ir_{20}$, Ir, and Rh metallic films were used as buffer layers. A particular focus of the analysis was the $Fe_{70}Pd_{30}$-buffer interface, since it directly affects the growth behavior of the films and thus the functional properties.

Another focus of the research was polycrystalline Fe-Pd films sputtered onto SiO_2 substrates. The aim was to overcome some of the drawbacks of epitaxial layers, such as costly substrates, the necessity for heating during deposition, and a more complicated fabrication with limited film thickness. Obtaining SME in polycrystalline films is important for industrial purposes. However, no systematic research has yet been carried out on these films. The present research was designed as a comparative study. The samples were heated ex situ in an oven, and were subsequently quenched to maintain their microstructures. For comparison, the same temperatures were selected for in situ heating experiments. Our main interest was the intermediate stages during the phase transformation from bcc to fcc structures. We also conducted in situ Lorentz microscopy analyses.

The last part of this section focuses on the characterization of ternary Fe-Pd-Pt alloys. For this purpose, TEM investigations were performed on Fe-Pd-Pt thin films sputtered onto SiO_2 substrates using a combination of methods[39]. The addition of a third element such as Pt enhances the functional abilities of Fe-Pd films, but single crystalline and complete ternary films are necessary. For this reason, TEM was needed for the nanoscale characterization of

the structure and composition. In situ cooling TEM experiments were also carried out, and were compared with in situ XRD results in order to identify a functional fct phase.

3.1 Epitaxial Thin Films

a) Au Buffer Layer

The first TEM examinations were carried out on a $Fe_{70}Pd_{30}$ sample produced by our project partners, by sputtering with 100 W power in a magnetron sputtering system (vonArdenne CS730S, 4" target by Kaistar R&D LLC, 99.95 % pure) on a buffered MgO (100) epi-polished substrate. The sputtering rates were selected as 0.073 nm/sec for the $Fe_{70}Pd_{30}$ film, and 0.366 nm/sec for the Au buffer layer. A cross-sectional bright field TEM image of the MgO/Au/$Fe_{70}Pd_{30}$ heterostructure is shown in Figure 10a.

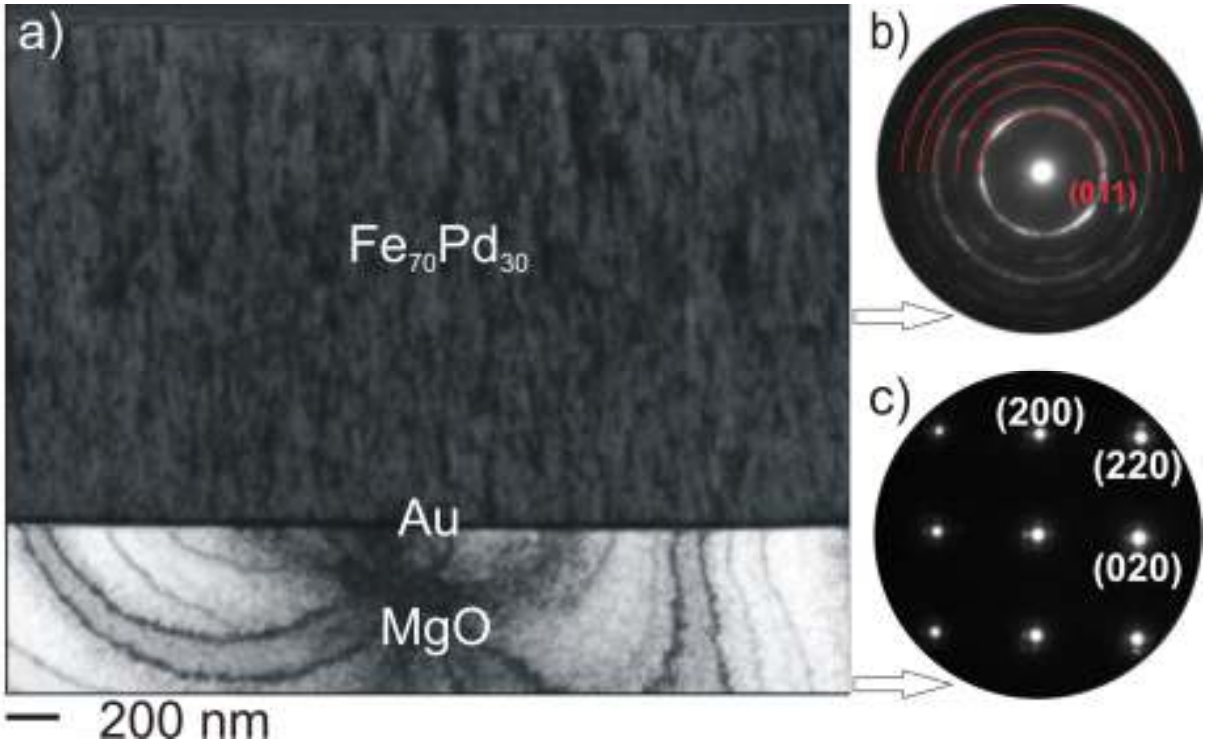

Figure 10: a) TEM bright field image of the heterostructure, ED patterns from b) $Fe_{70}Pd_{30}$, and c) MgO (zone axis: [001]).

Au was selected as a buffer layer for the initial analyses because its in-plane lattice parameter is close to that of one of the fct phases of $Fe_{70}Pd_{30}$. (Literature: a_{Au} = 0.407 nm; a_{fct} = 0.382 nm) The thickness of the sputtered film was determined to be 1.2 µm (Figure 10a).

The main interest was the epitaxial growth of the $Fe_{70}Pd_{30}$ film on various buffer layers. The SAED patterns and the HRTEM images revealed that the $Fe_{70}Pd_{30}$ film was not completely

epitaxial. The presence of almost complete concentric rings in the SAED patterns indicated the polycrystalline nature of the sputtered film. Hence, the film contained a large number of discrete grains with a similar structure, but in random orientations. However, a closer look at the SAED pattern revealed a slightly preferred growth direction of the $Fe_{70}Pd_{30}$ grains along zone axis <011>. This finding agreed well with the results from the XRD analysis.

Table 1 presents the measured values and the reference d-spacings. The calculated values confirm that the polycrystalline $Fe_{70}Pd_{30}$ film has a bcc structure. The d-values calculated from the diffuse intensity located on the concentric circles are marked with semi-circles in Figure 10b. The small grains of $Fe_{70}Pd_{30}$ are clearly the bcc type. The small deviation from the literature data is negligible, since it is in the range of measurement error.

Table 1: The d-values (nm) for the four strongest intensities of $Fe_{70}Pd_{30}$

BCC d/(hkl) ⇓	BCT d/(hkl)	FCC d/(hkl)	FCT d/(hkl)	Measured d
0.150/(0 0 2)	0.203/(1 1 0)	0.187/(0 0 2)	0.191/(2 0 0)	0.149
0.123/(1 1 2)	0.161/(0 0 2)	0.133/(0 2 2)	0.182/(0 0 2)	0.121
0.106/(0 2 2)	0.144/(2 0 0)	0.113/(1 1 3)	0.135/(2 2 0)	0.105
0.095/(0 1 3)	0.126/(1 1 2)	0.108/(2 2 2)	0.132/(2 0 2)	0.094

The SAED pattern recorded on the MgO substrate in the zone axis [001] showed additional reflections around the fundamental reflections (Figure 10c). These reflections originate from the so-called Moiré effect, and were also noticeable in the HRTEM micrographs. These effects occur when two identical periodic structures are superposed randomly on top of each other with a small scaling or angle difference. Figure 11 depicts the HRTEM micrograph of the Au-MgO interface with corresponding FFT patterns. Heteroepitaxy between both layers can be identified from the FFT patterns. The growth relationships between the layers are:

(100) MgO, (11-1) Au ‖ [001] MgO, [101] Au.

(**Nomenclature**: The epitaxial relationship is specified by first giving the plane in the film that is parallel to the substrate, followed by the growth direction of both layers).

After averaging three measurements from each of eight regions, the EDX spectra indicated a non-significant deviation from the stoichiometry $Fe_{70}Pd_{30}$, namely $Fe_{71(1)}Pd_{29\,(1)}$.

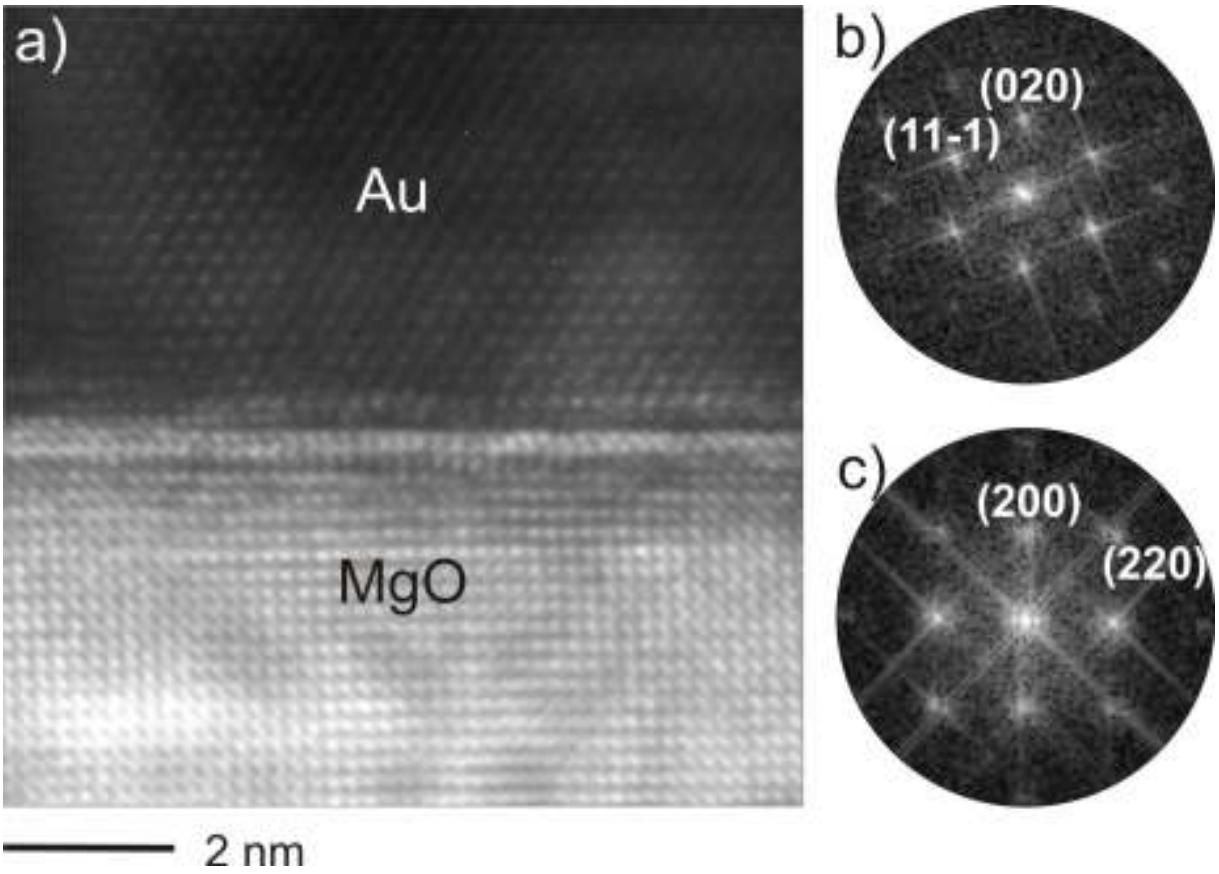

Figure 11: a) HRTEM image from MgO-Au interface, FFT patterns from b) Au film and c) MgO substrate.

Thus, the heteroepitaxial growth of an Au buffer layer on the MgO substrate was successful, but the epitaxy was not transferred to the $Fe_{70}Pd_{30}$ film. Although a very slight texture is visible in both X-ray and electron diffraction data, the desired single crystallinity requires the introduction of an adhesion promoter.

In addition to the structural and chemical characterization of the thin film, its magnetic properties were also investigated via Lorentz microscopy. Note that the mobility of magnetic domains with the excitation of an external magnetic field is important for the function. For example, pinning sites can hinder the mobility of the domain walls, which may affect the SME. These pinning sites cause the magnetization reversal in the material to lag behind the applied magnetic field. This delay, which results in Barkhausen jumps in the magnetic structure, can be observed in the magnetization curves.

The domain structure in a soft magnetic material is dictated by the total magnetic energy of the system, where the material, in most cases, forms magnetic domains to minimize this energy. Several energy types contribute to the total magnetic energy: exchange energy[40], magnetic anisotropy energy[41], magnetostatic energy[42], magnetoelastic energy[43], and Zeeman energy[44].

$$e_{total} = e_{exchange} + e_{anisotropy} + e_{magnetostatic} + e_{magnetoelastic} + e_{Zeeman}$$

Exchange energy deals with the alignment of the neighboring spins: when their alignment is parallel, they have the lowest energy state, whereas the antiparallel alignment results in the highest energy state. Magnetic anisotropy in a material creates certain axes, where the material is easier or more difficult to saturate magnetically. This term in the total magnetic energy of a system also depends on some anisotropic terms: magnetocrystalline anisotropy, induced anisotropy, shape anisotropy, and exchange anisotropy. When the magnetocrystalline anisotropy is absent inside the material (as in the case of amorphous thin films), the magnetization vector lies in the plane of the film due to the large shape anisotropy. Hence, the magnetization vector exhibits a preferred orientation only in the presence of some type of anisotropic component. Aligning all the spins along a preferred magnetization axis (easy axis) minimizes the exchange energy and magnetic anisotropy terms but the magnetostatic energy, which is correlated to the stray fields, becomes so high that the material divides itself into magnetic domains in order to reduce the magnetostatic energy. This multi-domain configuration leads to the formation of domains of perpendicular and anti-parallel alignment. These domains are separated by domain walls, where the type of the wall is directly correlated to the sample thickness.

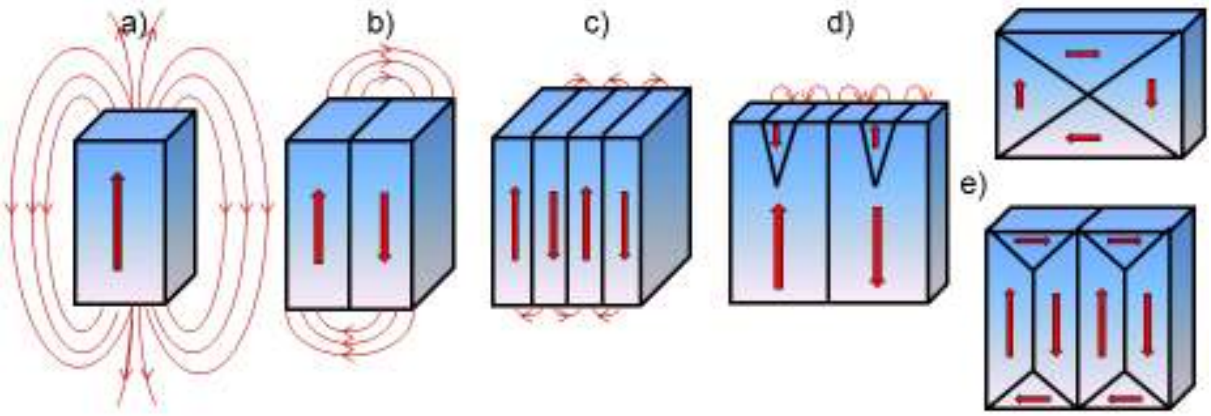

Figure 12: a)-e) Possible domain configurations occurring in magnetic thin films and respective stray fields.

Figure 12a illustrates a magnetized sample that exhibits uniaxial anisotropy. The ends of the films show large stray fields. Large numbers of free magnetic poles exist in the single domain configuration. Splitting the domains into two with the opposite magnetization reduces the stray fields, as well as the magnetostatic energy (Figure 12b). Further division of the domains is shown in Figure 12c. If the energy needed to create a new domain wall exceeds the accompanying reduction in the magnetostatic energy, then the sub-division of the domains continues up until that point.

Reverse spike domains are also introduced at the edges of the films when the material has uniaxial anisotropy. The magnetization on either side of the wall is anti-parallel, and these spike domains can appear in virtually all magnetic materials. If the magnetization direction

changes by 90°, then the corresponding domains are separated by 90° walls. Possible configurations are depicted in Figure 12e. These types of domain structures usually occur in cubic crystals where easy axes exist at 90° to each other. The triangular domains are called closure domains. The second type of domain structure containing both 180° and 90° walls, often forms (bottom) since it reduces the magnetoelastic energy, which is dependent upon the area of the domains. No free poles are present in either example, so the magnetostatic energy is reduced to zero. If the material contains strain or exhibits high magnetocrystalline anisotropy, then the magnetization pointing along a hard axis is involved, which is energetically unfavorable to form closure domains.

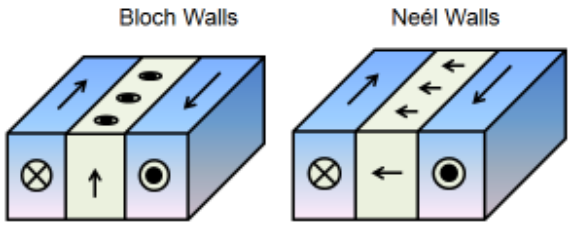

Figure 13: Two types of magnetic domain walls. Néel walls with in-plane, and Bloch type wall with out of plane magnetizations.

A balance between these energies determines the thickness of the domain wall. Figure 13 shows the two main types of domain walls existing in thin films. The first is the Bloch wall, which appears in bulk materials; the magnetization rotates out of the plane of the film[45]. The second one is the Néel wall, where the magnetization rotates from the direction of the first domain to the direction of the second, with a rotation that is within the plane of the domain wall[45]. The Bloch wall is more common, but a Néel wall is often favored in thinner films. A third type of wall is also recognized: the so-called cross-tie wall, which is a mixture of spins pointing out and in the plane (not shown). It is identified by spike walls that form to ensure flux closure.

The application of an external magnetic field causes the magnetization to begin to reverse in the direction of the applied field. This process is carried out by magnetization rotation and/or domain wall motion. The magnetization reversal in the easy axis is mainly dominated by the domain wall motion, whereas the magnetization rotation dominates the magnetization reversal in the hard axis. Lorentz microscopy investigations were conducted in the present study, in order to interrelate the crystal structure to the magnetic structure.

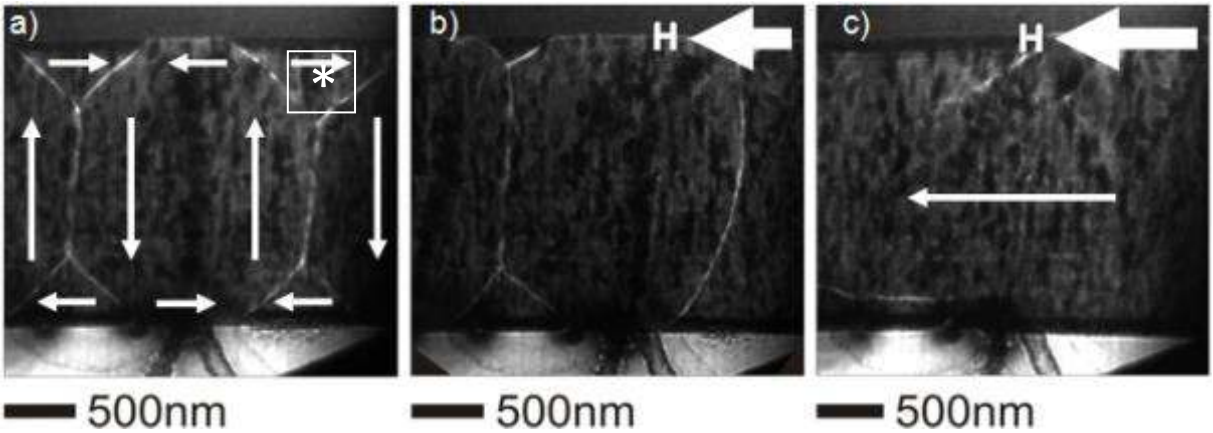

Figure 14: Lorentz microscopy images. Objective lens, a) switched off, b) excited 5.1% (0.146 T), c) excited 15.6% (0.424 T).

Lorentz images were recorded at variable excitations of the internal magnetic field. As a first step, the objective lens was switched off and the Lorentz lens turned on for magnetic field-free investigations. The incident electron beam was deflected by Lorentz force, due to the magnetization in each domain, causing a variation of electron distribution at positions corresponding to the walls. The specimen exhibited 180° magnetic domain walls, which separated neighboring domains with antiparallel magnetization. Increases in the magnetic field caused the domains with antiparallel alignment in the middle to start to rotate their magnetization direction. Likewise, the closure domains possessing antiparallel magnetization directions with respect to the applied field direction started to shrink (Figure14b). Magnetic domains aligned themselves in the direction of the applied magnetic field in order to minimize their entropy. The domain walls locally vanished when the objective excitation was at 15.6%, which corresponded to a saturation field value of around 0.424T. At that point, the specimen was in a single domain state (The magnetic field values of the objective lens were obtained from Prof. Zweck at the University of Regensburg, private communication).

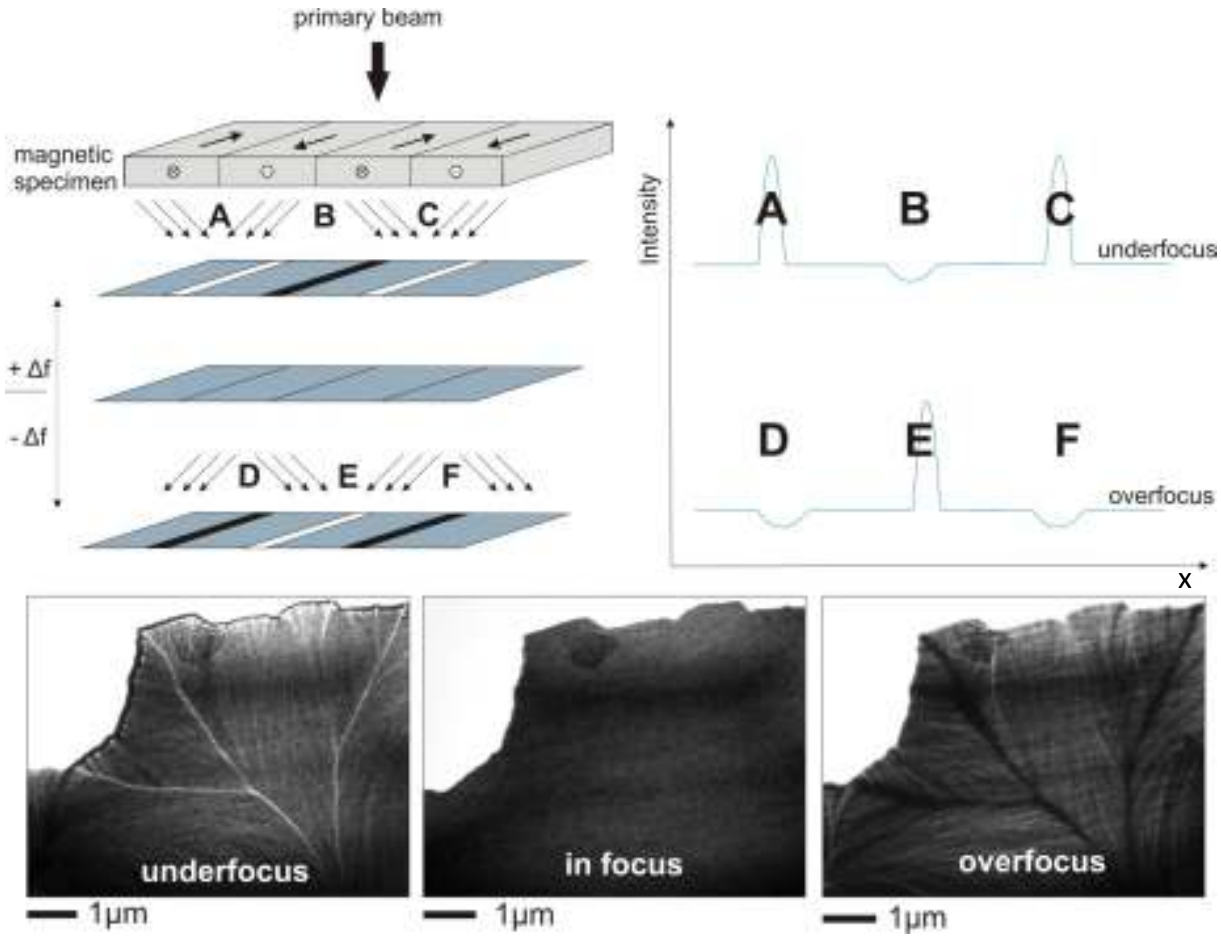

Figure 15: Schematic description of Fresnel imaging in Lorentz microscopy, showing the presence of Bloch type magnetic domain walls in the $Fe_{70}Pd_{30}$ film. Intensity distribution of magnetic domain walls shows an opposite contrast in over- and underfocus conditions. Representative images are depicted in the lower panels.

During in situ magnetic stimulation of the thin film, the domain walls moved along the film plane (not moving out of the plane), showing their Bloch type character. Néel walls would not be visible in Fresnel mode during the application of the external magnetic field. A possible domain configuration is schematized in Figure 14a. The contrast of the domain walls changes, depending on the focus conditions. A sharper contrast is always seen for domain walls that appear bright than for dark appearing domain walls. The intensity distribution and the schematic description of the Fresnel imaging are given in Figure 15. A careful look at the Lorentz images reveals changes in the size of the magnetic domains. As the magnetic domain on the right side (marked with a star) gets larger, the magnetic domain on the right top domain becomes smaller. Hence, the external magnetic field applied with the objective lens has a component coming from the right side (with respect to the given Lorentz images), and the domain on the right has some magnetization direction. Based on this information, other possible magnetization directions of all domains can be identified. The arrows in Figure 14a illustrate this configuration.

b) Au Buffer Layer with Cr (50 nm) as an adhesion promoter

Complete epitaxial growth of a $Fe_{70}Pd_{30}$film was achieved by sputtering a 50 nm thick Cr adhesion promoter between the MgO and Au layers. Cr is recognized for its ability to stabilize the temperature in the sputtering chamber, reducing diffusion, migration, and segregation of contact materials in the layers[46].

As a first trial, the sputtering rates were selected as 0.238 nm/sec, 0.6 nm/sec, and 0.084 nm/sec for Cr, Au, and $Fe_{70}Pd_{30}$, respectively.

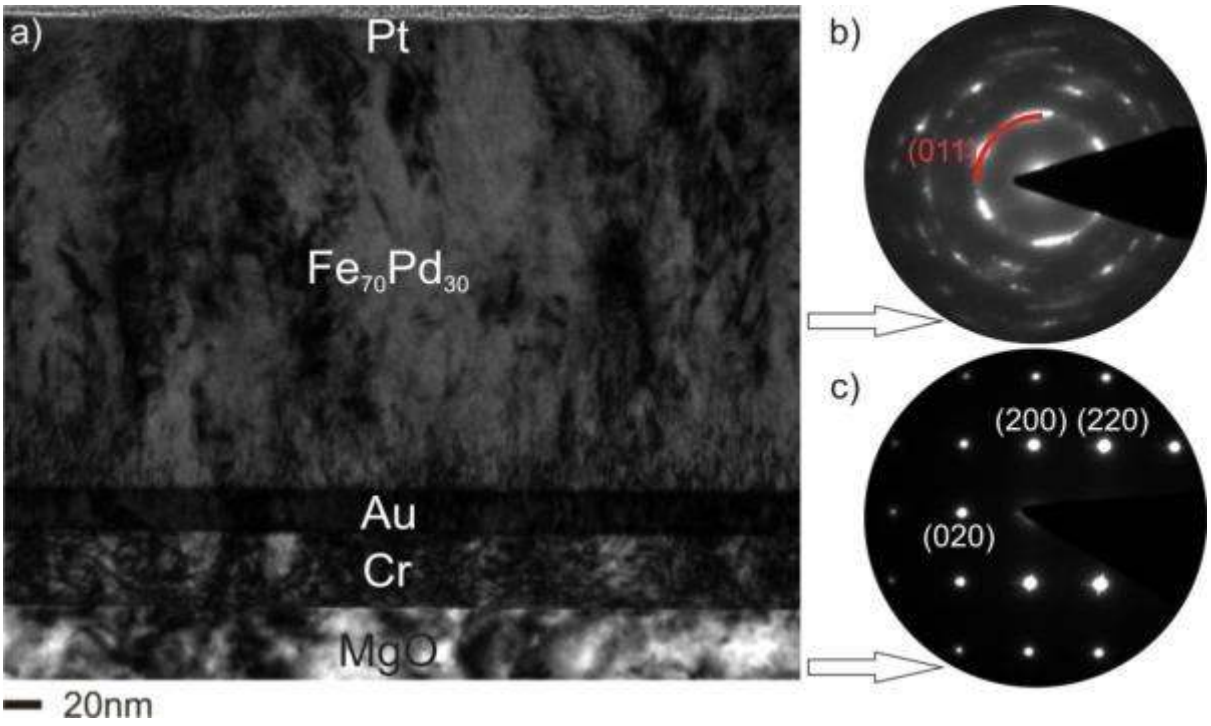

Figure 16: a) Cross-sectional bright field TEM image from the MgO/Cr/Au/$Fe_{70}Pd_{30}$/Pt heterostructure, SAED patterns from b) $Fe_{70}Pd_{30}$ film and c) MgO substrate.

The bright field TEM image clearly shows a 40 nm thick Cr adhesion promoter layer. The FFT patterns calculated from HRTEM micrographs and SAED patterns show that the complete structure of the $Fe_{70}Pd_{30}$ film is polycrystalline and of the bcc type. However, Figure16b shows that the $Fe_{70}Pd_{30}$ sample is strongly <011> textured, as indicated by the broad maxima located on the circle of diffuse intensity, with d = 0.211 nm (according to (011)). Consequently, the FFT in Figure 17b (top) exhibits defined spots consistent with this type of preferred orientation.

Table 2: The d-values (nm) for five high-intensity reflections in $Fe_{70}Pd_{30}$

BCC d/(hkl) ⇩	BCT d/(hkl)	FCC d/(hkl)	FCT d/(hkl)	Calculated d/(hkl)
0.212/(0 1 1)	0.214/(1 0 1)	0.217/(1 1 1)	0.217/(1 1 1)	0.212
0.150/(0 0 2)	0.203/(1 1 0)	0.187/(0 0 2)	0.191/(2 0 0)	0.149
0.123/(1 1 2)	0.161/(0 0 2)	0.133/(0 2 2)	0.182/(0 0 2)	0.124
0.106/(0 2 2)	0.144/(2 0 0)	0.113/(1 1 3)	0.135/(2 2 0)	0.106
0.095/(0 1 3)	0.126/(1 1 2)	0.108/(2 2 2)	0.132/(2 0 2)	0.094

Table 2 depicts the measured d-values of the five highest intensities. The values again match those of the bcc phase. No splitting of <110> reflections into the (101) and (110) reflections is reflected, which would indicate a tetragonal distortion of the $Fe_{70}Pd_{30}$ unit cell.

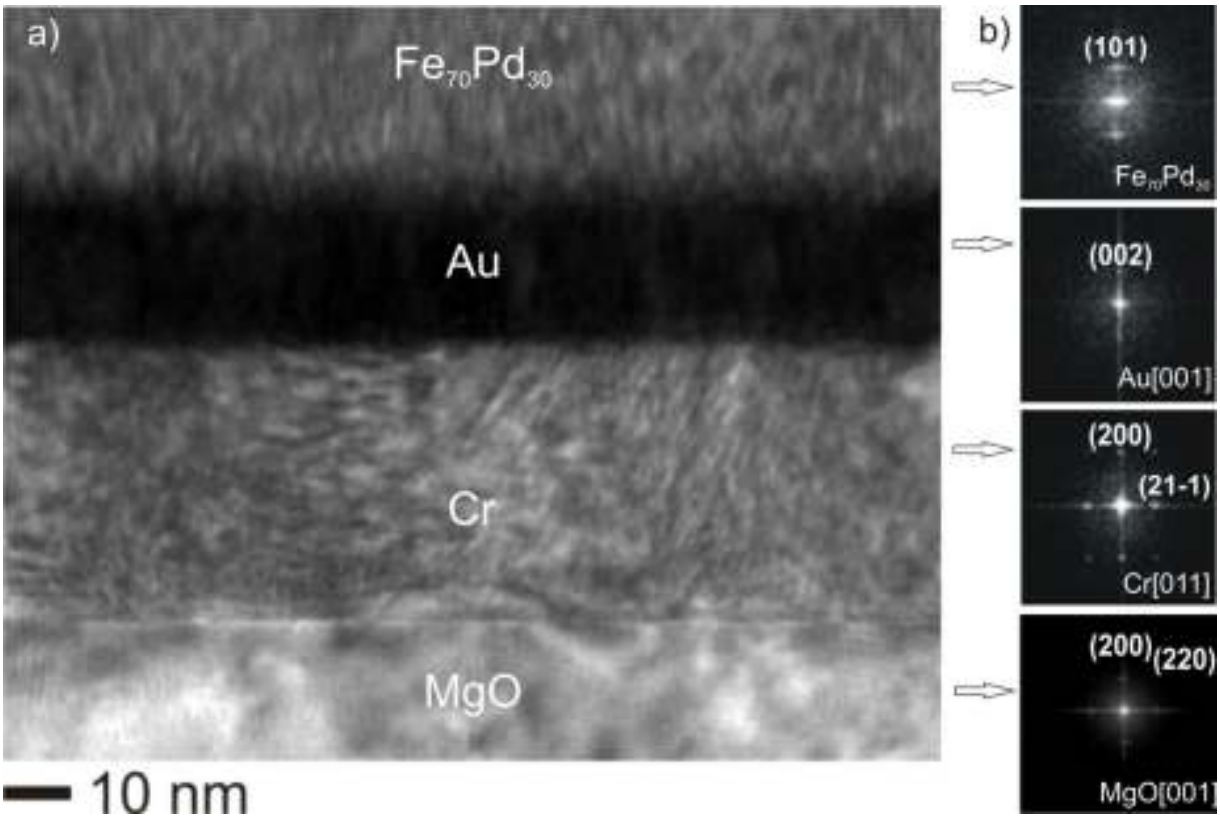

Figure 17: a) HRTEM micrograph of the heterostructure, b) FFT patterns from $Fe_{70}Pd_{30}$, Au, Cr, and MgO layers.

From the FFT patterns, the growth relationships between the layers are determined to be:

(100) MgO ‖ (100) Cr, [001] MgO ‖ [011] Cr,
(100) Cr ‖ (001) Au, [011]Cr ‖ [001] Au

A clear difference in the growth process was observed for the Au buffer layer. The Cr adhesion promoter causes Au to grow on MgO in the [001] direction, instead of the [101]. The HRTEM micrographs also verified the complete epitaxy of the Cr adhesion layer for its entire thickness (Figure 17). Hence, in the next step, the thickness of this Cr layer can be reduced in order to save on material. The nanoprobe chemical analyses performed in the STEM mode again verified no change in the composition when moving from the buffer interface to the film surface. The composition was determined to be $Fe_{70(1)}Pd_{30(1)}$ (an average value calculated from five measurements). No oxidation or interdiffusion at the interfaces was indicated.

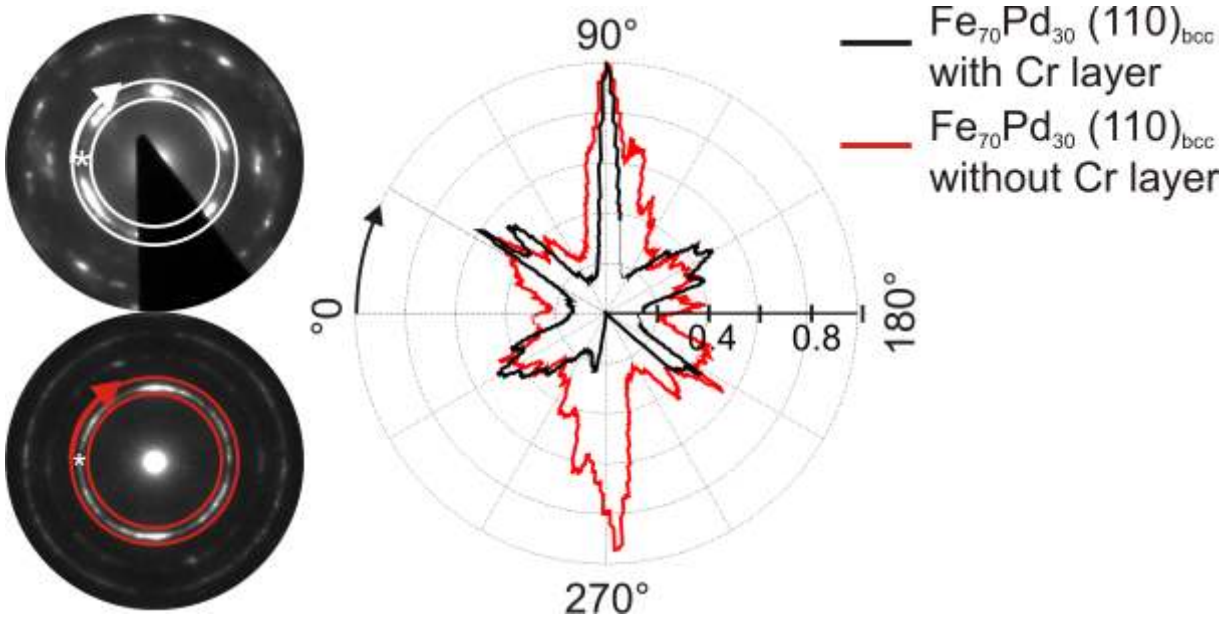

Figure 18: Intensity distribution of <110> planes for the $Fe_{70}Pd_{30}$ films. The film grown with Cr adhesion promoter shows strong texture (black label) of the <110> planes, in comparison to the film grown without adhesion promoter (red label).

The adhesion promoter affected the growth behavior of the entire heterostructure. When compared with the layered system without an adhesion promoter, a preferred orientation of the $Fe_{70}Pd_{30}$ grains was noted, which was visible in the circular intensity integration of the (110) planes of both films. The film grown with the Cr adhesion promoter showed strong texture (black label) of the (110) planes, in comparison to the film grown without adhesion promoter (red label) (Figure 18). However, the desired fct phase was not achieved. The next approach was to lower the sputtering rate for the layers, so as to give the atoms more time for arrangement on the interfaces. This was expected to reduce the misfit and to support the complete epitaxial growth of films of greater thicknesses.

c) Au Buffer with Optimized Cr (5 nm) as an Adhesion Promoter

A similar procedure was repeated for the heterostructure sputtered at lower sputtering rates. Figure 19a depicts a cross-section bright field TEM image of the $Fe_{70}Pd_{30}$ film. The stripes on this image originated from the bending effects, and were possibly caused by the FIB preparation. No indication of columnar growth or small-angle grain boundaries was observed. The film showed an almost perfect single-crystalline structure. SAED patterns of the $Fe_{70}Pd_{30}$ film and MgO are shown in Figures 13b and c, respectively. These SAED patterns show that the in-plane lattice parameter of the buffer layer and the $Fe_{70}Pd_{30}$ film were maintained constant (d-value = 0.210 nm).

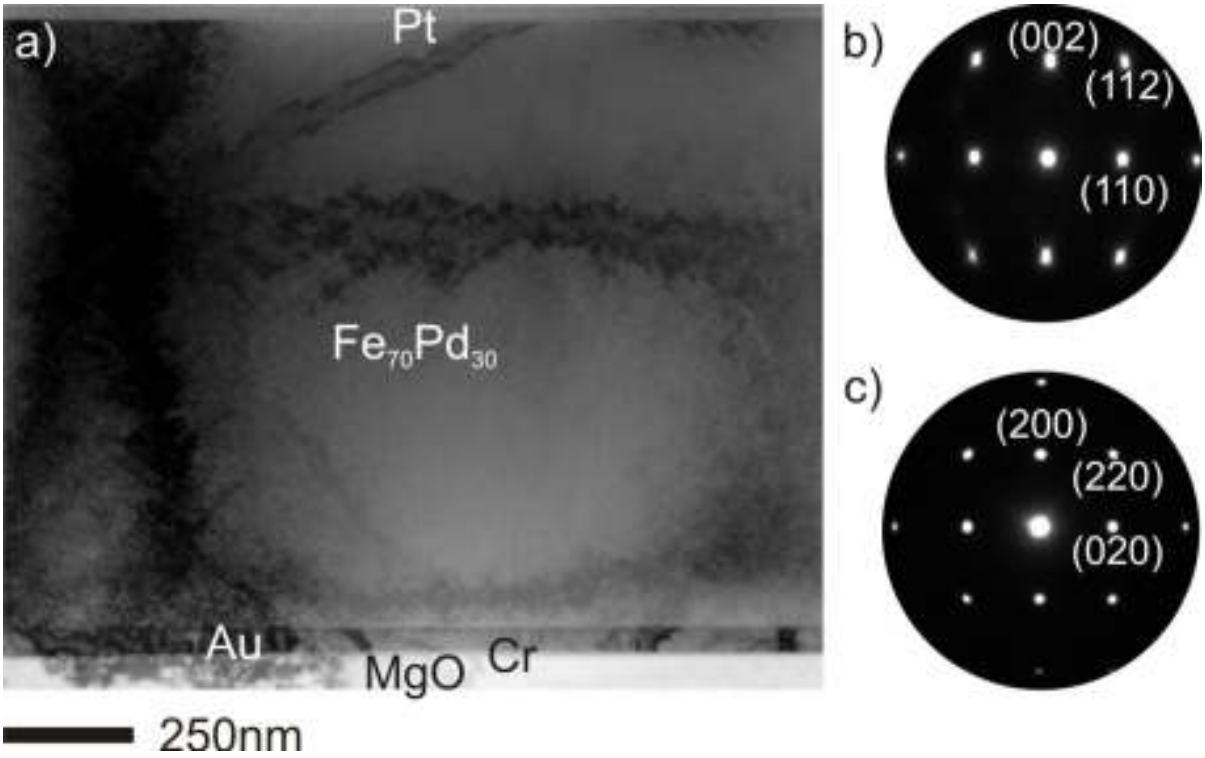

Figure 19: $Fe_{70}Pd_{30}$ thick film, a) BF TEM image, SAED patterns from b) $Fe_{70}Pd_{30}$ [1-10] film and c) MgO [001] substrate.

The possible tetragonality of the structure was determined by tilting the film 45° with respect to the given zone axis, as shown in Figure 19b. Note that the direct observation of the lattice distortion is advantageous for the determination of the tetragonality. In the given [110] zone axis of the $Fe_{70}Pd_{30}$, only the a-axis can be measured directly. Tilting the sample 45° makes the observation of both the a- and c-axis in one diffraction pattern possible. However, some experimental difficulties have to be overcome, or to be tolerated. Firstly, tilting of the specimen increases the travelling distance of the electrons inside the specimen; thus, the spatial resolution decreases and the intensity distribution becomes unreliable in the SAED pattern. This would not influence the d-spacings, but the structure resolution becomes challenging due to the unreliable intensity of the individual reflections. Secondly, tilting in the

microscope is experimentally limited to 45° when using a double tilt holder, so the necessary tilting angle is limited by the microscope. Fortunately, the sample was bent during the FIB preparation, providing the necessary angles for the tilted observations. Figure 20a depicts the diffraction pattern recorded along the [010] zone axis, showing the bct structure of the $Fe_{70}Pd_{30}$ film.

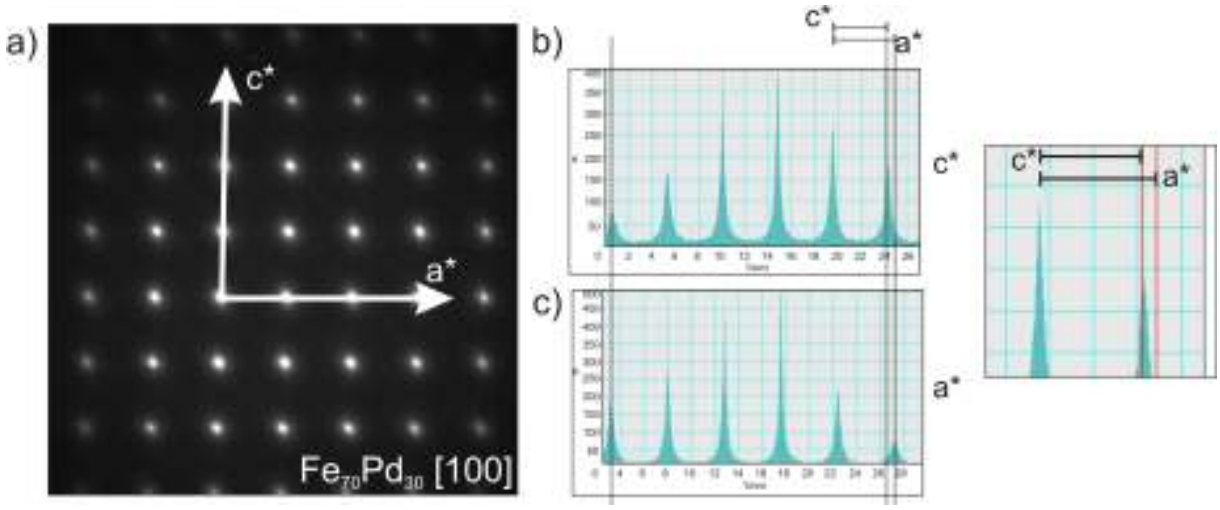

Figure 20: a) SAED pattern recorded along the [100] zone axis of $Fe_{70}Pd_{30}$. b) and c) are the line profiles measured in c* and a* directions, respectively. The enlargement clearly shows the difference in the a and c axes on the right side.

The tetragonal distortion of the unit cell is clearly visible in the given line profiles (Figure 20b and c). The distortion of the bct unit cell is calculated from the line profiles as $(c/a)_{bct} = 1.07$.

Figure 21a is an HRTEM micrograph that shows a very rough interface between Au and $Fe_{70}Pd_{30}$. Figure 21b gives the FFT patterns of the two individual layers. The well-defined orientation relationship between Au and $Fe_{70}Pd_{30}$ can be explained by similarities in metrics of Au and $Fe_{70}Pd_{30}$ (Figure 21). Thus, we conclude that an epitaxial layer of $Fe_{70}Pd_{30}$ on chromium directed Au is attainable under low sputtering rate conditions.

The orientation relationships between the layers were determined from SAED, as well as from HRTEM investigations:

MgO-Cr :	(100) Cr ‖ (100) MgO and [011] Cr ‖ [001] MgO
Cr-Au:	(100) Au ‖ (100) Cr, [001] Au ‖ [011] Cr,
Au-$Fe_{70}Pd_{30}$:	(001) $Fe_{70}Pd_{30}$ ‖ (100) Au, [1-10] $Fe_{70}Pd_{30}$ ‖ [001] Au

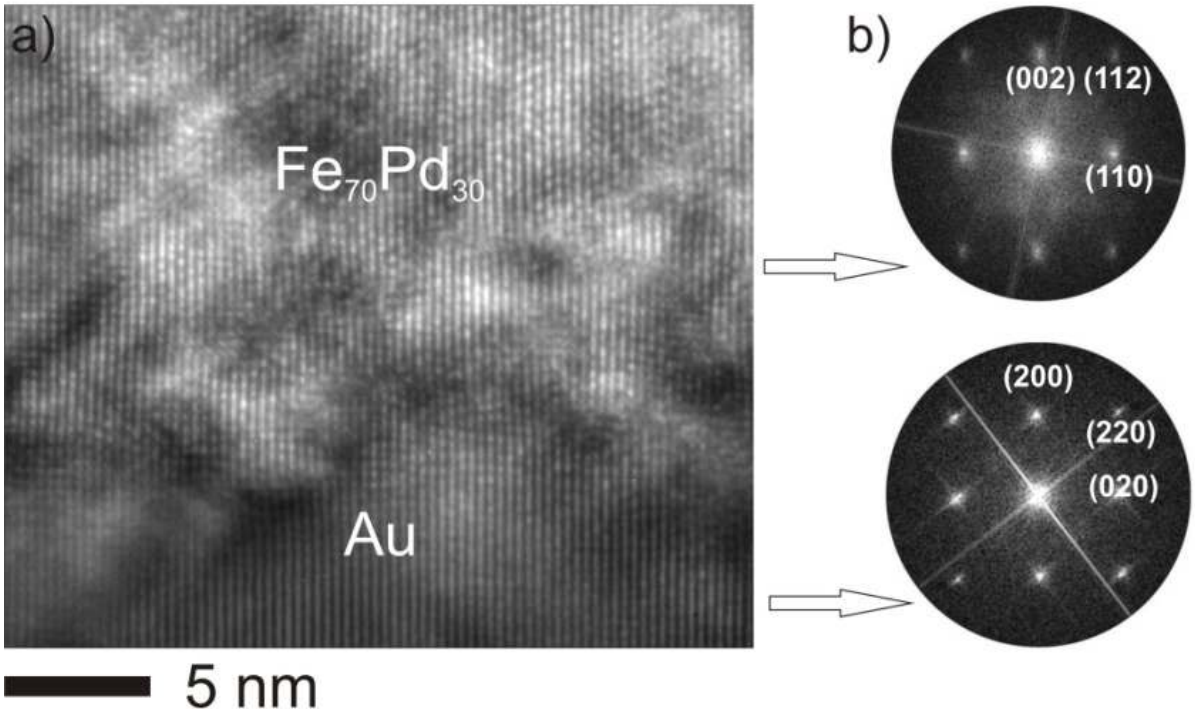

Figure 21: a) HRTEM image from Au-$Fe_{70}Pd_{30}$ interface, b) FFT patterns from $Fe_{70}Pd_{30}$ [1-10] film (top) and the Au [001] buffer (bottom).

Figure 22 depicts an HRTEM micrograph of the $Fe_{70}Pd_{30}$ film in [100] orientation. Characteristic diffuse scattering is observed for the film. This feature can be explained by the tweed model found for $Fe_{70}Pd_{30}$. The tweed structure is induced by the static displacement of atoms associated with the formation of disc-shaped martensite nuclei on the {110} planes of the austenite[47]. In the case of the investigated film, the diffuse stripes ran along the [100] direction in bcc cell settings, which corresponds to the [110] direction of the austenitic lattice (Figure 22b, marked with an arrow). Hence, these results are in good agreement with the model. Note that the tweed structure is only observed in $Fe_{70}Pd_{30}$ during the transformation from fcc austenite to fct martensite. One possible reason could be that the tweed microstructure persisted in the bct martensite after the sputtering, because the degree of tetragonality is small and the c-axis directions of the small bct martensite variants are tilted against each other, giving rise to the tweed pattern.

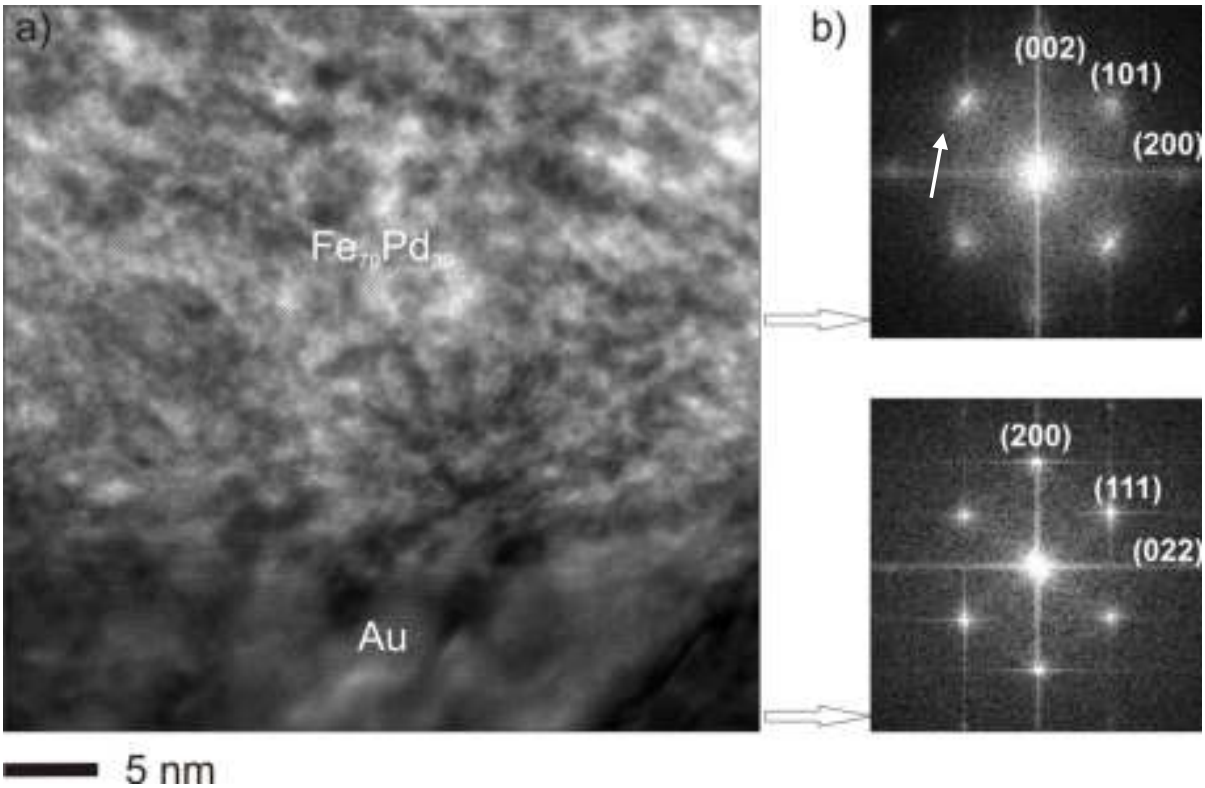

Figure 22: a) HRTEM image of Au- $Fe_{70}Pd_{30}$ interface, b) FFT patterns from $Fe_{70}Pd_{30}$ [010] and Au [010] layers when the specimen is tilted 45°.

These structural characterizations were augmented by chemical analyses performed via nanoprobe EDX and energy filtered imaging techniques. Nanoprobe EDX investigations in the STEM mode verified that the composition of the thick film was $Fe_{70(0.5)}Pd_{30(0.5)}$ (5 measurements).

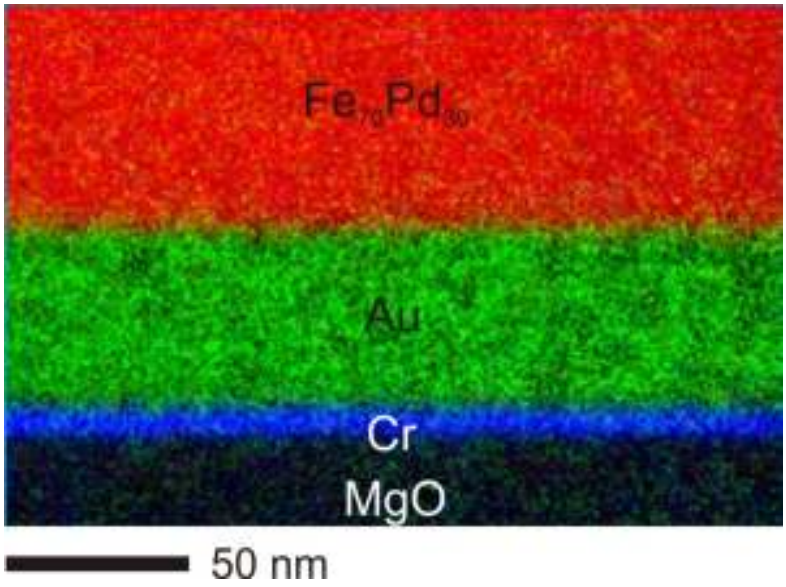

Figure 23: EFTEM elemental map from an MgO/Cr/Au/FePd heterostructure.

Figure 23 illustrates the superimposed EFTEM elemental map for MgO/Cr/Au/$Fe_{70}Pd_{30}$. The maps for each element are measured separately and are later overlaid on each other. No significant interdiffusion occurred at either interface of the Cr layer. These data also demonstrate the usefulness of EFTEM analysis, since the Cr layer is clearly indicated, in contrast to the BFTEM image.

Lorentz microscopy analyses were also performed, and did not reveal the presence of any magnetic domain walls. The film consisted of a single magnetic domain. Since the film was a single crystalline type, the magnetocrystalline anisotropy component of the complete magnetic anisotropy dominated in the film. The magnetization vector lay in-plane with respect to the given projection.

d) $Mn_{80}Ir_{20}$ Buffer Layer with an Adhesion Promoter

As previously mentioned, the SME is only observed in the fct structure of $Fe_{70}Pd_{30}$. The previous results showed that the structure of the $Fe_{70}Pd_{30}$ layer could be tuned using the buffer layer and sputtering rate; therefore, we endeavored to induce the desired fct structure in $Fe_{70}Pd_{30}$ by choosing a proper metallic buffer layer with an in-plane lattice parameter that would more evenly match those of the fct $Fe_{70}Pd_{30}$. This time, $Mn_{80}Ir_{20}$ was selected as the buffer layer. The in-plane lattice parameters of $Mn_{80}Ir_{20}$ and the desired fct $Fe_{70}Pd_{30}$ structures were $a_{Mn80Ir20}$ = 0.378 nm and a_{fct} = 0.382 nm, respectively. Since they were very close in value, an fct growth was expected for the $Fe_{70}Pd_{30}$ thin film.

Figure 24 shows a bright field TEM image of the MgO/Cr/$Mn_{80}Ir_{20}$/$Fe_{70}Pd_{30}$/Pt heterostructure. The thickness of the sputtered $Fe_{70}Pd_{30}$ was measured as 96 nm. The thickness of the layer was kept thin with respect to the previous films, in order to conserve material. The main focus was the procurement of a stable fct structure in the $Fe_{70}Pd_{30}$ film.

Figure 24b depicts the SAED pattern recorded for the $Fe_{70}Pd_{30}$ film. The diffuse intensity in a concentric circle, evident in the SAED, is caused by the amorphous Pt layer originating from the FIB preparation. Note that the SAED aperture represents an area of a circle with a diameter in the region of 250 nm. Since the film exhibits a thickness of ~100 nm, the collection of additional information/diffraction data from other layers is inevitable when using the SAED aperture.

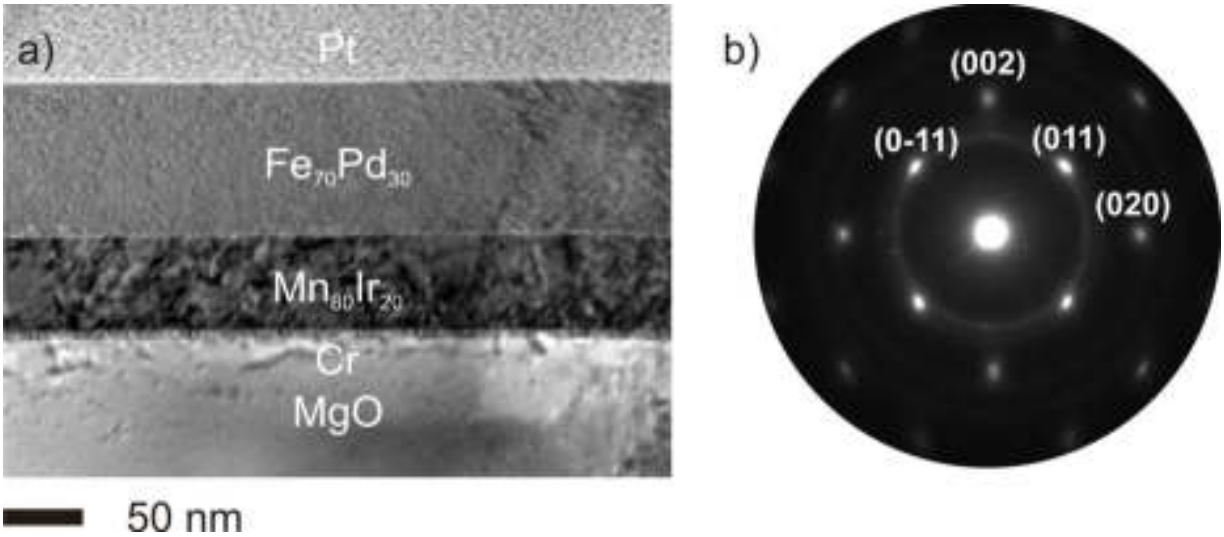

Figure 24: a) BF TEM image of the heterostructure b) SAED pattern from the $Fe_{70}Pd_{30}$, zone axis [010].

This film showed similar growth behavior to that observed for the film grown on the Au buffer layer with optimized sputtering parameters, as identified from the SAED pattern. However, in this case, the [010] zone axis was obtained directly, without too much tilting of the specimen. The reason is the difference in the FIB cut for the TEM sample preparation. This time, the sample was rotated by 45° with respect to the substrate edge during FIB milling, which made it possible to observate of the a and the c lattice parameters directly. The FFT pattern and the HRTEM micrographs of the materials revealed that the complete heterostructure was epitaxial. A small tetragonal distortion was verified. The $(c/a)_{bct}$ ratio was determined to be 1.03 according to the line scans obtained from $[100]_{bct}$ SAED patterns, which exhibited the bct type of structure. This value deviates from the XRD results of $(c/a)_{bct}$ = 1.12, which could be due to several reasons. Of course, the preparation method (FIB) could have an effect, for example by the bending of a FIB lamella, as observed during the FIB milling process. Moreover, the TEM provides data from the local structure, whereas the c/a ratios calculated from the XRD analysis are derived from the bulk. The sample dimension of the XRD samples are in the range of several centimeters in width and length. The distortion and the complete epitaxial growth of the layers are also confirmed by the HRTEM studies. Figure 25a depicts the HRTEM micrographs of the MgO/Cr/$Mn_{80}Ir_{20}$ and the $Mn_{80}Ir_{20}/Fe_{70}Pd_{30}$ interfaces. The orientation relationships were calculated from the FFT patterns (Figure 25b) between the layers as:

(002) $Fe_{70}Pd_{30}$ ‖ (200) $Mn_{80}Ir_{20}$, [100] $Fe_{70}Pd_{30}$ ‖ [011] $Mn_{80}Ir_{20}$
(200) Cr ‖ (200) $Mn_{80}Ir_{20}$, [010] Cr ‖ [011] $Mn_{80}Ir_{20}$
(200) Cr ‖ (200) MgO, [010] Cr ‖ [011] MgO

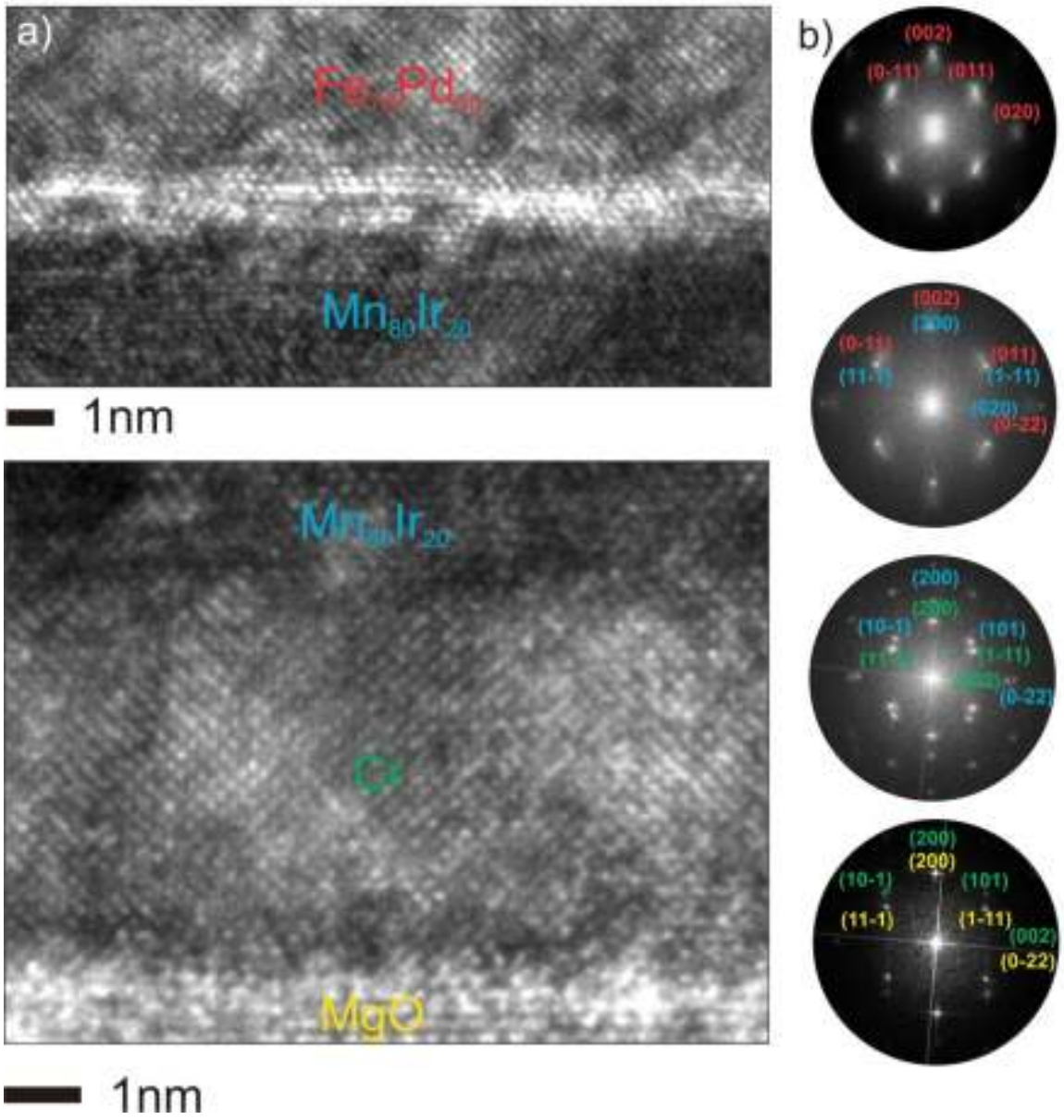

Figure 25: HRTEM micrograph of a) $Mn_{80}Ir_{20}$/ $Fe_{70}Pd_{30}$ (top) and MgO/Cr/ $Mn_{80}Ir_{20}$ interfaces, b) FFT pattern from each layer.

The well-defined orientation relationship between $Mn_{80}Ir_{20}$ and $Fe_{70}Pd_{30}$ can be explained by the similarities in the lattice parameters of $Mn_{80}Ir_{20}$ and $Fe_{70}Pd_{30}$. The misfit between the bct $Fe_{70}Pd_{30}$ and the fcc $Mn_{80}Ir_{20}$ layers is calculated to be 7.1%. Although the misfit is larger that that of the heterostructure with an Au buffer layer, a complete epitaxial growth of the $Fe_{70}Pd_{30}$ film was still achieved.

For both the epitaxial and bct type $Fe_{70}Pd_{30}$, the Lorentz mode was turned on after performing the TEM analyses. The Fresnel images showed no contrast related to magnetic domain walls. This result was expected for single variant martensitic layers. The strong

magnetocrystalline anisotropy of the single variant layers results in the formation of single magnetic domain variants; hence, no magnetic domain walls can be observed.

e) A 3 μm thick $Fe_{70}Pd_{30}$ sputtered film with an Au buffer layer

After obtaining the bct type martensite with greater thickness (1.2 μm), the $Fe_{70}Pd_{30}$ film was sputtered according to the same parameters. This time, a 3 μm film thickness was selected in order to determine the critical thickness of the stable bct phase.

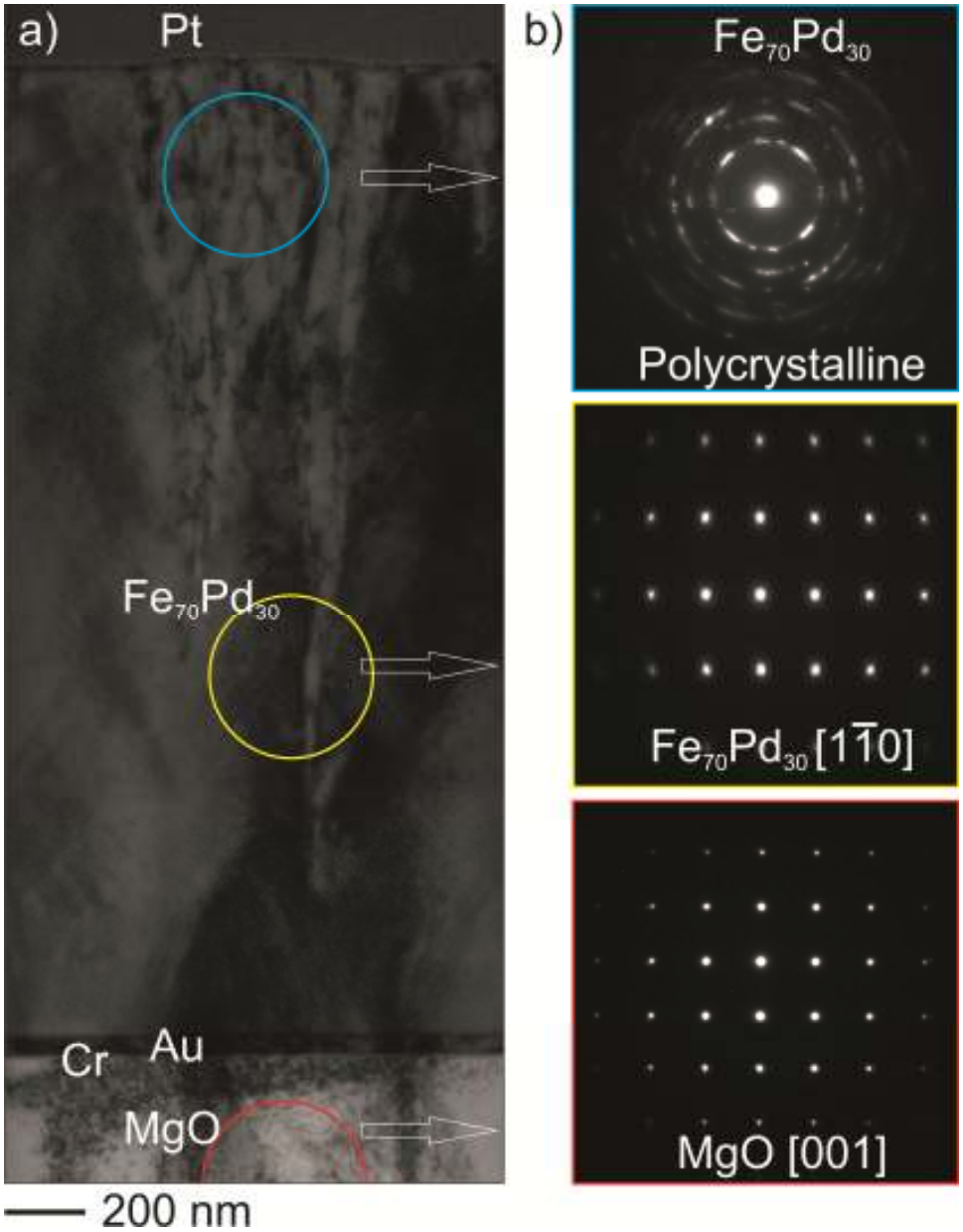

Figure 26: A 3 μm thick $Fe_{70}Pd_{30}$ film; a) Bright field TEM micrograph from cross-section; b) selected area electron diffraction patterns recorded from the marked regions.

Figure 26 shows a bright field TEM micrograph of the 3 µm thick $Fe_{70}Pd_{30}$ thin film. A significant difference in the microstructure can be observed in the micrograph. The SAED patterns recorded on the marked regions also confirm the change in the microstructure. At the substrate interface, the film grows as a single variant bct martensite, in agreement with the earlier results. Moving from the interface region to the film surface, the structure relaxes and becomes polycrystalline, as indicated by the presence of the concentric rings in the diffraction pattern (indicated in blue). The critical thickness is determined to be 1.2 µm for the sputtered film. Table 3 depicts the measured and theoretical d-values for the polycrystalline region.

Table 3: Measured d-values and d-values from the literature for the polycrystalline region with respective (hkl) planes

BCC d/(hkl) ⇩	BCT d/(hkl)	FCC d/(hkl)	FCT d/(hkl)	Calculated d/(hkl)
0.212/(0 1 1)	0.214/(1 0 1)	0.217/(1 1 1)	0.217/(1 1 1)	0.212
0.150/(0 0 2)	0.203/(1 1 0)	0.187/(0 0 2)	0.191/(2 0 0)	0.149
0.123/(1 1 2)	0.161/(0 0 2)	0.133/(0 2 2)	0.182/(0 0 2)	0.124
0.106/(0 2 2)	0.144/(2 0 0)	0.113/(1 1 3)	0.135/(2 2 0)	0.106
0.095/(0 1 3)	0.126/(1 1 2)	0.108/(2 2 2)	0.132/(2 0 2)	0.094

The given d-values indicate that the film is relaxing to a bcc type structure. This conclusion is in contradiction with the DFT (density functional theory) calculations performed by Professor Entel's group in Duisburg (Figure 27). In terms of energy the fcc structure is the most favorable state for these kinds of films[48]; however, a local minimum is additionally present for a c/a_{bcc} ratio around 1, which is dominant in our observations. The film relaxes to its local minimum state after several micrometers, when a buffer layer with an in-plane lattice parameter close to the fct structure is used.

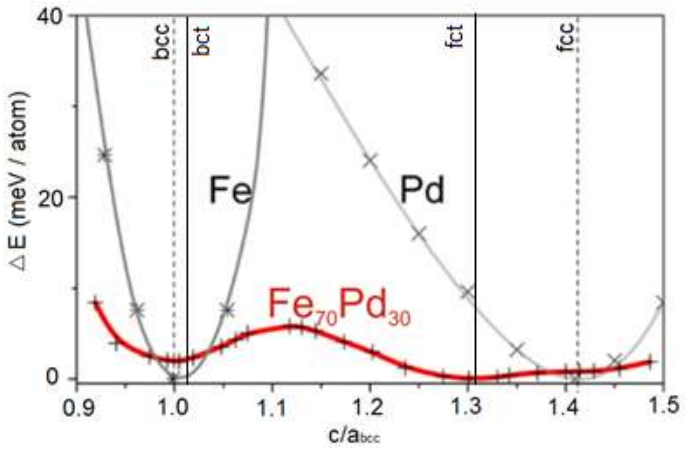

Figure 27: Calculated energy landscapes for Fe and Pd (labeled in grey) with energy minimums located at their equilibrium states. For the $Fe_{70}Pd_{30}$ thin film a fluctuating energy landscape (red curve) is observable with a minimum area around the fcc/fct side. (The image was originally published in ref. 37)

The stress introduced at the interface during sputtering is partly overcome by the misfits at the interface. However, with increasing film thickness, this stress requires further compensation. Two mechanisms for stress relaxation in $Fe_{70}Pd_{30}$ films are mentioned in the literature. Kaufmann-Weiß et al. suggest that $(111)_{fcc}$ twinning is the most common mechanism for this relaxation[49]. However, our HRTEM investigations of the transition region to the polycrystalline area indicate no signs of twinning. Instead, the grain sizes become smaller, and many planar defects are introduced between the grains. Some of the small grains also overlap each other, resulting in Moiré contrast. This finding is in good agreement with the second mechanism, which suggests that the presence of misfit dislocations is responsible for the relaxation process[50].

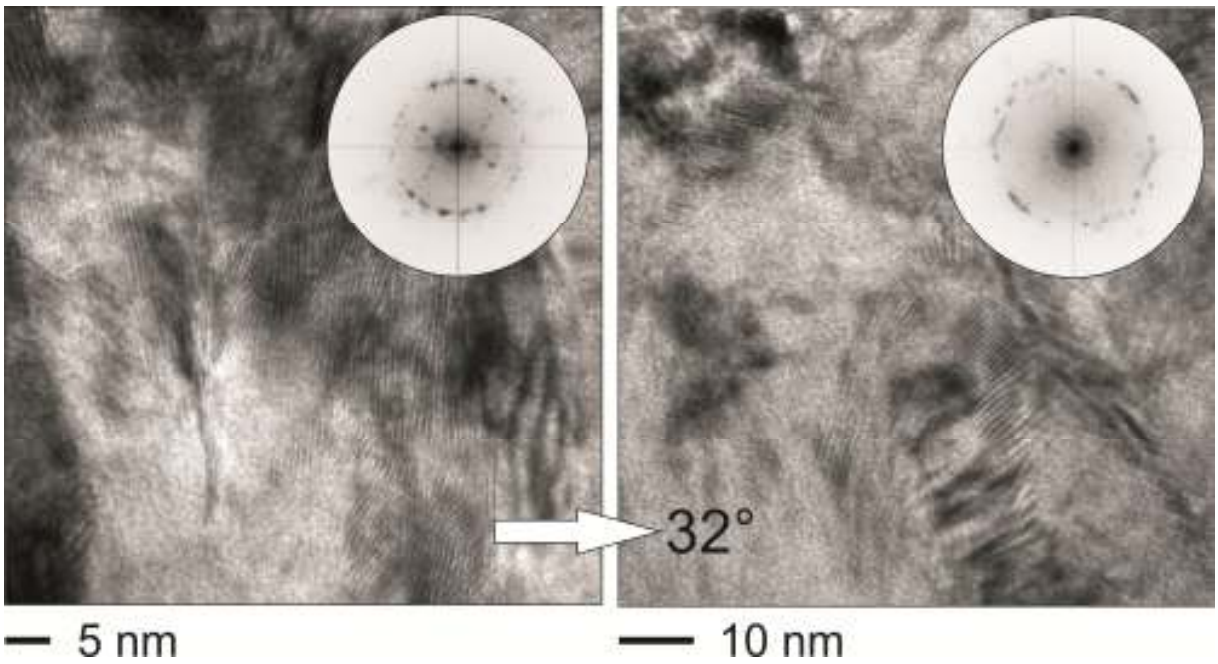

Figure 28: HRTEM micrographs recorded at the transition region in which the relaxation occurs. Both micrographs are dominated by a contrast which occurs due to the overlapping of small grains. Futhermore, the polycrystalline nature of the regions is evident in the FFT pattern given as insets.

Figure 28 depicts two HRTEM micrographs recorded at the transition region. Two different zone axes are selected for detailed examination (zone axes are selected according to the MgO substrate). Note that some Moiré contrast may appear to be twinning at first glance, such as when two grains are oriented symmetrically. For this reason, observations in different directions are essential. In both HRTEM micrographs, the superposition contrast is dominant. Diffuse stripes are visible in the FFT patterns, resulting from the superposition of crystalline but misaligned grains via double diffraction and a Moiré effect, respectively. The stripes run randomly in all directions. This agrees with the polycrystalline nature of the $Fe_{70}Pd_{30}$ film. Small grains were oriented randomly, with many misfit dislocations in between. In addition, no symmetry plane could be found in either FFT pattern, disproving the presence

of twinning. Thus, the introduction of misfit dislocations is concluded to be the prominent relaxation mechanism for the investigated thin films. The results are in good agreement with the micrographs published by Kühnemund et al[51], where the misfit dislocations were also determined to be the stress relaxation mechanism in the case of vapor deposited $Fe_{70}Pd_{30}$ films.

f) Rh Buffer Layer:

The artificial single variant bct martensite state could be stabilized up to 1.2 µm thickness, but a functional fct phase was still not achieved. As the next step, an Rh buffer layer that exhibited an in-plane lattice parameter closer to those of fct $Fe_{70}Pd_{30}$ was selected (a_{Rh} = 0.380 nm a_{fct} = 0.382nm).

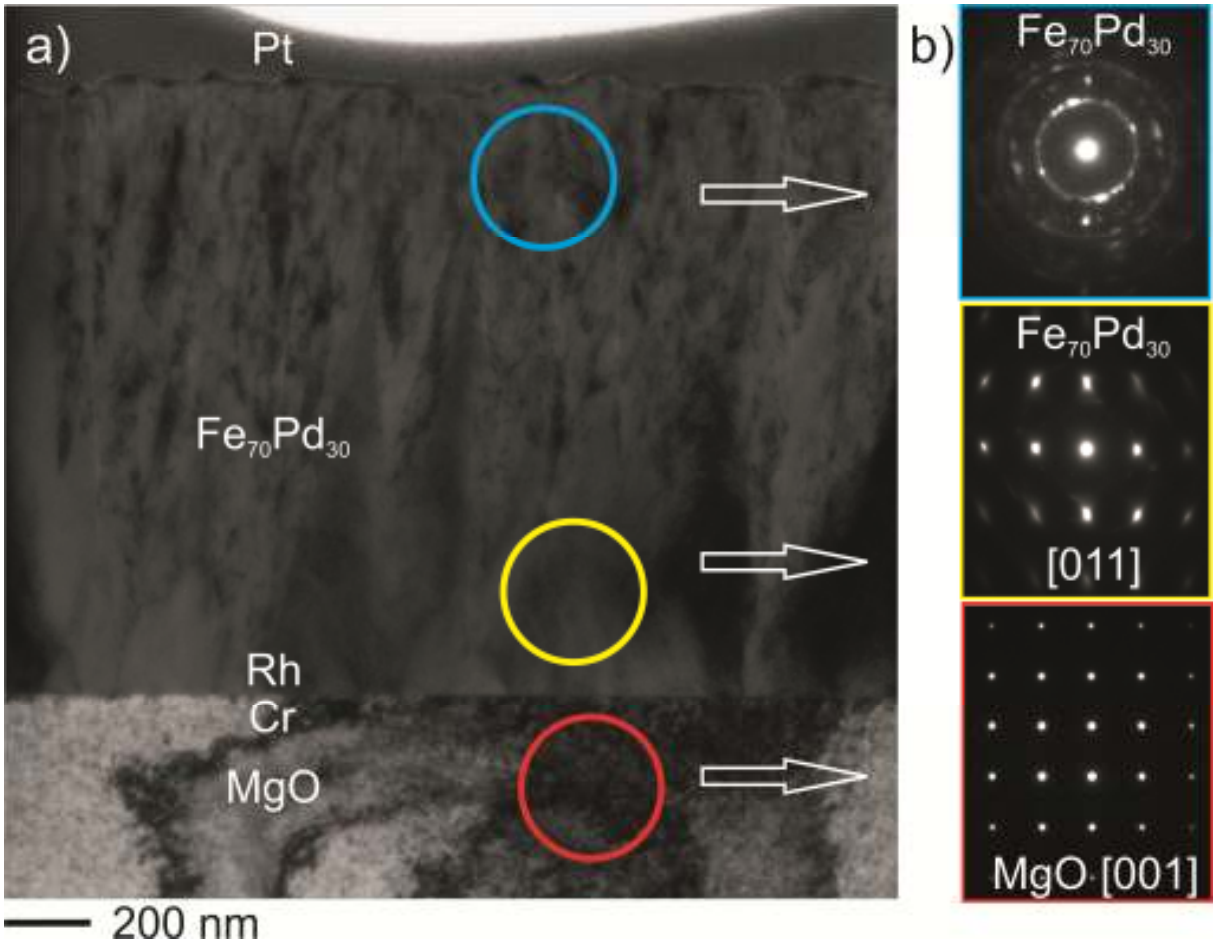

Figure 29: a) Cross sectional bright field TEM image of the heterostructure. b) SAED patterns showing the partial epitaxial growth of the $Fe_{70}Pd_{30}$ thin film.

Figure 29a depicts the bright field TEM image of the MgO/Cr/Rh/$Fe_{70}Pd_{30}$/Pt heterostructure. The SAED patterns given in Figure 29b reveal the partial epitaxial growth of the $Fe_{70}Pd_{30}$ film. Similar to the 3 µm thick sputtered film on the Au buffer layer, the film again relaxes to a polycrystalline bcc type structure at some distance from the substrate. However, the single variant region is significantly thicker, in comparison to the Au buffered film. The critical

thickness for the stable region was determined as 1.2 µm for the Au buffer layer. With the Rh buffer layer, this critical thickness decreased to ~500 nm. This strong deviation can be explained by the sputter behavior of the Rh buffer layer. In this particular case, a 50 nm thick Rh buffer layer was sputtered onto a Cr adhesion layer, with similar sputter parameters as for Au. Figure 30a shows the phase contrast image (HRTEM) recorded at the interface region. No clear sign of a 50 nm thick buffer layer can be detected, nor do the FFT patterns show a crystalline nature for the buffer layer (not shown). Energy filtered imaging reveals the Cr layer but, again, the Rh buffer layer cannot be identified (Figure 30b). Although a tilting series was performed, no separated buffer layer was observed using conventional TEM methods. Figure 30c shows the EFTEM elemental maps and the interdiffusion/dissolution of the buffer layer into the $Fe_{70}Pd_{30}$ film. The HRTEM micrographs showed no sign of a change in the expected d-values of $Fe_{70}Pd_{30}$. Hence, no ternary phase was indicated. A bulk/volume diffusion of Rh may have occurred in the functional film. This type of diffusion phenomenon might cause pinning sites, and could hinder the twin boundary movement in functional devices. In addition, free standing films cannot be achieved, because selective etching of the buffer layer is not possible.

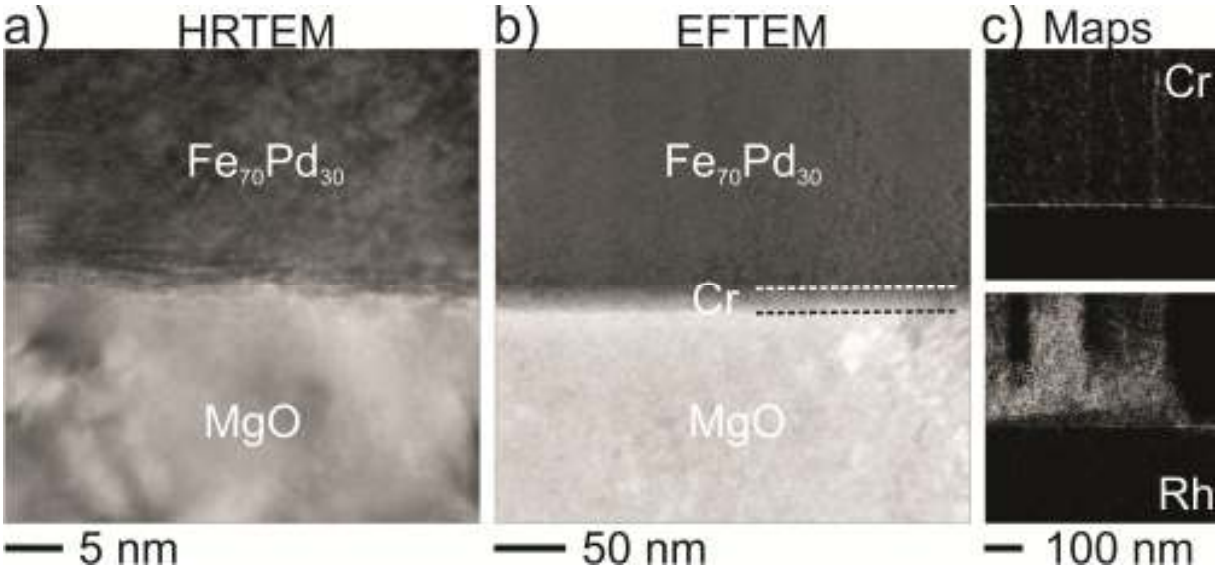

Figure 30: a) HRTEM micrograph recorded on the interface region showing no presence of a 50 nm thick Rh buffer layer. b) Using an energy filter, the Cr adhesion promoter becomes visible. c) EFTEM elemental maps showing the interdiffusion of the Rh buffer layer in the $Fe_{70}Pd_{30}$ film.

Table 4 depicts the measured d-values for the polycrystalline region. Again, the film clearly relaxes to the bcc type structure. This kind of relaxation is manifestly reproducible for these sputtered films. Again, the small grains overlap at the single- to poly-crystalline transition region, leaving behind multiple misfit dislocations. Hence, the relaxation mechanism is again determined as misfit dislocations, and not as a result of nanotwinning. The SAED patterns recorded at the buffer interface again reveal the bct type growth of the $Fe_{70}Pd_{30}$ film. The tilting experiments give a calculated $(c/a)_{bct}$ ratio of 1.06.

Table 4: Measured and calculated d-values for the possible structures in the $Fe_{70}Pd_{30}$ system.

BCC d/(hkl) ⇩	BCT d/(hkl)	FCC d/(hkl)	FCT d/(hkl)	Calculated d/(hkl)
0.212/(0 1 1)	0.214/(1 0 1)	0.217/(1 1 1)	0.217/(1 1 1)	0.212
0.150/(0 0 2)	0.203/(1 1 0)	0.187/(0 0 2)	0.191/(2 0 0)	0.149
0.123/(1 1 2)	0.161/(0 0 2)	0.133/(0 2 2)	0.182/(0 0 2)	0.124
0.106/(0 2 2)	0.144/(2 0 0)	0.113/(1 1 3)	0.135/(2 2 0)	0.106
0.095/(0 1 3)	0.126/(1 1 2)	0.108/(2 2 2)	0.132/(2 0 2)	0.094

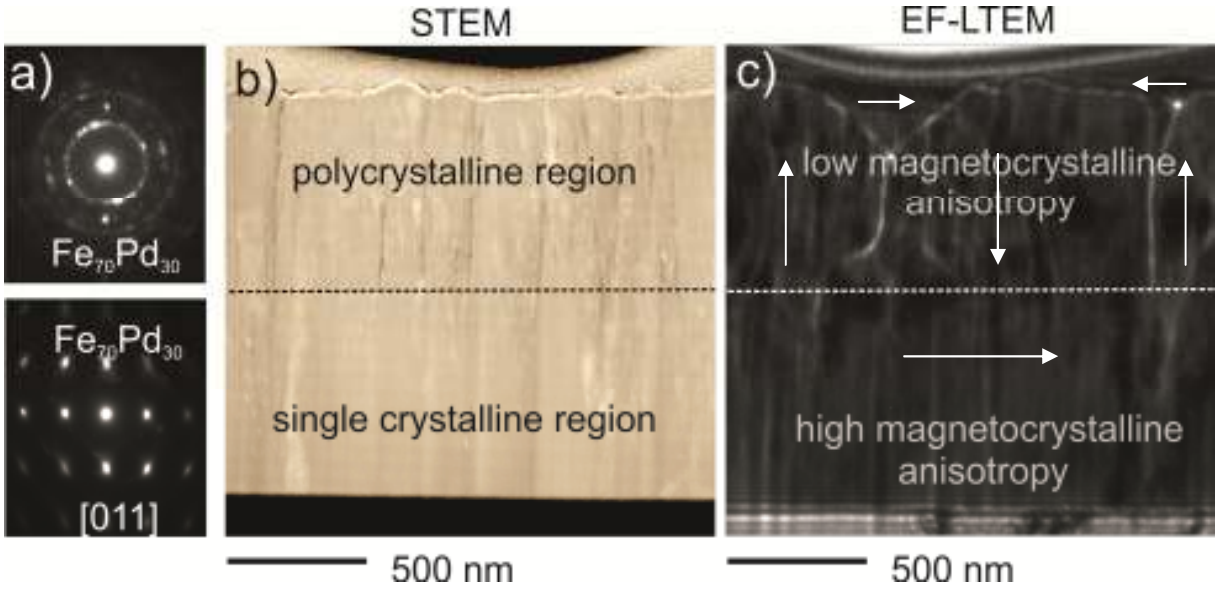

Figure 31: a) SAED patterns displaying the difference between single- and polycrystalline regions. b) STEM micrograph showing the microstructural changes across the growth direction, and c) EF-Lorentz microscopy images correlate the structural data with the magnetic nature of the film.

Figure 31 shows the interrelation of the real and magnetic structure of the sputtered film. The STEM micrograph reveals clear differences between the microstructure of the polycrystalline and single crystalline states. The energy filtered-LTEM micrograph depicted in Figure 31c shows no sign of any magnetic domain walls for the single variant region. However, magnetic domain walls become visible towards the film surface. This finding is in good agreement with the previous results. Note that no magnetic domain walls are indicated in the film grown in the single variant state on the Au buffer. However, the polycrystalline film sputtered onto Au without any adhesion promoter showed the presence of closure domain walls.

The high magnetocrystalline anisotropy in the single variant region results in an area consisting of only one magnetic domain, which exhibits an in-plane magnetization. Therefore, no magnetic domain walls were visible. Note that the $Fe_{70}Pd_{30}$ system has biaxial magnetocrystalline anisotropy. The two short and easy axes are oriented in a plane

respective to the projection direction. The polycrystalline region showed no preferred orientation of the crystals. Hence, the magnetocrystalline anisotropy component vanishes (becomes weak) and the magnetoelastic component of the magnetic anisotropy dominates, which gives rise to the formation of the closure domain walls. A possible domain configuration is given in Figure 31c, but precise determination of the magnetization vectors will require in situ observations.

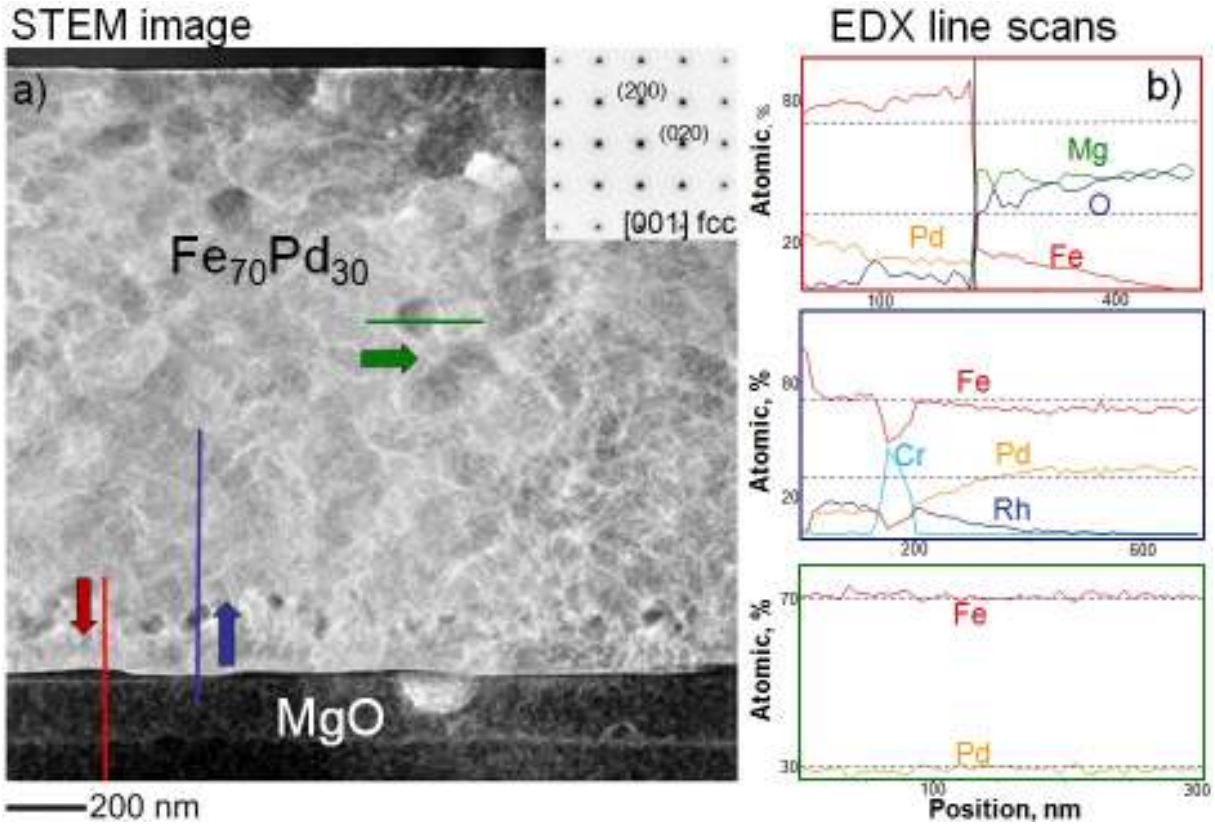

Figure 32: a) STEM image of the $Fe_{70}Pd_{30}$ thick film grown on Cr/Rh buffer layer after heating. b) Nanoprobe EDX line scans recorded from colored lines marked in a).

The transformation behavior of the thin film was investigated using an ex situ heating approach. The film was heated in an Ar atmosphere at 850 °C for 30 minutes and was then quenched in water in order to keep the high temperature state. The phase diagram suggests the formation of the fcc phase at 850 °C. An increase in the grain size is also expected. Figure 32a depicts the STEM micrograph of the cross section. The SAED pattern recorded using the 400 nm aperture on the Fe-Pd film is given as an inset in the image. Both expectations were confirmed from the obtained data. Hence, the grain size increased and the entire film transformed into the fcc type structure. Again, the interface region does not show a clear indication of the Rh buffer layer. However, a mixture of bright/dark contrast is present at the interface, as well as in the film as well. The reason for these different contrast phenomena was explored using nanoprobe line scans performed in scanning mode.

The line scans in Figure 32b reveal fluctuations in the individual element concentrations. Arrows in the STEM micrograph depict the directions in which the line scans were performed. The scan marked in red clearly shows that the Fe diffuses into the MgO substrate. Again no ternary phase of Mg, O, or Fe is indicated. Pd remains in the sputtered Fe-Pd film. The α-Iron has the highest diffusivity at 910 °C and the 850 °C tempering temperature selected for tempering is close to this value. Touloukian et al. calculated these values as 0.0512 x $10^4 m^2 s^{-1}$ and 0.0565 x 10^4 $m^2 s^{-1}$ for 850 °C and 910 °C, respectively[52]. The diffusivity range is determined as 200 nm for Fe.

The scan marked in blue reveals that the Cr adhesion layer also shows interdiffusion. The Cr layer dissolves from the interface region, and agglomerates in the $Fe_{70}Pd_{30}$ thin film. Dark clusters just above the substrate interface indicate these Cr agglomerates. On the other hand, the diffusivity of Cr into MgO was experimentally determined by Dologlou[53], who showed that the Cr reaches its highest diffusivity at temperatures of around 1200 °C, which is a value far below that which we selected in our in situ experiment. Therefore, Cr would not be expected to diffuse into MgO. In addition, the dissolution of Rh into the $Fe_{70}Pd_{30}$ film was again detected via EDX analyses. The results support the EFTEM maps depicted in Figure 30c. No sign of Cr or Rh is found up to a thickness of 400 nm. Hence, the contrast variation near the $Fe_{70}Pd_{30}$ surface cannot be explained by the diffusion of the buffer, nor by the adhesion layer. Elemental analyses also show no change in the Fe:Pd ratio (i.e., the line-scan labeled in green). In most cases, the STEM micrographs are dominated by the Z-contrast, as discussed in the experimental section. However, residual diffraction contrast is inevitable. Different alignments of the grains cause different scattering angles, and this change can be detected via the HAADF detector. Hence, this micrograph shows that the diffraction contrast has become the determining contrast mechanism. For this reason, elemental maps and/or scans are crucial to these types of analyses and must be performed as supplementary tests in order to understand the contrast behavior.

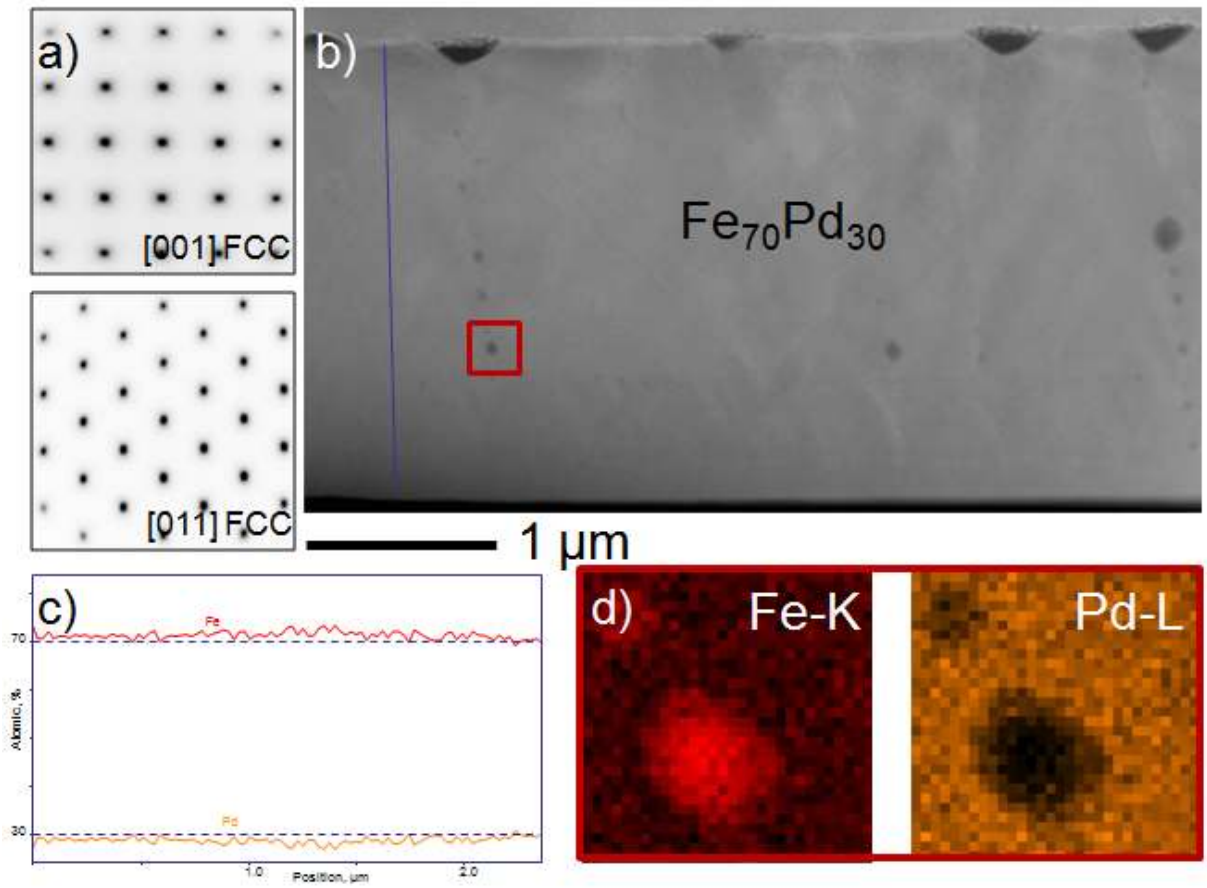

Figure 33: a) SAED patterns recorded on $Fe_{70}Pd_{30}$ thick film. b) STEM image of the free standing film. c) EDX line scan recorded from the line marked in blue in b) and d) STEM-EDX elemental maps taken from the indicated in the region red box (the SAED pattern originated from a tilting experiment).

Another attempt was made to remove the film from the buffer layer. These processes and their consequences have to be considered according to the scope of electron microscopy investigations, since freestanding films will be required for functional devices. In this case, the film was released from the substrate by chemical etching with KI/I_2 solution (11.5 g I_2/50g KI/1 liter H_2O). The presence of a substrate or a buffer layer would block the motion of the film; hence, complete etching of the buffer layer is important. The film is also under stress due to its growth on a sacrificial buffer layer and the removal of this layer will release that stress, which could affect the microstructure. The deviation from the ideal $Fe_{70}Pd_{30}$ stoichiometry will also affect the function in a negative manner. Figure 33b displays the STEM micrograph of the same film depicted in Figure 29a. The freestanding film shows no indication of the residual substrate. Nanoprobe line scans, indicated by the blue marked line, reveal that the 70:30 ratio is almost completely maintained for Fe and Pd (Figure 33c). The film has also retained its fcc type structure (Figure 33a). However, dark regions located on preferred lines are noticeable in the STEM micrograph. The elemental maps from nanoprobe EDX measurements are given in Figure 33d, showing the dark regions to be Fe-rich precipitates. The reason that the precipitates are linearly agglomerated can be identified from

Figure 31b. Columnar growth of the film can be identified in the STEM micrograph. Since these column boundaries exhibit higher free energy than does the rest of the film, the first precipitates occur at these boundaries. Similarly, at the surface, the free energy is higher than is the free energy inside the film, so the precipitations occur primarily at the intersection points of the surface and column boundaries. This can also be clearly seen in the STEM micrograph. When the film is heated to 850 °C for 30 minutes, the Fe atoms are excited, primarily in the precipitated columnar boundaries. Removal of the buffer layer apparently triggered the movement of Fe atoms, and precipitates occurred. These precipitates are undesirable, as they would block the shape memory behavior.

h) Ir Buffer Layer

The use of the Rh and $Mn_{80}Ir_{20}$ buffer layers with an in-plane lattice parameter close to the fct $Fe_{70}Pd_{30}$ failed to achieve the desired fct phase with high stability. In the case of Rh, an interdiffusion of the buffer layer was also observed. Materials with lattice parameters close to the fct phase were selected (i.e., for those values, the growth of an fct phase was foreseen), but only bcc/bct phases were obtained in all cases. These results can be explained by the local minima of the bcc structure calculated by the DFT method (Figure 27). We assume that this minimum dominates for our sputtered films, although an artificial strain is introduced at the buffer interface via the mismatching of different lattices.

The Ir buffer layer was selected as the next approach; in other words., an alloy with an in-plane lattice parameter between Au and Rh[2] (a_{Ir} = 0.293 nm). The reason for this selection is quite straightforward. The XRD measurements performed on the Ir buffer showed a possible distortion of the fcc lattice. Figure 34a depicts the bright field TEM image of the MgO/Cr/Ir/$Fe_{70}Pd_{30}$/Pt heterostructure. SAED patterns recorded on the marked regions show a partial epitaxial growth of the $Fe_{70}Pd_{30}$ film. At the buffer interface, the $Fe_{70}Pd_{30}$ film grows completely epitaxially with the fcc structure (i.e., the yellow framed SAED pattern at the bottom). Even after tilting the specimen by 45°, no tetragonal distortion of the unit cell is indicated. This conclusion is also supported by the XRD measurements[54]. The HRTEM micrographs and the calculated FFT patterns indicate that the epitaxial growth of the $Fe_{70}Pd_{30}$ film is kept approximately 80 nm from the Ir buffer layer interface. The FFT patterns also suggest a small mismatch and a rotation of the $Fe_{70}Pd_{30}$ unit cell with respect to the Ir buffer layer. The rotation is around 4° and the mismatch is 1.7%. The epitaxial relationship between the layers is determined to be:

[2] Author's note: The reason for this selection is simple. The selection of Au led to the growth of a bct type structure. Hence, the selection of a buffer layer with a larger in-plane lattice parameter was neccessary.

$$(001)_{MgO}\,(001)_{Cr} \parallel [110]_{Cr}[100]_{MgO}$$
$$(001)_{Ir}(001)_{fcc} \parallel [100]_{fcc.}[100]_{Ir}$$

The additional SAED patterns recorded in the regions marked in blue and red in Figure 34a verify that a relaxation occurs. When moving away from the buffer interface, the film relaxes to a polycrystalline type structure. The transition region from single- to polycrystalline areas contains all three variants of fct crystals, as indicated by the splitting of the fundamental reflections in the blue framed SAED pattern, marked with arrows in the enlarged section. Note that the position of one variant of the formed triplet is parallel to the observation direction, and is therefore not visible in the given projection. The polycrystalline region (red framed region at the top) exhibits a tetragonal structure. The tetragonal distortion of the unit cell can be seen by the splitting of the $<110>_{bcc}$ reflections into $(101)_{bct}$ and $(110)_{bct}$ and the $<112>_{bcc}$ reflections into $(112)_{bct}$ and $(211)_{bct}$; i.e., the enlarged section in the respective SAED pattern. The tetragonal phase was identified from the possible bct and fct structures, by comparing the intensity distribution of the concentric rings on the SAED patterns with the calculated intensities from the structure models[26]. For both structures, one ring (corresponding to one d-value) is missing, namely $(002)_{bct}$ and $(111)_{fct}$. The missing $(111)_{fct}$ ring for the possible fct phase has the highest intensity of all the other reflections. On the other hand, for the bct phase, the missing $(002)_{bct}$ reflections have the intensity value of 107/1000, according to the calculations dependent on the given structure factors in the literature. The absence of the most intense ring in the SAED pattern is hardly conceivable, and cannot be explained by the presence of a texture. Hence, the structure is assumed to be a bct type.

The EDX elemental maps recorded on the interface region also did not indicate any interdiffusion of the buffer layer into the $Fe_{70}Pd_{30}$ film. The chemical composition of the film was therefore determined to be $Fe_{71(1)}Pd_{29(1)}$ at the interface, as well as in the polycrystalline region.

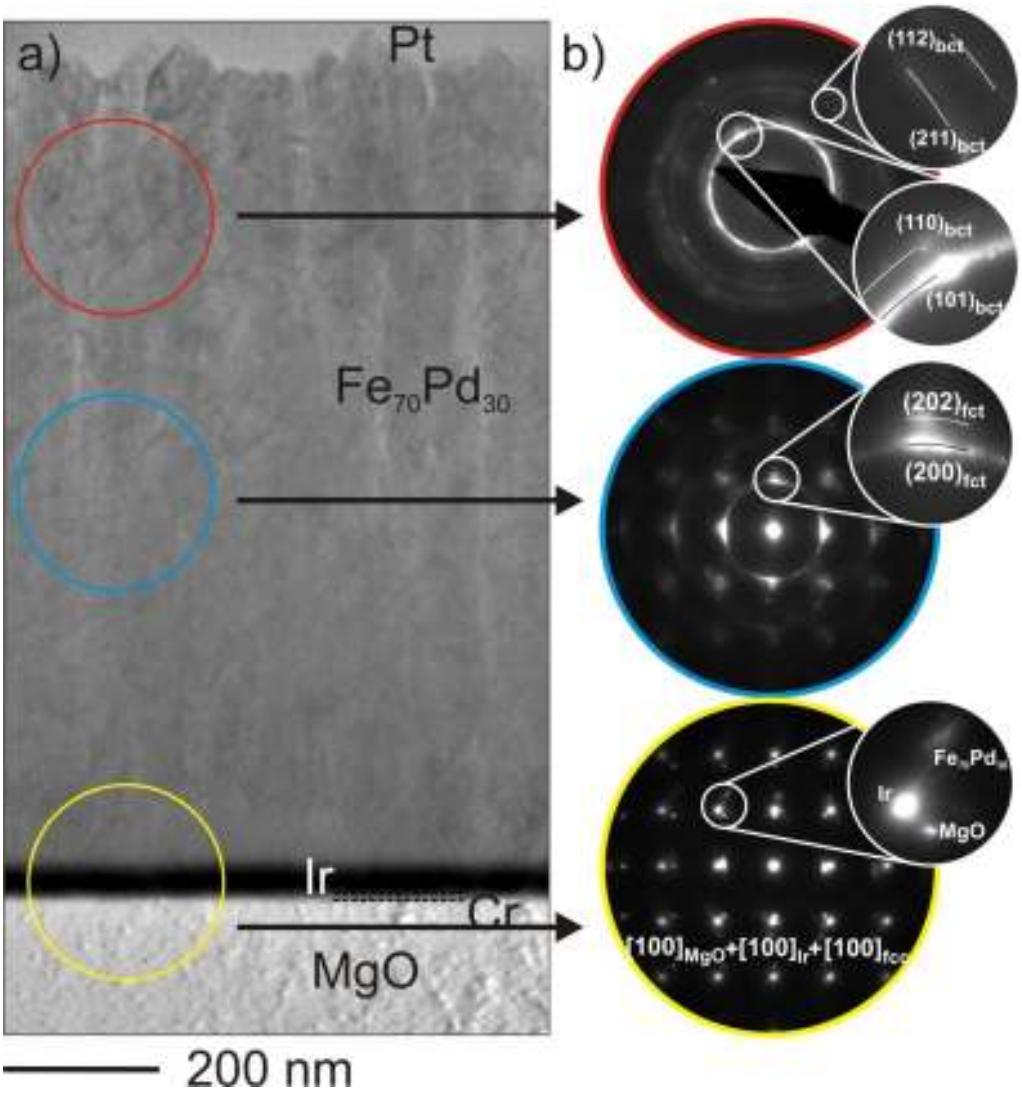

Figure 34: a) BFTEM image of the MgO/Cr/Ir/$Fe_{70}Pd_{30}$/Pt heterostructure. b) Recorded SAED patterns from the marked regions, with an enlarged section to illustrate the peak splitting.

3.2 Polycrystalline Layers

As previously mentioned, another focus of this research was to achieve functional polycrystalline films. Single crystalline films are difficult and costly to fabricate; thus, polycrystalline films attract more interest. The functionality of these films is strongly correlated with their microstructure. For example, the presence of nanoscale precipitates hinders the movement of the twin boundaries in the films, which blocks the SME. In this study, we combined standard TEM characterization of the films with in situ experiments, in order to gain a deeper understanding of phase transitions. The films were sputtered onto SiO_2 substrates.

Figure 35 displays SAED patterns recorded during an in situ heating experiment. At room temperature, the film exhibits a bcc type structure, in support of the previously presented

results. The absence of a buffer layer and the use of higher sputtering rates resulted in the formation of a polycrystalline type structure.

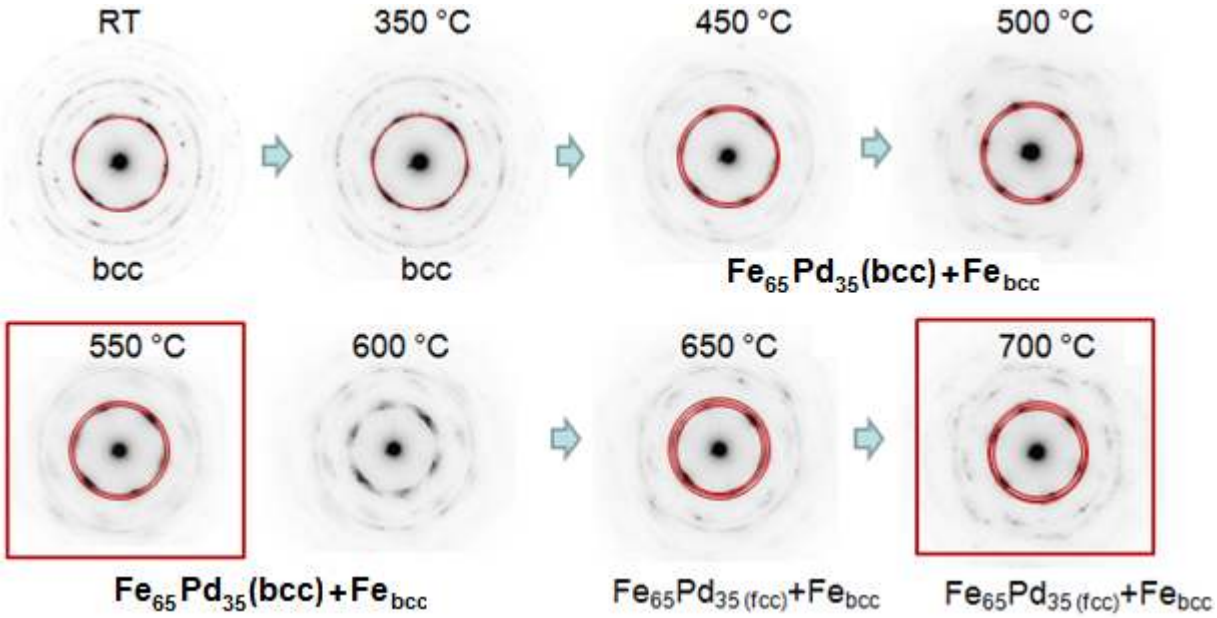

Figure 35: In situ heating of a polycrystalline Fe-Pd sample. A phase transition from bcc to fcc structures was observed.

Increasing the temperature to 350 °C resulted in no change in the deposited bcc structure. Heating above 550 °C gave rise to the formation of a secondary phase, detected via electron diffraction. This is clearly visible in the splitting of the first order reflections in to two, and then in to three rings, which are assigned to the (111) and (200) reflections, first of a $Fe_{65}Pd_{35}$ compound, and to the (110) planes of the bcc Fe phase. The appearance of the additional rings is marked by red circles in the diffraction patterns. An additional texture is also visible in the diffraction data, which could be related to the <110> bcc phase. The EFTEM micrographs and respective Fe and Pd maps show no indication of any precipitation. Instead, a homogenous distribution of Fe and Pd is observed (Figure 36). The reason could be the presence of very small precipitates that were not undetected via EFTEM mapping in the chosen area. The decomposed state of the TEM sample is stable up to 650 °C. From 450 °C to 650 °C, the solubility of Pd in α-Fe increases; this should result in an increase of α-Fe lattice constants. This change, however, is very small and could not be detected within the limits of experimental error.

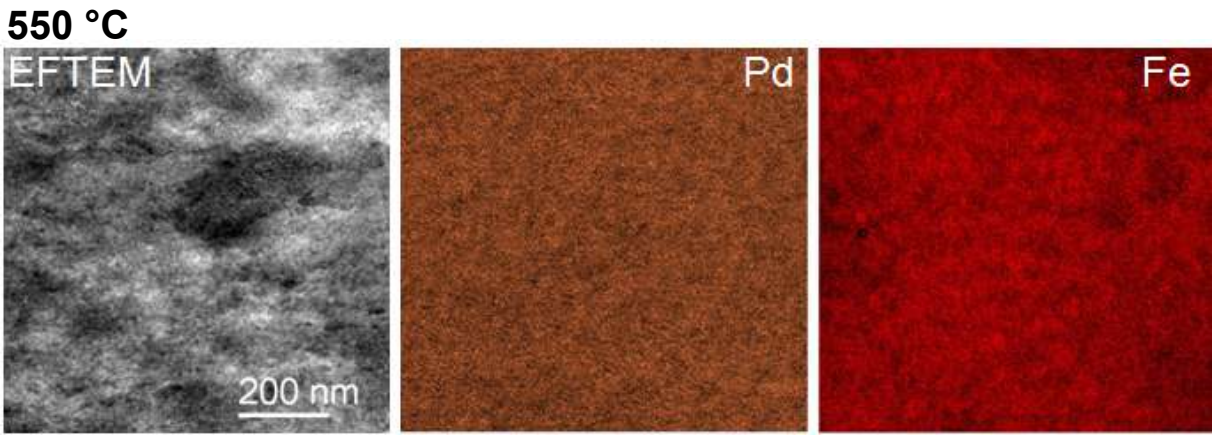

Figure 36: EFTEM micrograph of the sample heated to 550°C. Fe and Pd maps show a homogenous distribution of Fe and Pd.

A significant grain growth was also observed, and continued to be even more pronounced up to 850 °C. Bechtold et al. reported different magnetic properties for the films before and after annealing (ex situ)[55].

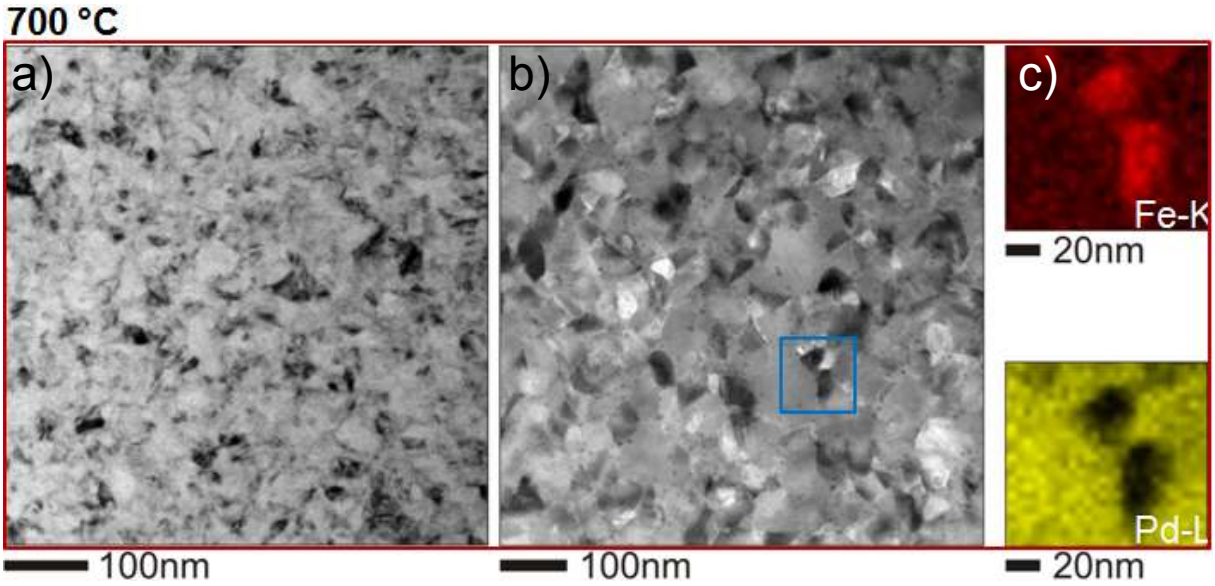

Figure 37: STEM micrographs of a) ex situ and b) in situ heated polycrystalline samples. In both cases, after heating the sample to 700 °C, Fe rich precipitates can be identified.

Further heating of the sample gave the expected transformation from the bcc to the fcc phase. However, the d-values deviated slightly from the ideal $Fe_{70}Pd_{30}$. The reason can be identified from the STEM micrographs shown in Figure 37. The micrographs on the left and in the middle show the microstructures of ex situ and in situ heated samples, respectively. The ex situ heated sample was held at 700 °C for 30 minutes and was subsequently quenched. The nanoprobe EDX measurements were carried out after the sample was heated to 700 °C and then cooled to room temperature. In both micrographs, similar microstructures can be observed. The dark areas can be identified as Fe-rich areas. The sizes of these precipitates vary in the two micrographs. Smaller precipitates are observed by

TEM in the quenched sample than in the in situ thermally treated sample. The atoms do not have enough time for diffusion after quenching, so the precipitates on the left micrograph are more confined.

The measured d-values agree with Vegard`s law, and the chemical composition of the matrix is determined to be bcc-$Fe_{65}Pd_{35}$. The d-value of the additional concentric ring appearing above 600 °C is correlated with the bcc Fe. Note that EDX analyses can only be performed at room temperature, since the thermal drift is too high at elevated temperatures. Thus, the illuminated area is not the same as the region in which the experimental data were recorded. The background and shadowing effects of the heating holder are also too strong.

However, the diffraction experiments can be conducted during the in situ heating. The thermal drift is sufficiently small for the case of conventional SAED. Table 5 summarizes the list of measured d-values.

Table 5. Measured and assigned d-values of phases obtained at different temperatures.

RT	**350 °C**	**450 °C**	**550 °C**	**650 °C**	**750 °C**	**850 °C**
0.211 nm(110) bcc	0.210 nm (110) bcc	0.221 nm (111)$Fe_{65}Pd_{35}$	0.221 nm(111)$Fe_{65}Pd_{35}$	0.222 nm(111) $Fe_{65}Pd_{35}$	0.218 nm (111)fcc	0.218 nm (111) fcc
0.150 nm(200) bcc	0.149 nm (200) bcc	0.207 nm (110) Fe	0.203 nm(110) Fe	0.205 nm(110) Fe	0.189 nm (200) fcc	0.187 nm (200) fcc
0.121 nm(211) bcc	0.123 nm (211) bcc	0.146 nm (200) Fe	0.145 nm (200) Fe	0.191 nm (200) $Fe_{65}Pd_{35}$	0.134 nm (202) fcc	0.134 nm (202) fcc
0.105 nm(202) bcc	0.106 nm (202) bcc	0.120 nm (211) Fe	0.134 nm (220) $Fe_{65}Pd_{35}$	0.146 nm (200) Fe	-	0.109 nm (222) fcc
-	-	-	0.119 nm(211) Fe	0.136 nm (220) $Fe_{65}Pd_{35}$	-	-
-	-	-	-	0.118 nm(211) Fe	-	-

The sample is cooled down to room temperature after heating. As expected, the reverse transformation from fcc to bcc occurs. No additional feature is detected in the SAED pattern. Comparison of the recorded SAED pattern (Figure 38a) with the one (Figure 35 at RT) before heating clearly shows that the grain size increases after heating. This is evident from the strong Bragg intensities located on the concentric ring. In addition, a preferred <110> orientation of the grains is noticeable.

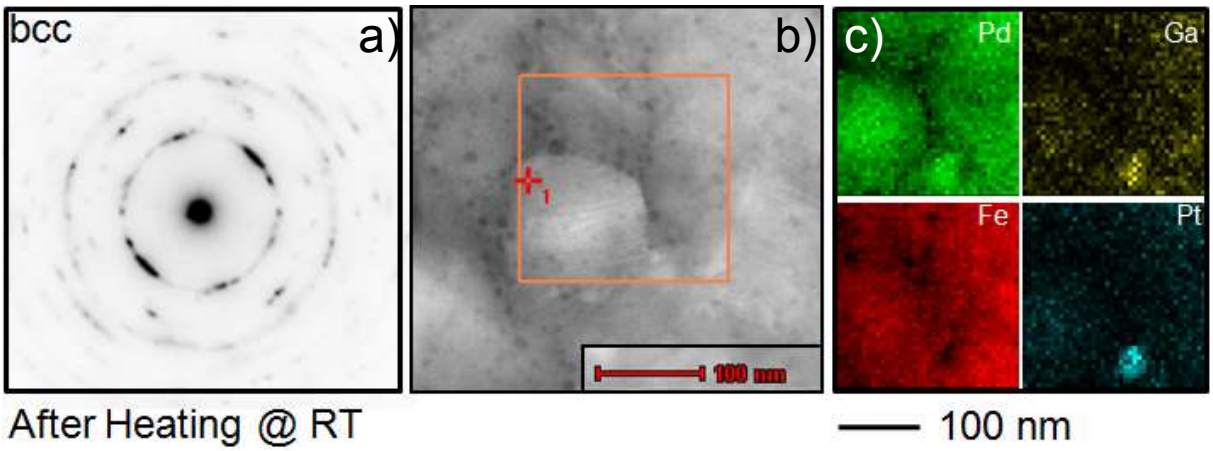

Figure 38: a) SAED pattern showing the reverse transformation to the bcc phase after heating, b) STEM micrograph and c) elemental maps measured from the marked region in b).

Elemental maps measured from the marked area in Figure 38b display the distribution of Fe and Pd. The amounts of Fe and Pd change in a correlated manner. Note that the colored elemental maps are based on the detected intensity of the given elements by the EDX detector. The calculated atomic percentages for Fe and Pd are similar over the entire map. The contrast is dominated by the thickness in the given STEM micrograph. In addition, the presence of Ga and Pt originating from the FIB preparation is detected.

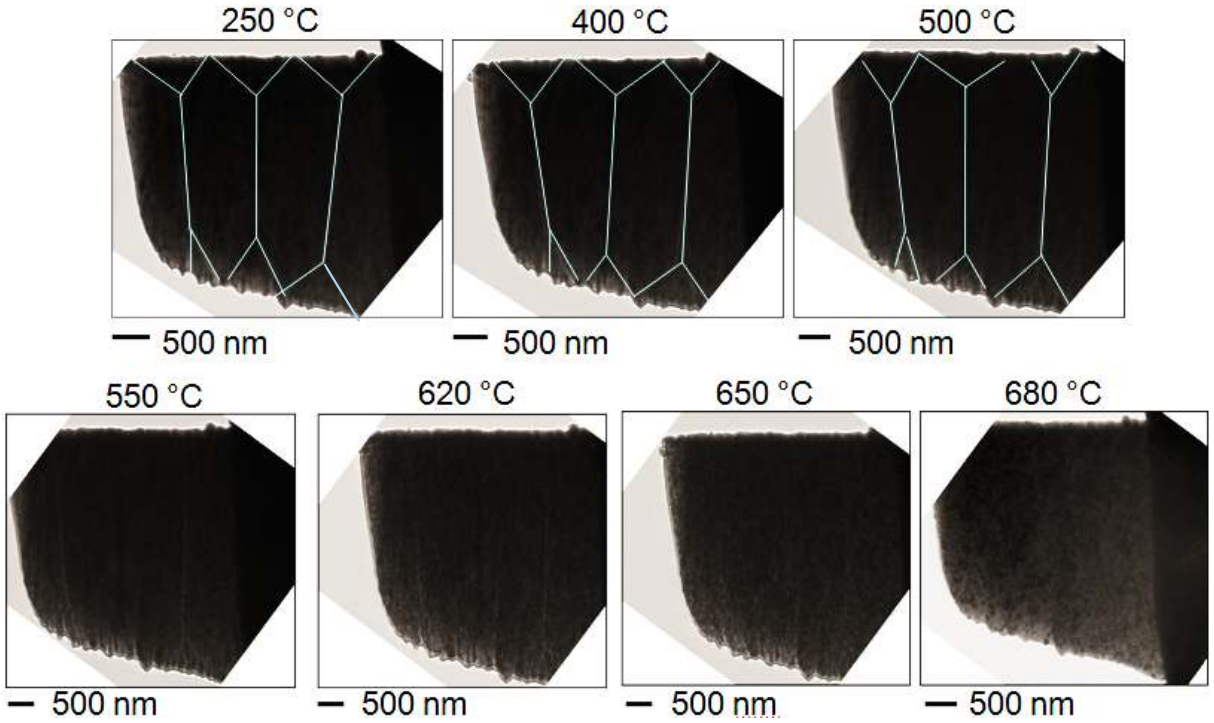

Figure 39: LTEM micrographs recorded during in situ heating experiments. Magnetic domain walls vanish at around 600 °C, which is well above the Curie temperature reported in the literature[56].

Similar heating experiments were also performed in the LTEM mode: the objective lens was switched off and the domain wall observations were performed using Lorentz lenses. Upon

heating, the domain walls did not move, but slowly vanished. At around 650 °C, no presence of magnetic domain walls was visible (Figure 39). This is because the sample, upon reaching the Curie temperature, becomes non-magnetic. Note that the Curie temperature of the $Fe_{70}Pd_{30}$ was reported in the literature to be around 400 °C[57]. The significant difference in both values is due to the slight change in the composition, as discussed earlier. The TEM sample exhibits a significantly lower thickness than that of the sample reported in the literature, which causes a deviation in the measured Curie temperature.

3.3 Fe-Pd-Pt System

A promising way to enhance the properties of Fe-Pd alloys is by alloying a third element. However, little information regarding ternary Fe-Pd-X materials is avaible. For example, the addition of Co and Ni to Fe-Pd resulted in an increase in saturation magnetization[58]. The addition of Co shifted the fcc-fct transformation temperature to higher values, whereas Ni addition lowered that temperature. These results suggest that the relative stability between fcc and fct phases is affected by the composition. The impact of the Fe content and the valence-electron number on the structure is not well understood and still requires comprehensive investigation.

TEM investigations were focused on the structure and on the composition of these films at the nanoscale. Subsequently, the films were cooled below the transformation temperature in situ, and the changes in morphology and microstructure were monitored. Another point of interest was the substrate/film interface. Although the substrates are SiO_2 and amorphous (no epitaxial growth possible), an interdiffusion between the film and the substrate can take place due to the post-annealing of the films. This would block the complete removal of the layer, which is an essential feature of fully functional films.

All samples were produced using a combinatorial magnetron sputtering system (CMS 600/400LIN, DCA). The films were deposited by co-sputtering from elemental targets on thermally oxidized Si substrates. The synthesis and XRD measurements were performed at Ruhr University by our cooperation partner (Professor Ludwig).

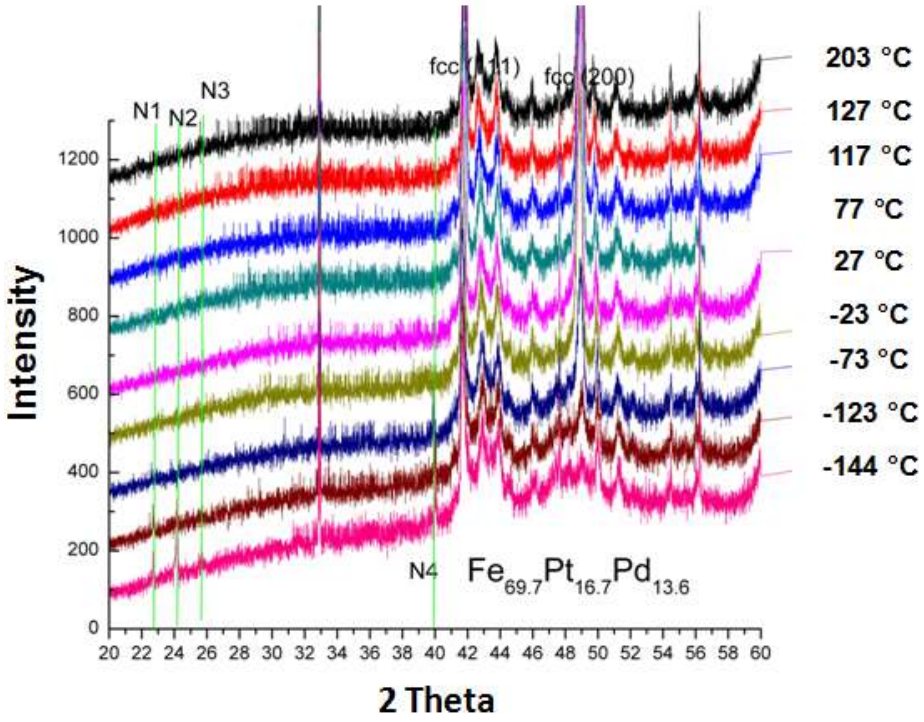

Figure 40: Temperature dependent XRD diffractogram of Fe-Pd-Pt alloy.

The results of the temperature dependent XRD measurements are depicted in Figure 40. The diffractogram shows that the fcc phase is stable at elevated temperatures, as expected. ((111) and (200) peaks are indexed). Cooling the sample to below -23°C caused a phase transformation from the highly symmetrical fcc parent phase to a less symmetrical fct phase. Further cooling did not result in a phase transformation, although small peaks arose in the XRD pattern (labeled with N1, N2, N3, and N4 below -123°C). One possible explanation was the presence of a modulation in the structure; however, no study has yet reported any modulation in an Fe-Pd system.

HRTEM and SAED investigations were performed to clarify the structure at the nanoscale level. Low temperature experiments are very sensitive to the humidity of the environment, which can cause a formation of crystalline ice that is visible in XRD patterns. The hexagonal ice exhibits its characteristic peak positions at around 23°, 24°, and 25°, which are close to the values that are visible in the XRD pattern. The profiles of the peaks are also too sharp to have been modulated. Broader peaks are expected for cases of modulation; however, our peaks were rather sharp, indicating a highly crystalline phase, such as ice.

Another open question is whether the alloy is completely ternary. This is the point at which STEM-EDX elemental maps play a pivotal role in the TEM investigations. The film composition was determined to be $Fe_{69.7}Pd_{13.6}Pt_{16.7}$ via EDX measurements performed in SEM.

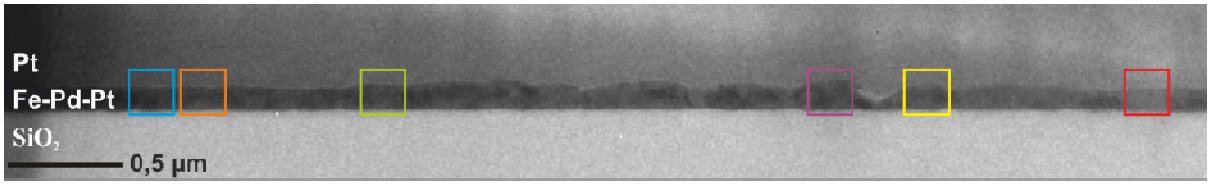

Figure 41: Bright field TEM image of the entire lamella. Heterostructure labeled on the image (SiO_2/Fe-Pd-Pt/Pt).

The SiO_2/Fe-Pd-Pt/Pt heterostructure is displayed in Figure 41. The cross-sectional bright field TEM image shows SiO_2 and Pt protection layers from the FIB preparation. The different nature of the Pt protection layers is due to the different deposition parameters used when cutting the sample via FIB. Low rates are selected for the regions that are in contact with the Fe-Pd-Pt layer, in order to avoid Pt implementation. The colored squares indicate the regions in which the SAED patterns were recorded. Note that the SiO_2 substrate has an amorphous character and, for this reason, does not cause additional reflections in the SAED pattern. The thickness of the layer varied between 90 and 100 nm. This low thickness makes these specimens challenging objects for selected area electron diffraction experiments, since the selected area aperture exhibits a diameter of 250 nm. A selection of SAED patterns are depicted in Figure 42. All patterns indicate that the film consists of fcc, fct, and bcc phases. The calculated d-values are also in agreement with the XRD measurements. The presence of an fct phase can be explained by the cooling experiment performed before the sample was prepared by FIB for TEM investigations. Thus, the film is not completely transformed to an fcc type, and some fct crystals remain untransformed. As a complete transformation was expected, we assumed that the SiO_2 substrate blocked the full transformation.

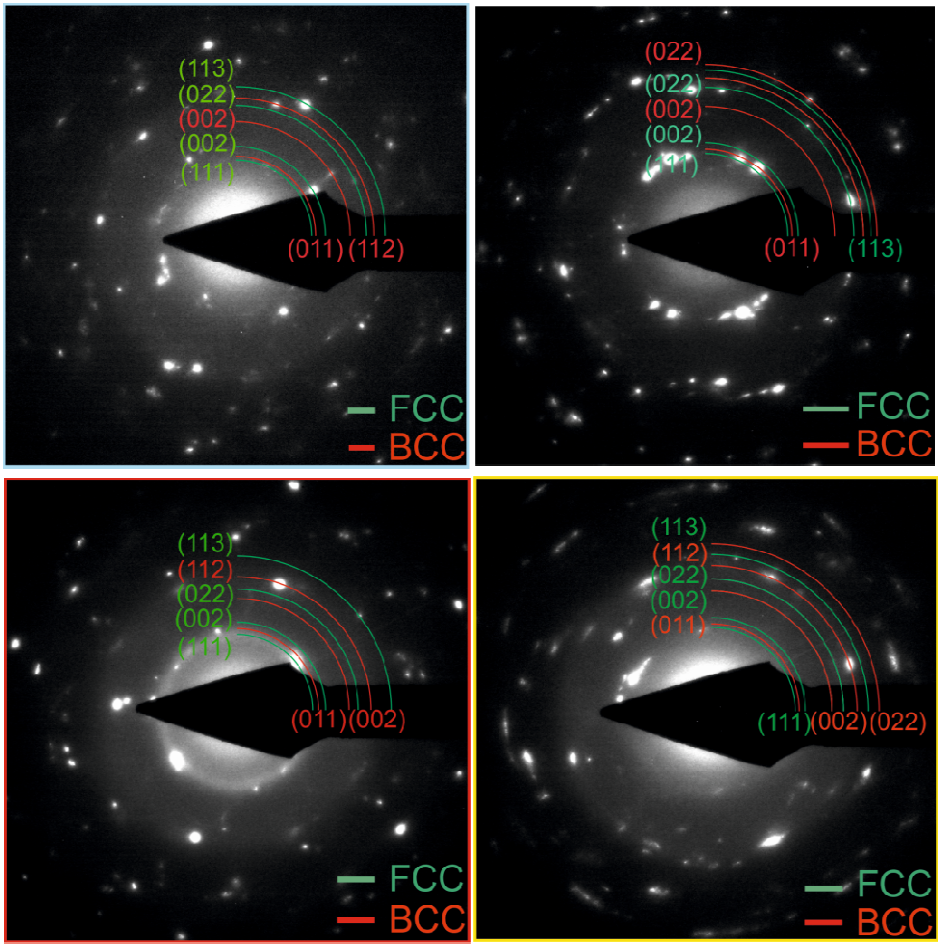

Figure 42: Selected SAED pattern recorded on the colored squares in figure 41. The film exhibits a mixture of bcc, fcc and, in one region, fct crystals (not shown).

Nanoprobe STEM investigations were performed across the film. Point measurements with small spacing in between were selected instead of line-scans, in order to have higher count numbers for the EDX detector. Figure 43 shows the selected results of the chemical investigations. The regions from 1 to 4 (labeled in the right corner of the spectra) are the same areas in which the SAED patterns were recorded in Figure 42. Related concentrations are written on the image. The Si peaks originate from the substrate, and the Cu peak is a result of the TEM grid; these peaks are not taken into account when calculating the Fe, Pt, and Pd concentrations. The EDX-spectra show that the Pt amount is higher for the right part of the film. The reason could be the applied welding process with Pt during FIB cutting. In this process, the welding is applied between the FIB micromanipulator and the sample before it is stuck onto the special support, and is implemented from the edge of the sample. Hence, the Pt amount at the edge of the sample is higher. Micrographs taken from the right side of the film also show small inclusions at the top of the film. The SAED patterns verify that these inclusions originate from Pt (forming a concentric ring with a corresponding d-value of Pt). In addition, local deviations from the target stoichiometry are recognizable. However, it has to

be kept in mind that Pt is used for adhesion for the applied FIB cut, and these observed deviations could be a result this practice.

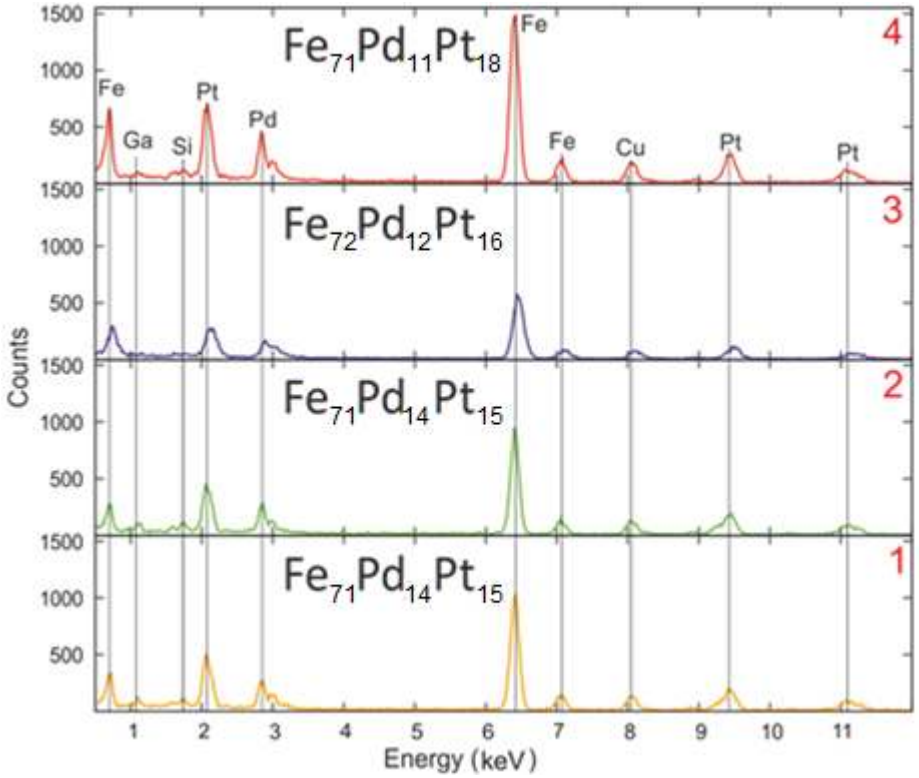

Figure 43: EDX spectra measured from the regions in which the SAED experiments were performed.

The SAED investigations showed that most parts of the sputtered film exhibited a polycrystalline nature. Hence, the film consists mainly of randomly oriented grains of bcc, fcc, and fct crystals. Some areas also showed a strong <100> texture for the bcc phase. (the third SAED pattern depicted in Figure 42). Further scanning and tilting of the sample in diffraction mode revealed a small fragment of the sample to be single crystalline.

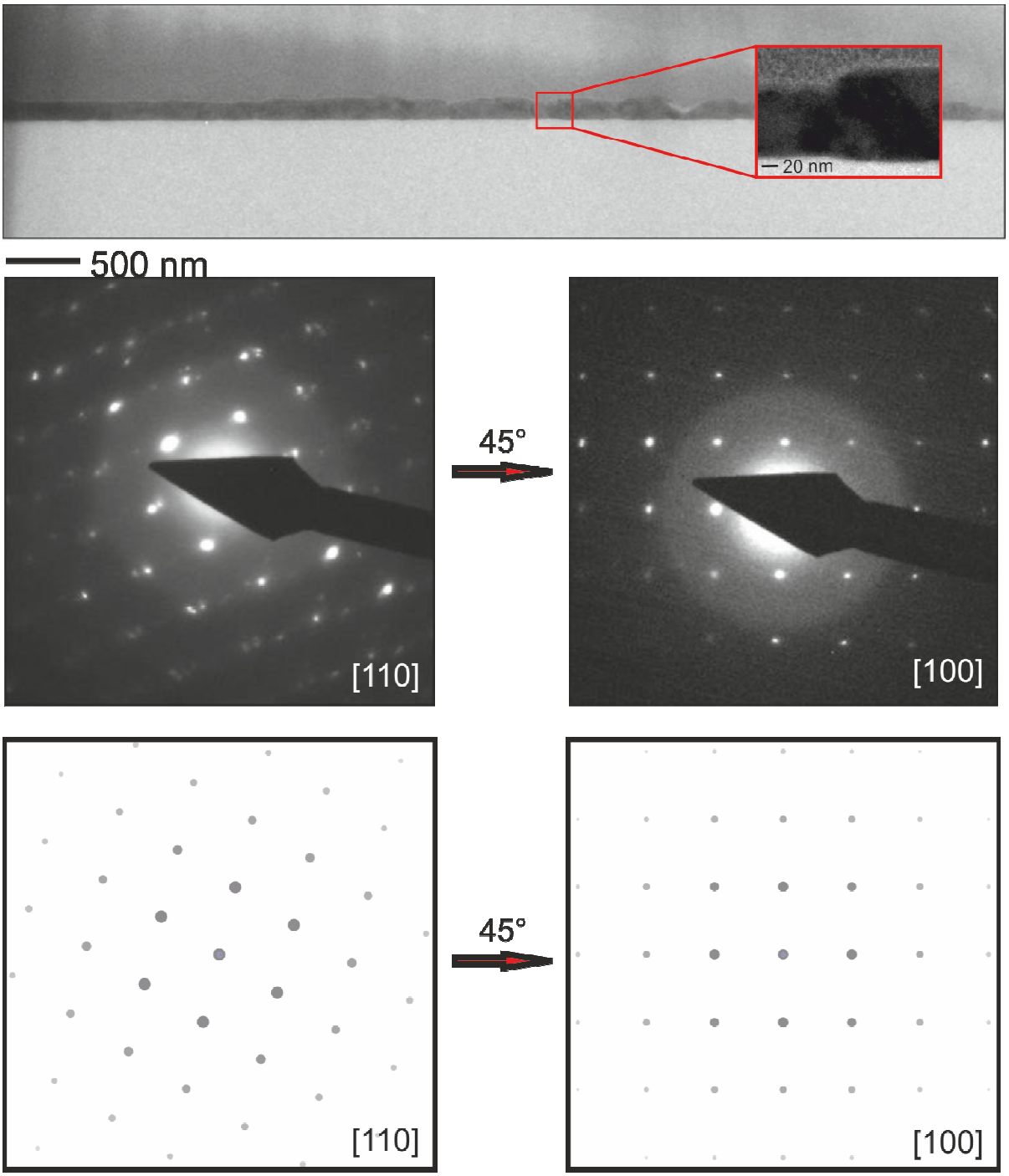

Figure 44: BF-TEM image of the overview: the micrograph of a single crystalline region with higher magnification is presented as an inset (top). Experimental and simulated diffraction patterns were recorded in two different zone axes (bottom).

Figure 44 depicts the BF-TEM image, while the inset shows the regions in which elemental maps and diffraction experiments were performed. The homogenous region is highly textured in the [110] zone axis of the fcc phase. The zone axis changes from [110] to [100] via the tilting experiment. The experimental and simulated diffraction patterns are in good agreement. Additional reflections can also be identified in the SAED pattern recorded along

the [110] zone axis. These reflections are likely to originate from the neighboring grain. They vanish after tilting the specimen, in agreement with this assumption.

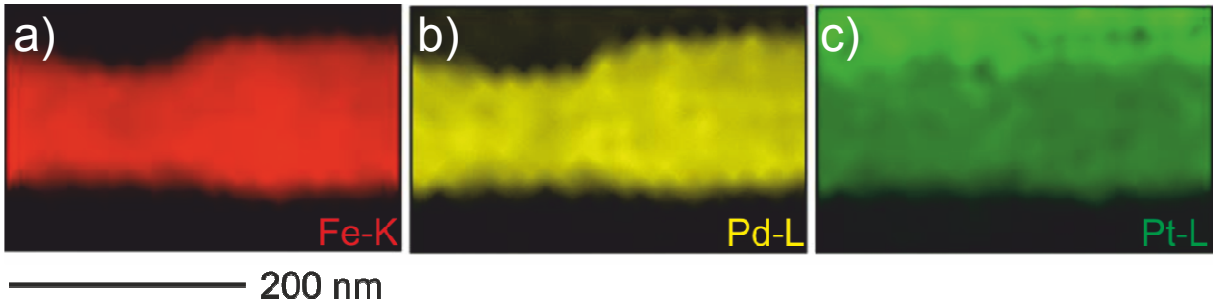

Figure 45: Elemental maps of a) Fe, b) Pd, and c) Pt. Homogenous distribution of the elements are identified.

Elemental mapping was carried out using STEM-EDX from the single crystalline region. Homogenous distribution of Fe, Pd, and Pt elements were verified. No precipitates were observed. Hence, a region around 250 nm in diameter was identified as being completely ternary. Later, in situ cooling experiments were particular focus on the single crystalline region, were conducted. Cooling analysis was performed to investigate the phase change, as well as to compare it with the XRD results.

Figure 46 shows the SAED patterns recorded at different temperatures during an in situ cooling experiment. At first glance, the diffraction pattern did not appear to change upon cooling. However, the splitting of the (011) reflections was noticeable, and is indicated by arrows in the enlarged section of the SAED pattern taken at -95 °C. The additional reflection, which arises during cooling, can be explained by the phase transformation from the fcc to fct phase. The diffraction pattern does not permit differentiation between whether the entire region is completely transformed to the fct phase, or if some crystals remain untransformed. Recall that the diffraction patterns are similar for [001] and [010] directions in the case of fcc and fct type structures. The splitting of the reflections indicates a tetragonal distortion of the unit cell of around 7%. However, the remaining (unchanged) reflections can originate from the fcc or from one of the similar orientations of the fct phase. The observed transformation temperature of -95°C is well above the temperature measured via the in situ XRD experiments. The difference in the two results could originate from the measurement techniques. The TEM measurements are performed on a very confined region, whereas the XRD is integrated throughout the entire volume. The observed difference could be due to this localization of the TEM results.

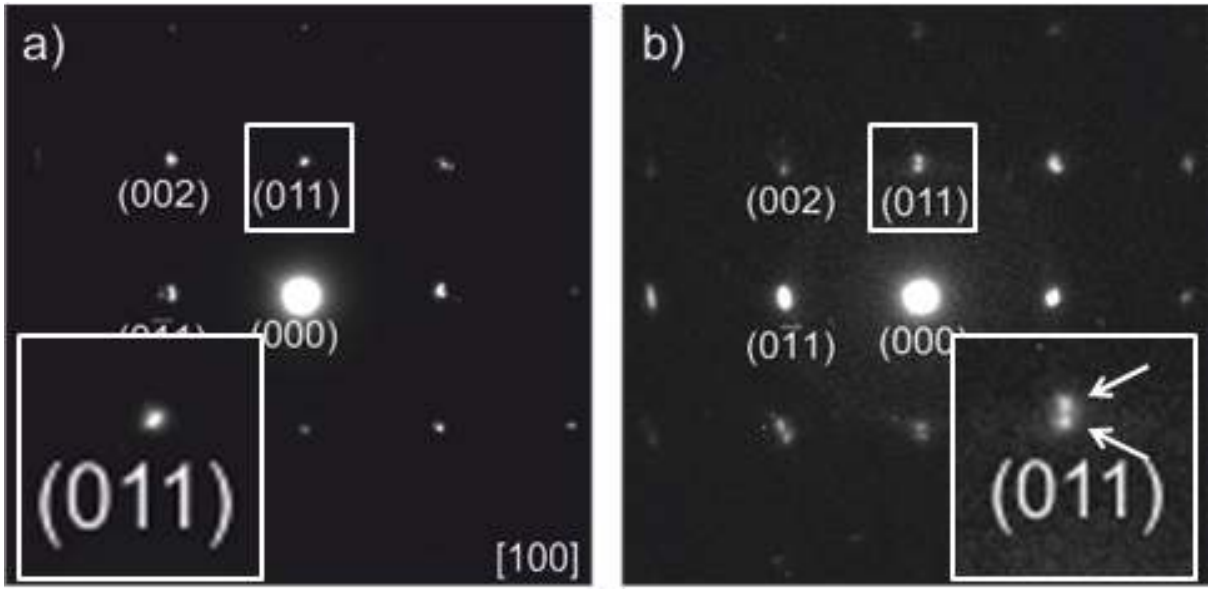

Figure 46: SAED patterns during an in situ cooling experiment. a) room temperature, and b) -95 ºC.

A second explanation is that the additional reflections arose from a neighboring region. Both effects can have consequences for electron diffraction patterns. Firstly, the SAED aperture has a virtual diameter of around 250 nm, which is significantly larger than the desired/optimal size for these films. Secondly, the aperture may not be positioned at exactly the same region when recording the SAED pattern. Note that a repositioning of the aperture is required for in situ cooling/heating experiments because a strong thermal drift is present, due to the large temperature gradient. Further cooling did not result in any additional reflections indicating a modulation. The high thermal drift precluded an HRTEM investigation at low temperatures. For this reason, HRTEM studies were conducted at room temperature.

An HRTEM micrograph recorded on a different region in a similar film and the calculated FFT patterns from three marked regions are shown in Figure 47a. The FFT patterns show the twinned regions and the corresponding twin plane. The twin plane is determined to be $(111)_{fcc}$ and is indicated by an arrow on the figure. The FFT patterns are compared with the simulated diffraction patterns in Figure 47 b-d. The FTT pattern calculated from the blue region (when two variants are in one region) matches the superpositioned diffraction pattern obtained by the overlap of two patterns from two individual variants. The determined values and calculations show that the angle between the twin crystals is 42°, and that the film has an fcc structure. The zone axes are also determined to be [101] according to the results. The SAED pattern is presented as an inset in Figure 47a.

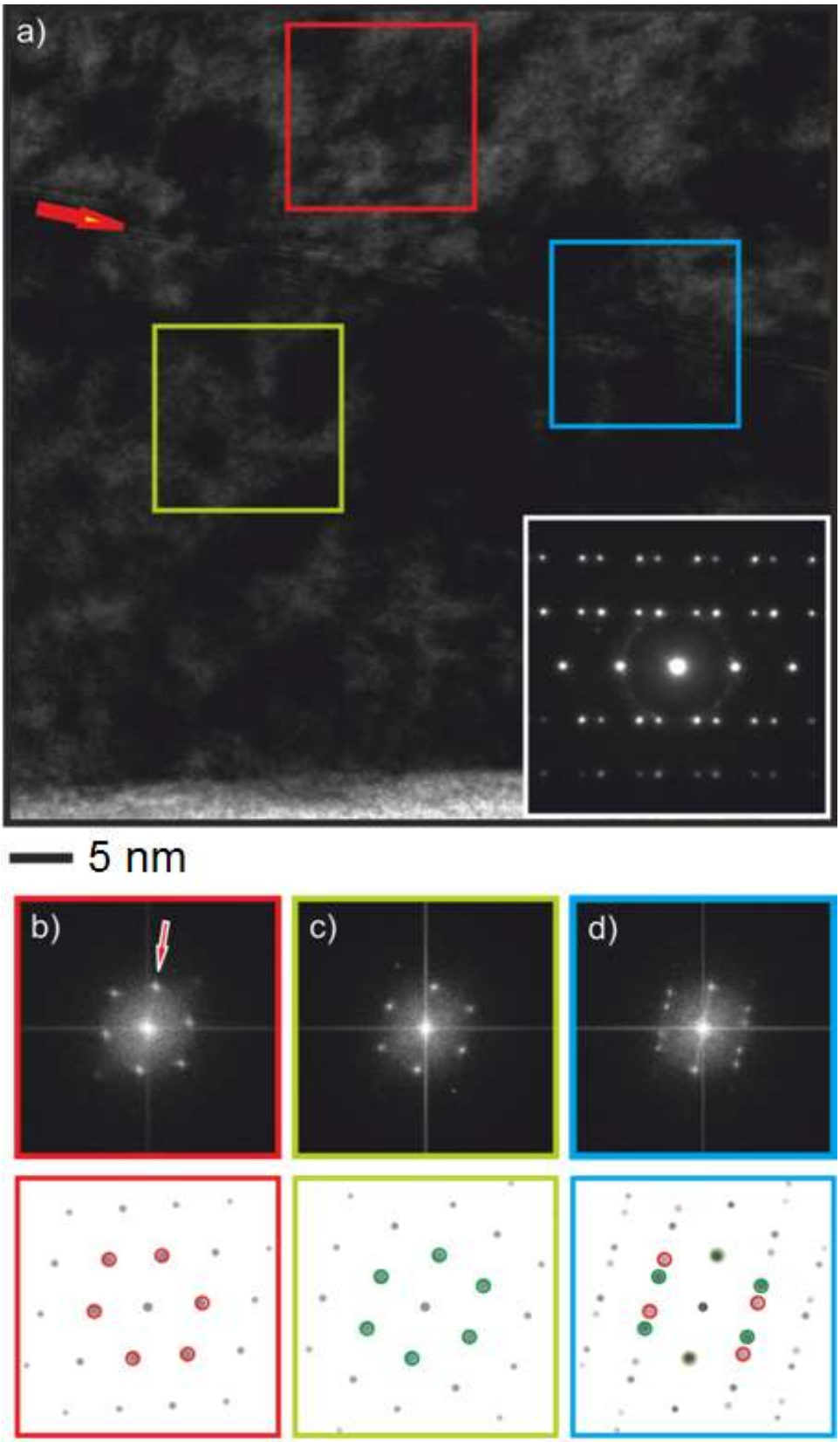

Figure 47: a) HRTEM micrograph, b) and c) FFT patterns calculated from the labeled regions (top) and from the simulated diffraction patterns (bottom). The arrow in b) indicates the twin plane. c) Calculated FFT pattern from the twin interface region (marked in blue) fits well with the superpositioning pattern from b) and c) given in d).

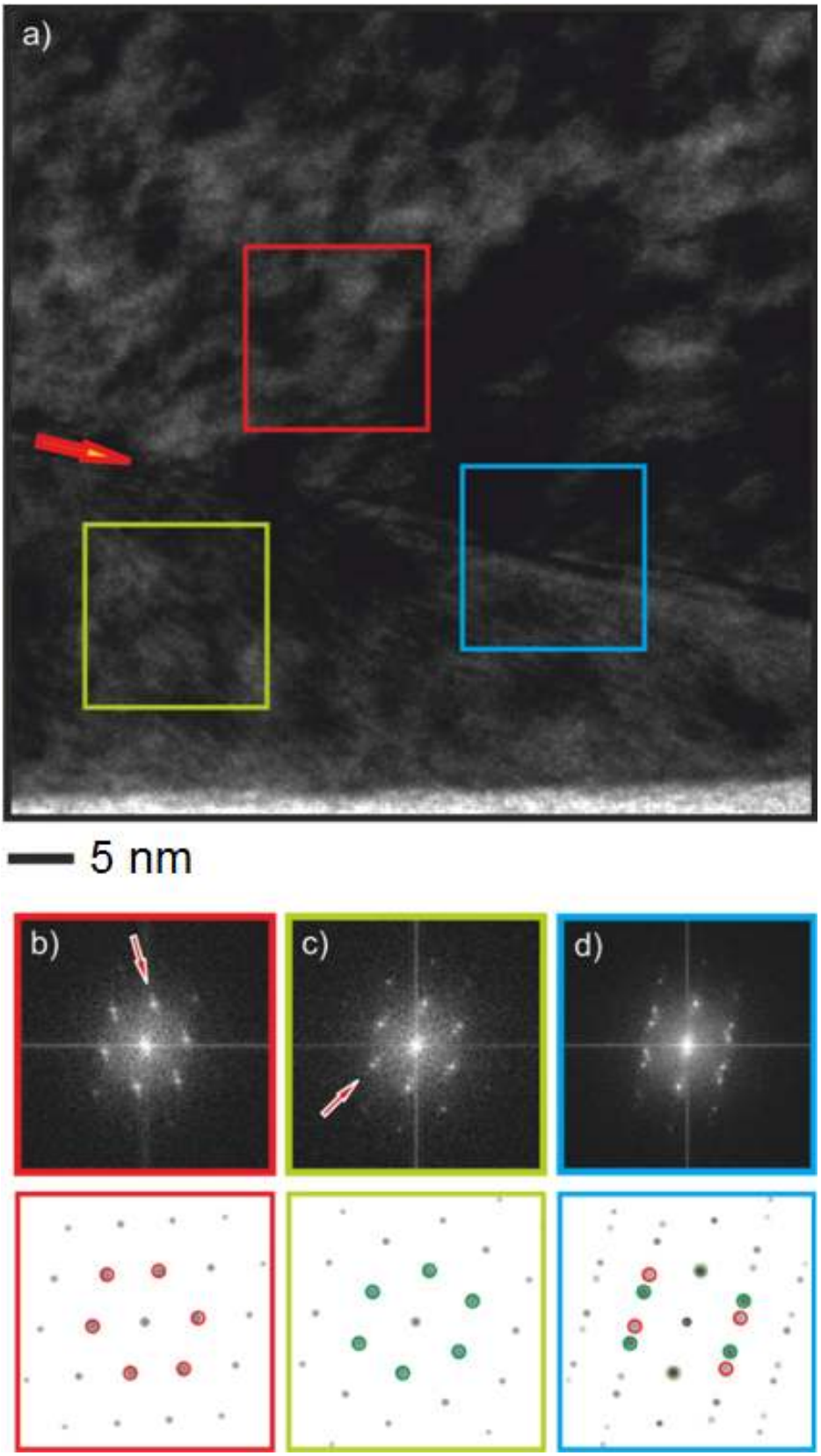

Figure 48: a) HRTEM micrograph, b) and c) FFT patterns calculated from the labeled regions (top) and from the simulated diffraction patterns (bottom). The arrow in b) and c) indicates the splitting of the reflections. c) The calculated FFT pattern from the twin interface region (marked in blue) fits well with the superpositioning pattern from b) and c) depicted in d).

Following the twin boundary across the film, additional structural features are recognized via HRTEM imaging. Similarly as in the previous results, two differently oriented twinned regions and the twin boundary are shown in Figure 47. Interestingly, however, additional spots (marked with arrows) appear around the main reflections in the FFT patterns. Stripes responsible for the splitting can also be identified in the HRTEM micrograph. One possible reason for the splitting of the reflections is the presence of a Moiré pattern (superposition of two crystals on top of each other). However, one would not expect this in this case, because the stripes begin directly at the substrate interface. Consequently, a second explanation is the possible existence of a disordering in each twin variant. This explanation would agree with the expected modulation in the XRD results. A detailed understanding requires a higher resolution, but this type of phenomenon is already known to occur in other magnetic shape memory alloys, such as, Ni-Mn-X Heusler type alloys, and will be discussed in the following chapter.

Figure 49 shows an HRTEM micrograph and the diffraction pattern taken from a Ni-Mn-In-Co metamagnetic shape memory alloy. The structure is twinned and is internally modulated. The similarity of the SAED pattern to the FFT pattern depicted in Figure 48d is obvious. In both cases, the modulation directions of the phases are in the [110] directions with respect to the parent phases (the fcc phase for Fe-Pd-Pt, and austenite for Ni-Mn-In-Co). A third possible explanation is the presence of a premartensitic phase. Note that the films had already been cooled for the temperature dependent XRD experiments. Hence, a residual premartensitic phase during the fcc-fct transformation could be the reason for the additional disorder.

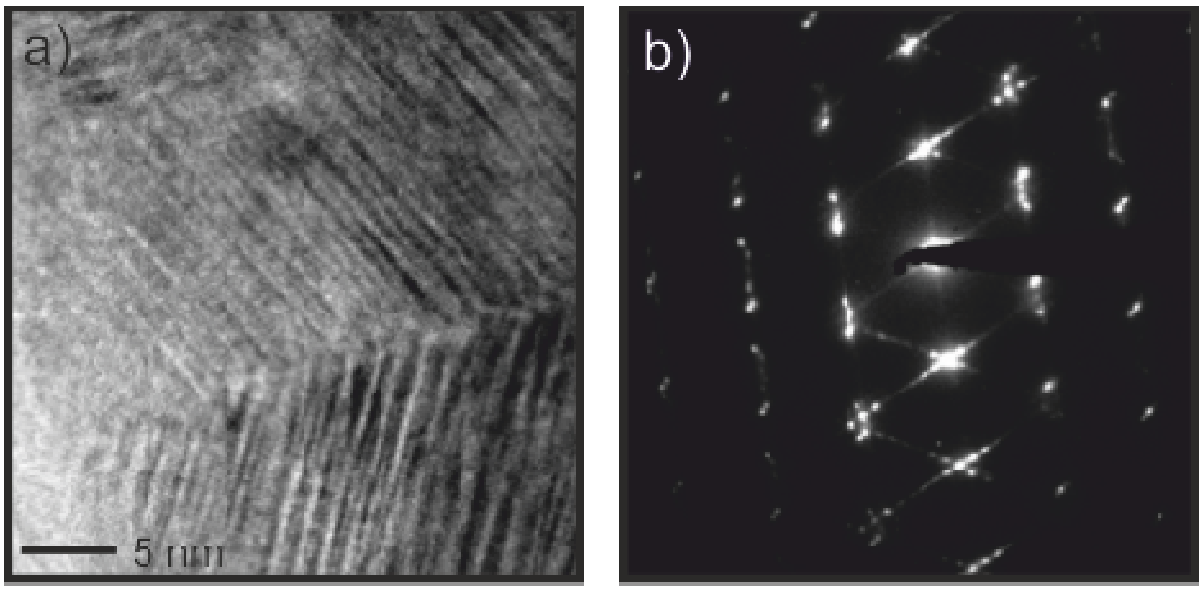

Figure 49: a) HRTEM micrograph and b) the SAED pattern from a Ni-Mn-In-Co alloy. Both HRTEM micrograph and SAED pattern show similarities with the results of Fe-Pd-Pt.

An additional result that supports the occurrence of a phase transformation is the SAED pattern recorded on the twinned region at -122 °C (according to the TEM holder cooling control system). Figure 50 depicts both patterns recorded before the cooling experiment had started (at RT), and at -122 °C. An additional concentric ring occurring in both patterns originates from the Pt layer deposited during FIB preparation. Two marginal changes are noteworthy when comparing the two patterns. Firstly, a systematic change in the reciprocal distance between each variant is observed when cooling the sample. As an example, two line profiles are depicted in Figure 50c. In the fifth row reflections, the differences between both profiles are clearly noticeable. For the SAED pattern recorded at -122 °C, the reciprocal distance becomes smaller in comparison to the pattern recorded at RT. On the other hand, in the SAED pattern captured at room temperature, all the third row reflections coincide and the reciprocal distance between the reflections in the other rows originating from each variant stays consistent.

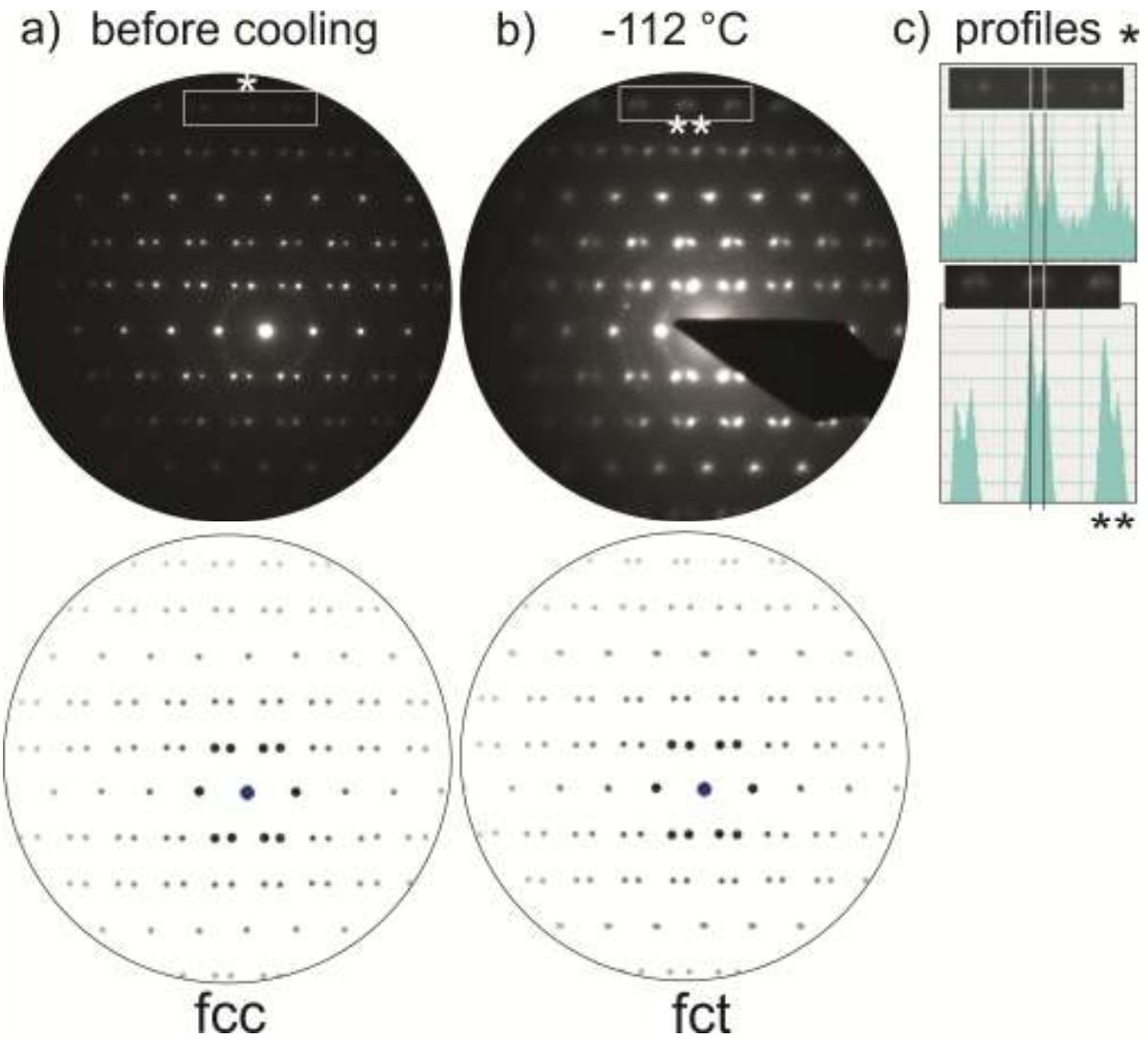

Figure 50: SAED patterns recorded at a) RT, b) at -112 °C and c) corresponding line profiles measured from the white framed rectangles in a) and b). A clear difference in the reciprocal distances can be identified.

Note that the reciprocal distance stays constant only in the case of cubic models. In the event of a tetragonal distortion, the reciprocal distance varies between each variant's reflections, and it is particularly visible in higher order reflections. This is exactly the situation here, and it indicates the occurrence of the phase transformation in the thin film. The simulated diffraction patterns also support this finding and match with the experimental data very well.

A second remarkable feature in the SAED pattern (at -112 °C) is the preferred elongation of the individual reflections. There could be multiple reasons for the elongation of these reflections. The presence of the strain during cooling is one possible answer, but another reason could be that additional disordering in the film occurs during cooling. The reciprocal elongation direction is determined as <110>* from the electron diffraction pattern. This diffuse scattering in the $[110]_{fcc}$* direction has been reported previously, and is referred to as the premartensitic phase[59]. Grüner et al. also reported a phonon softening in these directions for similar films (unpublished, private communication). The premartensitic phase is characteristic of those alloys during fcc-fct transformations, and was studied in detail by Oshima et al. Since no indication of a modulation was observed for the film, the additional peaks observed in the XRD diffractogram are most likely caused by artifacts.

3.4 Summary

Three different approaches have been proposed when investigating Fe-Pd based FSMAs using TEM. In the first step, epitaxially grown films were observed using TEM with a particular focus on interface analyses. Lorentz microscopy (Fresnel Imaging) techniques were also applied, in order to correlate the crystal structure with the magnetic structure of the samples. The epitaxial $Fe_{70}Pd_{30}$ sputtered films showed different growth behaviors on different metallic buffer layers. The structure of the films also showed dependence on the thickness and on the sputtering. These changes were supported by in situ observations.

Films prepared on an Au buffer layer without any adhesion promoter layer were polycrystalline in the bcc type. Use of a Cr adhesion promoter resulted in a<110> bcc texture of the sputtered film. Changes in the sputtering parameters (selecting lower sputtering rates) gave rise to an artificial single variant martensitic state for first time. By tilting the sample a tetragonal distortion of 7% of the bct unit cell was detected.

Similar approaches were repeated by selecting different metallic buffer layers with various lattice parameters close to those of the desired fct phase of $Fe_{70}Pd_{30}$. $Mn_{80}Ir_{20}$, Rh, and Cr

buffer layers gave similar results. The films grew to a limited thickness, with a partial bct structure. All films relaxed to a polycrystalline bcc structure. Only the Ir buffer layer yielded the desired fct phase, but with limited thickness (100 nm). All the results are summarized in Table 6.

Table 6: Summary of growth behavior of $Fe_{70}Pd_{30}$ films on different buffer layers.(Op) stands for the optimized sputtering parameters.

Buffer Layer	Au	Cr/Au	Cr/Au (op)	Cr/Au (op)	Cr/$Mn_{80}Ir_{20}$ (op)	Cr/Rh (op)	Cr/Ir(op)
Sputtered Thickness	1.2 µm	1.2 µm	1.2 µm	3 µm	100 nm	1.2 µm	400 nm
Epitaxial Thickness	-	-	1.2 µm	1.2 µm	100 nm	500 nm	100 nm
Experimental Misfit	-	-	0.5 %	0.5 %	7.1 %	2.3 %	1.7 %
Epitaxial Structure	bcc poly-crystalline	<110> textured bcc polycrystalline	bct marten-site	bct marten-site	bct marten-site	bct marten-site	fct marten-site
c/a ratio	1.0 (0.1)	1.0 (0.1)	1.07 (0.1)	1.07 (0.1)	1.03 (0.1)	1.06 (0.1)	1.05 (0.1)
Relaxation Type	-	-	-	bcc poly-crystalline	-	bcc poly-crystalline	bct poly-crystalline
Interdiffusion	no	no	no	no	no	yes	no

As shown in Table 6, the growth of fully epitaxial layers is only festered in the case of low sputtering rates (labeled “op”). Coherent epitaxial growth requires that the lattice parameters of an already-deposited film are reorganized by the newly arriving atoms. A certain diffusion length is needed before these adatoms find their ideal positions. A low rate is therefore beneficial, as defects rarely occur at the interface. However, even when using the lowest

sputtering rates, rough interfaces were detected by HRTEM. These defects accumulate with increasing thickness, resulting in a relaxation of films in bc(c/t) type structures. The commonly proposed relaxation mechanism is $(111)_{fcc}$ twinning, but it is favored for the transformation from bcc to fcc phases. Note that none of the sputtered films relaxed to an fcc type structure. In the case of an Ir buffer layer, the relaxation occurred from an fc(c/t) to bc(c/t) phase; hence, a back transformation has to be considered. In other words, twinning is discarded as a possible relaxation mechanism for the films presented here. An intermartensitic transformation to a bct phase is also unlikely. The only pathway that is favorable for the relaxation is the introduction of misfit dislocations, which were detected at a high density in the transition region. Hence, for the case of sputtered thin films, the relaxation mechanism is most probably misfit dislocations.

In addition, the obtained epitaxial growth thickness is related to the measured misfit at the buffer layer interface. For the case of higher misfits, the thickness of the epitaxially grown section of the film also decreases. Films exhibiting almost no misfits at the interface (0.5 % for Au the buffer layer) achieve complete epitaxial growth. In the particular case of the Rh buffer layer, an interdiffusion phenomenon is also observed.

The method of choice for obtaining functional thin films with higher thickness should not be the sputtering technique. Even when selecting the lowest possible sputtering rates, the achieved films do not exhibit an fct phase with high thickness. During this study, Prof. Mayer's group in Leipzig achieved fct films with high thickness grown on MgO substrates, using a molecular beam epitaxy method[60]. Some suggestions for changing the growth behavior of the film with sputtering are given in the outlook section.

Lorentz microscopy investigations were also performed in relaxed and epitaxial regions. The magnetic nature of the material changed in both regions, depending on the magnetocrystalline anisotropy. In the polycrystalline (relaxed) regions, the material showed high magnetic anisotropy, dominated by the magnetoelastic anisotropy component. The magnetocrystalline anisotropy component was very low, due to the polycrystalline nature of the investigated areas. For this reason, closure domain walls were detected, minimizing the stray fields. The epitaxial regions (unrelaxed) showed single crystalline behavior, since the magnetocrystalline anisotropy component dominated in these regions. No domain walls were recognized by Lorentz imaging.

A second research focus concentrated on the polycrystalline $Fe_{70}Pd_{30}$ layers sputtered on thermally oxidized Si substrates. In situ heating studies were carried out in order to understand the transformation kinetics of $Fe_{70}Pd_{30}$ FSMAs. In situ diffraction studies

accompanied by nanoprobe STEM-EDX measurements revealed an intermediate stage during bcc-fcc transformations. At temperatures up to 350 °C, no chemical and structural changes were observed. In the interval between 450 °C and 650 °C, bcc Fe precipitates were formed. From the obtained diffraction data, the composition of the matrix was determined to be $Fe_{65}Pd_{35}$. At temperatures over 750 °C, the desired fcc phase was achieved. The in situ Lorentz micrographs revealed the presence of closure domain walls in the film. The magnetization direction was again determined to be in-plane. The measured Curie temperature was much higher than was stated in the literature. The reason for this is possibly that the Fe precipitations occurred during heating.

The last part of the TEM examinations dealt with the Fe-Pd-Pt system. The possibility of forming complete ternary phases was investigated via in situ cooling experiments. A completely ternary region that exhibited fcc structure was found. The in situ cooling of the sample also demonstrated a successful fcc-fct transformation. Structural similarities between Ni-Mn-X type alloys were also noted, indicating structural modulations in the $Fe_{70}Pd_{30}$ system. The results are encouraging for obtaining functional Fe-Pd-Pt thin films.

PART II
Characterization of Caloric Thin Films

4.0 Caloric Effect

Recently, there has been increasing interest in alternative cooling systems that reduce the greenhouse gases used in refrigeration. The miniaturization of electronic technology also calls for local cooling devices that work more efficiently than do current fan/liquid based systems. One possible solution is the utilization of so-called caloric devices based on magnetic refrigeration (magnetocaloric effect), a phenomenon known since 1881[61]. Warburg et al. first described this effect on Fe, and showed that demagnetization can lead to the production of very low temperatures. However, these transitions are second order and are not feasible in today`s devices due their low efficiency[62] at room temperature.

External factors such as pressure, strain, magnetic fields, and electrical fields, can trigger first order transitions in some alloys that show discontinuous jumps of thermodynamic functions[63], which can lead to large temperature changes in the environment. Geschneidner et al. were the first to observe these extreme effects in gadolinium based alloys. This finding was a major breakthrough for cooling systems working at room temperature. However, the necessity of using rare earth metals, such as Gd limits the development of functional devices due to the high cost thereof. In 2002, Tegus et al. demonstrated a transition metal based refrigerant for room temperature applications[64] using MnFe(P, As) alloys. This has opened a new vista for using abundant and inexpensive materials for refrigeration.

The selection of the refrigeration type and the material determines the importance of the orientation of various anisotropic entities in the function. The entities of importance are the orientation of crystallographic variants in ferroelastic materials, the presence of magnetic domains in magnetic shape memory alloys, and the formation of polar domains in ferroelectric materials. These entities show a strong correlation with external stimuli, such as strain, magnetic fields, and electric fields, respectively. These external fields can also change the transition temperature. For example, in the case of ferromagnetic shape memory alloys, the application of a sufficient external magnetic field can result in a martensitic transformation. Similarly, the stress induction of a shape memory alloy gives rise to pseudoelasticity. In both cases, there is an entropy difference between the two states of the materials, before and after the transformation. The entropy difference between these two states (martensitic and austenitic) can be used to influence the temperature of a system. A schematic thermodynamic cycle is illustrated in Figure 51, which shows a case of magnetic refrigeration.

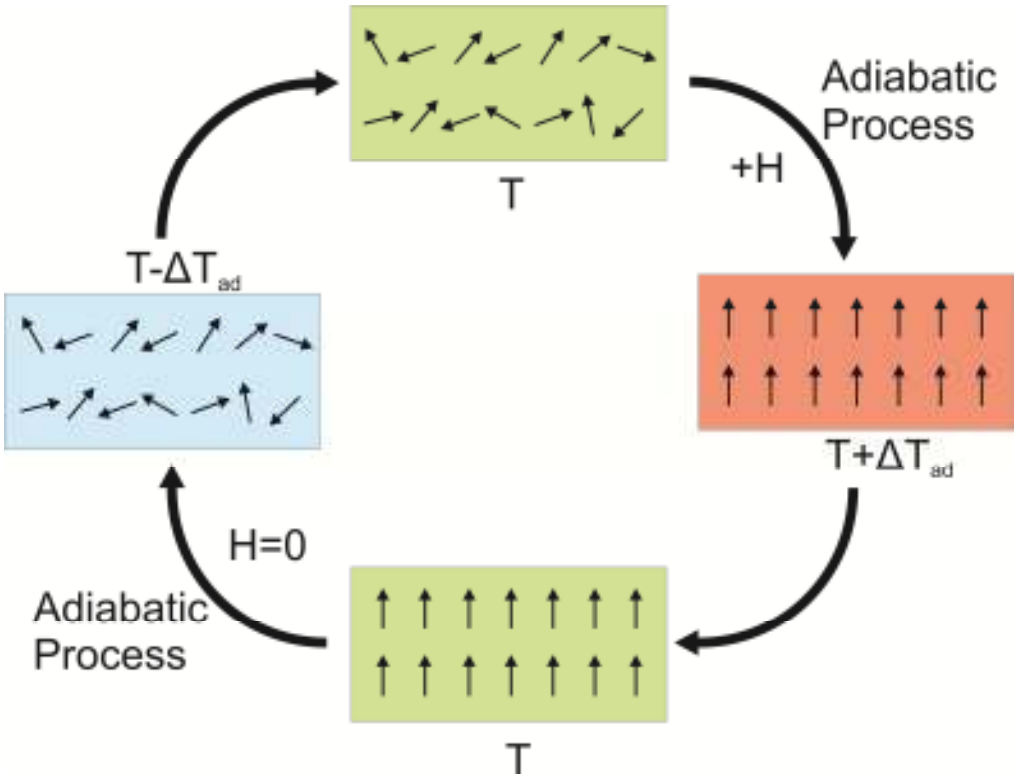

Figure 51: Schematic illustration of a refrigeration cycle. Exposing the magnetic sample in to a magnetic field causes the magnetic dipoles of the atoms to align preferentially, resulting in a decrease in the magnetic entropy. Isomagnetic enthalpy transfer occurs later, and the demagnetization process cools the material. See the text for more detail.

The cycle can be explained in four basic steps. A magnetic at ambient conditions (at temperature T) exhibits randomly oriented magnetic dipoles. Introducing this material into a magnetic field, H, causes the dipoles of the atoms to align parallel to the applied magnetic field. The result of this process is a decrease in the magnetic entropy. According to the necessity for the conservation of total entropy, the system responds to this magnetic entropy change by heating the material. In a well-designed system, this additional heat (ΔT_{ad}) can be transferred via a liquid or a gas. Thus, the material returns to temperature T and exhibits aligned dipoles in a magnetic field, H. Further decreasing the magnetic field leads to disorder of the magnetic dipoles; hence, the magnetic entropy increases. Again, the total entropy needs to be conserved and, as a result, the material cools. In a microsystem in which the material can be brought into contact with the environment being cooled, heat transfer occurs. Thus, the material returns to its initial state, and the cycle can start again. Similar cycles can be also envisaged in the case of elastocaloric (application of stress), barocaloric (application of pressure), and electrocaloric (application of an electric field) materials.

In this study, we focused on the TEM characterization of Ni-Mn-In-Co and Ni-Ti alloys, which both show a slight temperature change during cycling. Since the functional properties of these alloys are strongly interconnected with their micro/nano structures, TEM examination is of significant importance. Thin films were chosen because of their capacity for easy

integration into microsystem technology. Their high surface to volume ratio also makes them attractive, because of the fast heat transfer ability. Currently, neither of these thin film systems has been examined by TEM with regardto caloric effects.

In the case of Ni-Mn-In-Co thin films, the substrate-film interface is of significance. The interdiffusion of an adhesive layer to the film can hinder the function after the release of the film from the substrate. In addition, the composition-structure relationship has to be examined. The main question involves the kind of structure associated with a particular composition. For the determination of structure and composition, Tem is the only method available that has a high spatial resolution in one instrument. The possible presence of martensitic and austenitic regions with different structural motives also has to be evaluated. Since these structures are confined to small regions, TEM is the method of choice for the characterization.

Elastocaloric binary Ni-Ti films were investigated, with a particular focus on the precipitate-austenite interfaces. Note that the distribution of these particles directly affects the pseudoelastic behavior[65]. The microstructures of the films before and after mechanical cycling were also investigated. Some TEM methods, such as ACOM were performed on Ni-Ti films for the first time during these analyses. Similar examinations were repeated for the case of Ni-Ti-Cu films.

4.1 Ni-Mn-Ga Based Magnetocaloric Thin Films

The Ni–Mn–Ga, system, with Ni_2MnGa being the most intensively studied alloy, exhibits a complicated scenario of phase transformations. The giant magnetostrain is limited to the modulated martensites[66], while the FSM effect has not been reported for non-martensitic and non-modulated structures. At around 1073 K, the CsCl-type Ni_2MnGa[67] transforms into a Heusler-type structure[72]. On cooling, two thermally induced phase transitions are observed[68,69]: the Heusler-type structure is converted to a premartensitic phase below 260 K[71], followed by an MT below 220 K. The total shape change and the macroscopic strain energy are minimized by the formation of twinned martensite variants[70]. A number of martensitic structures have been examined,[71] and were found to have the common feature of a spontaneous lattice distortion of the parent Heusler-type structure. Depending on the composition of the Ni–Mn–Ga alloy and the temperature, the distorted structures can be described as having tetragonal, orthorhombic, or monoclinic[72] symmetry. Research on this system has been intense; nonetheless the martensitic structures and their influence on the magnetic field induced strain mechanism are still the subject of controversy.

The martensitic structures are defined by a simple shuffling of closely packed atomic layers; however, the structures are somewhat complicated by the details of modulation and disordering. Depending on the alloy composition[72], the structures are described by commensurate or incommensurate modulations. All known structure models are also affected by disordering, as indicated by averaging effects like mixed atom sites. The functional modulated structures most frequently consist of variants with five (5M), seven (7M), or an even higher number of distorted unit cells of the parent structure[73,74] (Figure 52).

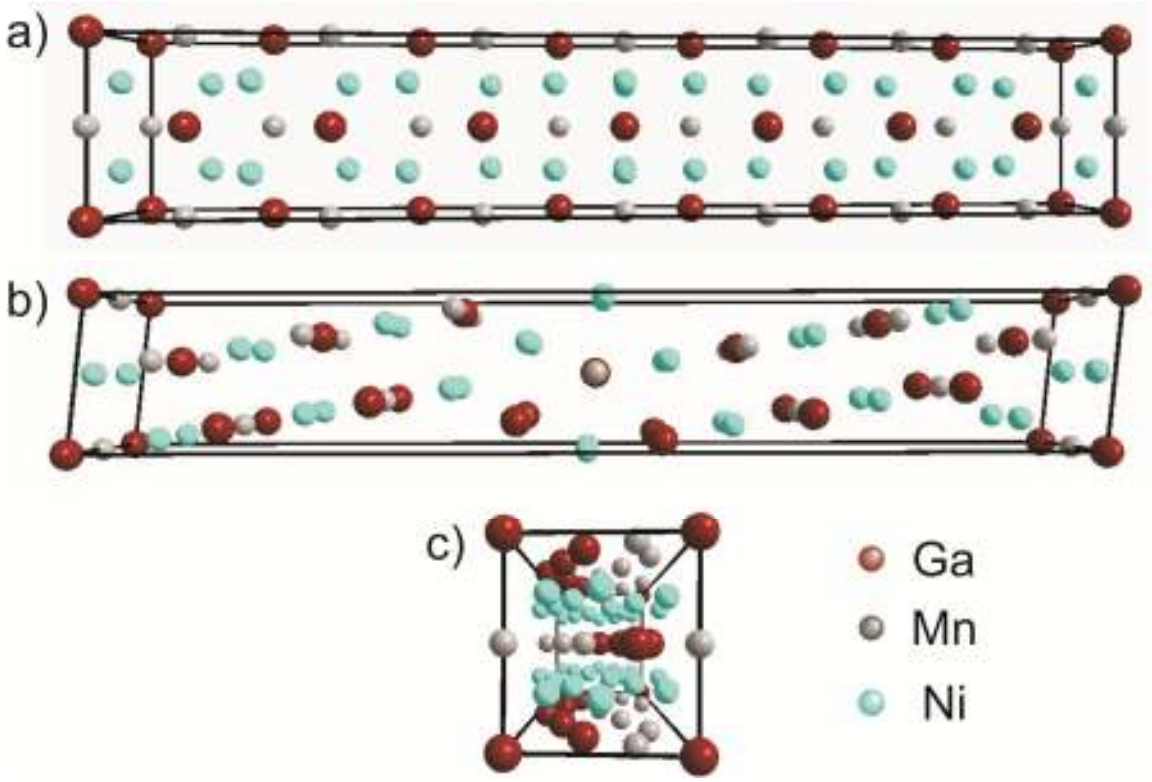

Figure 52: Structure of a 7M periodic approximant of an incommensurately modulated martensitic phase (composition of sample Ni_2MnGa) given in three main axes a), b) and c).

The number of layers within each lamella and the sequence of the lamellae are the two parameters that give rise to the formation of highly complex and diverse structures. Fähler et al.[75] also concluded that the 7M structure is an adaptive phase with a nanotwinned nature, which can attune internal and external stress by variations in the stacking sequences. Magnetic field induced stress is strongly dependent on the magnetization anisotropy and the mobility of twin boundaries[76]. Therefore not only is the crystal structure determination of fundamental importance, but so is the real structure characterization.

4.2 Magnetocaloric Ni-Mn-In-Co Thin Film

The following analysis investigated a film that exhibits magnetocaloric properties in the vicinity of room temperature. The TEM analyses were performed by Mrs. Viola Duppel at the Max-Planck-Institute for Solid State Research in Stuttgart.

Figure 53a depicts the bright field TEM image recorded on the cross-section of the Ni-Mn-In-Co thin film specimen. The thicknesses of the individual layers are determined as 300 nm for Ni-Mn-In-Co film, and 20 nm for the adhesion Cr layer. An additional Pt layer, originating from the cross sectional FIB preparation, is visible at the top of the image. Two different types of lamellar microstructures can be identified by the brighter and darker stripes in the diffraction contrast of Figure 53a. The enlarged section in Figure 53b shows angularly oriented lamellar structures that feature a modulation. The perpendicular stripes depicted in Figure 53d represent twinning of the martensite; the twinning plane is marked with a red arrow in the micrograph. Both characteristics are in good agreement with the SEM micrographs reported previously in the literature, and they correlate with the twinned microstructure of epitaxially grown Ni-Mn-Ga films. In addition, a bottle-like precipitation with a dark contrast is present, showing no indication of modulation (Figure 53c).

In the following study, three different subindexes are used in order to distinguish between possible structures. Subindexes 7M, A, and T stand for the modulated, austenite, and non-modulated tetragonal structures, respectively.

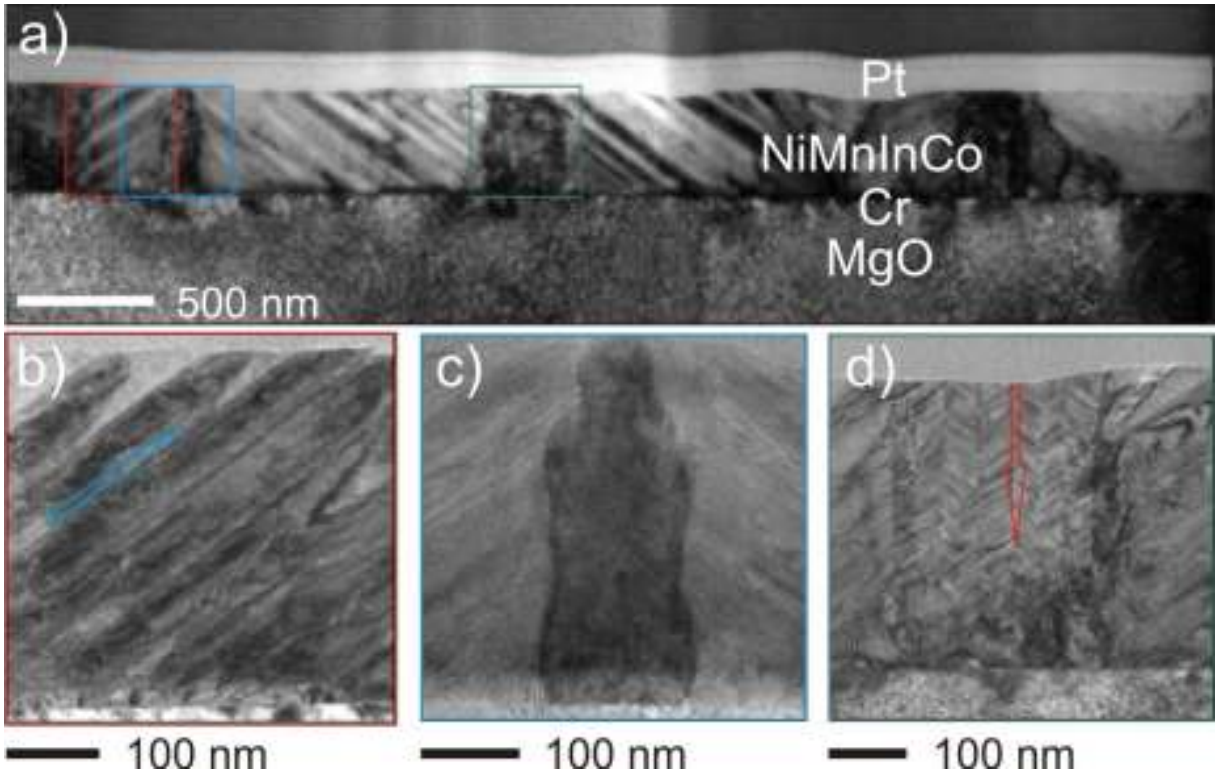

Figure 53: a) Cross sectional bright field TEM micrograph recorded at the MgO/Cr/NiMnInCo interface, b)-d) Magnified regions from a) showing different microstructures and twin boundary orientations. (The image was originally published in reference 77)

The obtained electron diffraction data give the orientation relationship between MgO and modulated Ni-Mn-In-Co as:

$$(001)[110]MgO \parallel (001)_A[110]_A$$

In addition to the microstructural differences, the regions can also be differentiated chemically according to their content of quaternary and penternary phases. The average chemical composition of the film in quaternary and penternary regions is calculated as:

Quaternary: $Ni_{49(0.25)}\ Mn_{37(0.31)}\ In_{12(0.17)}\ Co_{2(0.05)}$ (9 measurements)

Penternary: $Ni_{46}Mn_{33}In_8Co_9Cr_4$ (1 measurement)

The calculated chemical compositions show that the target composition is not maintained when the film is deposited at elevated temperatures. High resolution microscopy (vide infra) also proves that the quaternary regions can exhibit twin lamellae with non-modulated and modulated martensitic phases. In both cases, the orientation of the twin boundaries and the modulation propagation could be perpendicular or inclined by 45° with respect to the MgO substrate, respectively. Here, the structural features within the quaternary regions will be described first. Fig. 54a displays a bright field image recorded on a phase with an apparently

modulated structure. The twin boundaries running perpendicular to the substrate interface are also evident.

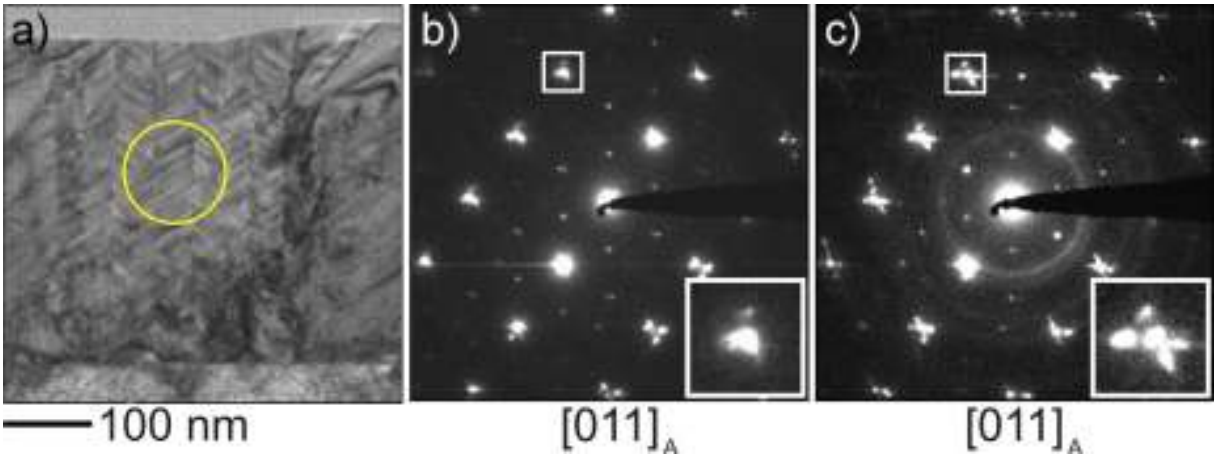

Figure 54: a) Bright field TEM image of a multiple twinned region, b) SAED, and c) PED patterns in $[011]_A$ zone axis orientation. The additional concentric ring on the PED pattern originates from the amorphous Pt layer. (The image was originally published in reference 77).

Both features are visible in the diffraction pattern depicted in Figure 54b, recorded along the $[011]_A$ zone axis orientation. The present modulation is remarkable for the diffuse intensities between the fundamental reflection, and the differently oriented grains are visible by the splitting of those fundamental reflections. The fundamental intensities show two intersecting and elongated streaks at the Bragg positions, produced by the combination of disordering and twinning. The orientations of the diffuse intensities show that the disordering originates from the imperfections in the periodicity of shuffled $(101)_A$ layers. The intensity and extension of the streaks is enhanced when switching to the precession electron diffraction mode, as shown in the corresponding enlarged sections. The diffuse rods running along $[101]^*_A$ in reciprocal space are tilted from the zone axis of $[011]_A$ by an angle of ca. 60°, and are incompletely cut by the Ewald sphere when applying SAED. Switching to the PED mode enables the excitation of the reflections from the higher order Laue zones; thus, wider sections of the diffuse rods are cut by the Ewald sphere. Two EDX nanoprobe point measurements show that the composition inside the region is $Ni_{50(0.875)}Mn_{36(0.615)}In_{12(0.085)}Co_{2(0.095)}$.

High resolution imaging is performed in order to investigate the twin interface. According to the literature, a misfit has to be introduced at the twin interface, since a modulation of the layers is present on both sides of the twin boundary[78]. Figure 55a depicts the average background subtracted HRTEM micrograph recorded along a twin boundary, taken from an area highlighted in Figure 54a. The twin boundary interface is parallel to $(11\text{-}2)_T$ planes. The modulation is also visible as the alternating faint bright-dark fringes on both sides. Across the twin boundary, interface regions with and without misfit are observed. The misfit of the

adjacent variants at the twin interface is apparent from the blurred contrast in Figure 55b. However, neighboring areas in which no alternating fringes are visible (i.e., non-modulated structures) show no indication of a misfit at the twin boundary. Note that the modulation is inclined through the image plane and should not be observed in the given zone axis, but is visible due to strain effects. This finding is in good agreement with the model proposed in the literature.

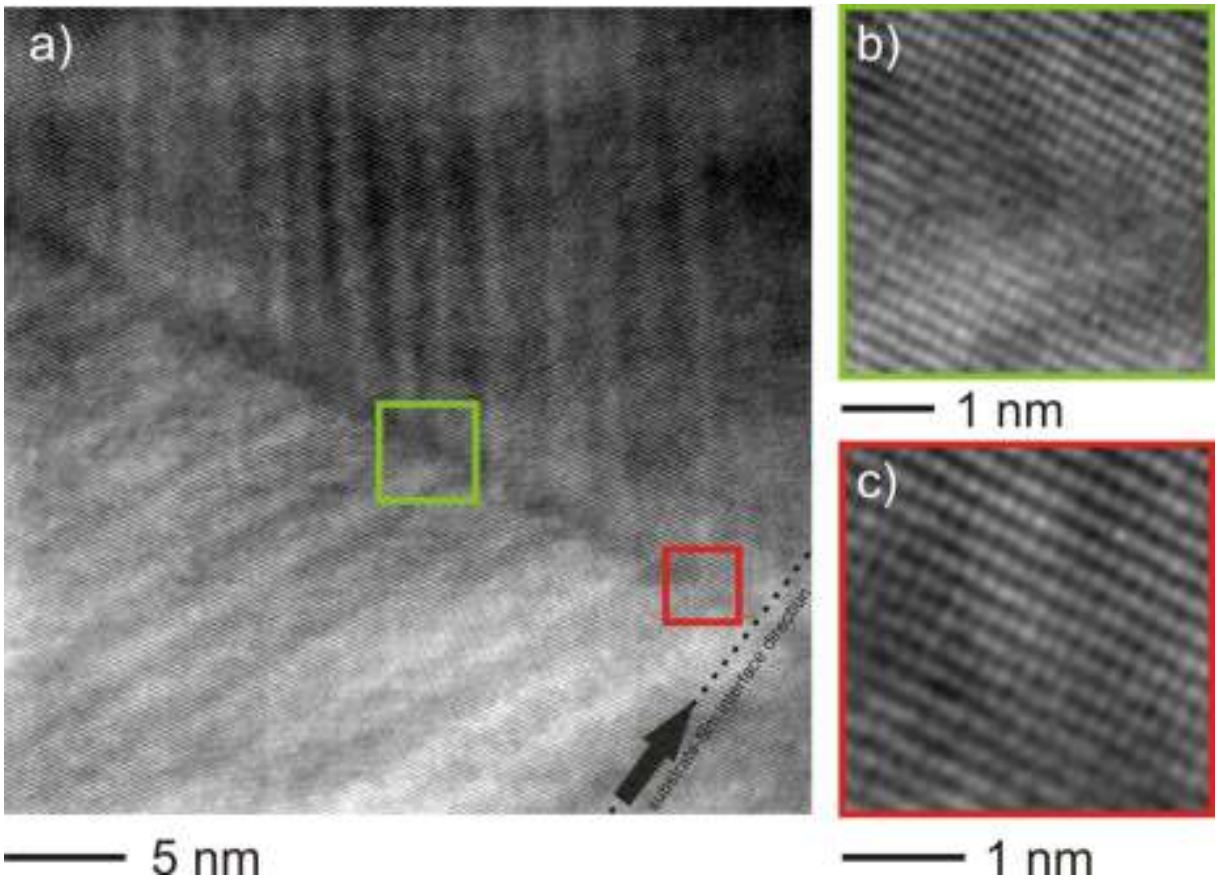

Figure 55: a) Average background subtracted HRTEM micrograph recorded along a twin interface taken from an area shown in Figure 54. a) showing the b) incoherent twin boundary interface at which the modulation occurs and c) the surrounding area with no indication of structural misfit and modulation.(zone axis: $[011]_A$) (The image was originally published in reference 77)

In addition to the twinned and modulated region, a non-twinned but modulated region is detected. Figure 56 depicts the bight-field micrograph and the HRTEM micrograph from a selected area. The SAED pattern is recorded inside the green squared region highlighted in the bright field TEM micrograph (zone axis: $[111]_T$) Five additional reflections between the fundamental reflections are evidence of the 6M modulation in the region. The cell parameters are determined as a_A = 5.44 A°, c = 7.10 A°, according to the austenitic settings. Although the 6M modulation is evident from the electron diffraction data, HRTEM micrographs recorded inside in the red square of Figure 56b show that the stacking also exhibits polytypic disordering. From the inserted intensity profiles, the thicknesses of the propagation lengths of

the modulated structures are calculated as 5M ~ 1.10 nm, and 6M ~ 1.30 nm. The numbers on the profile images specify the number of the shuffled $(010)_T$ layers. The profile on the left side of Figure 56b shows a periodic arrangement of peaks, as expected for an ordered 6M modulated structure. Since the SAED aperture represents an area of 100 nm on the specimen and the region is dominated by the 6M modulated structure, the polytypic intergrowth cannot easily be identified by Bragg scattering. Thus, the marginal width of the coherently scattering areas containing the same modulation-type is visible in the SAED pattern. An additional remark can be made regarding the intergrowth region separating the lamellas. The modulation is fading (cf. Figure 56b), potentially to avoid a large misfit strain. The presence of a non-modulated region between two differently modulated regions is suggested by the adaptive concept. EDX nanoprobe point measurements show a slight deviation from the aforementioned $(Ni_{50(0.875)}Mn_{36(0.615)}In_{12(0.085)}Co_{2(0.095)})$, namely $Ni_{48(0.07)}Mn_{37(0.55)}In_{13(0.195)}Co_{2(0.03)}$.

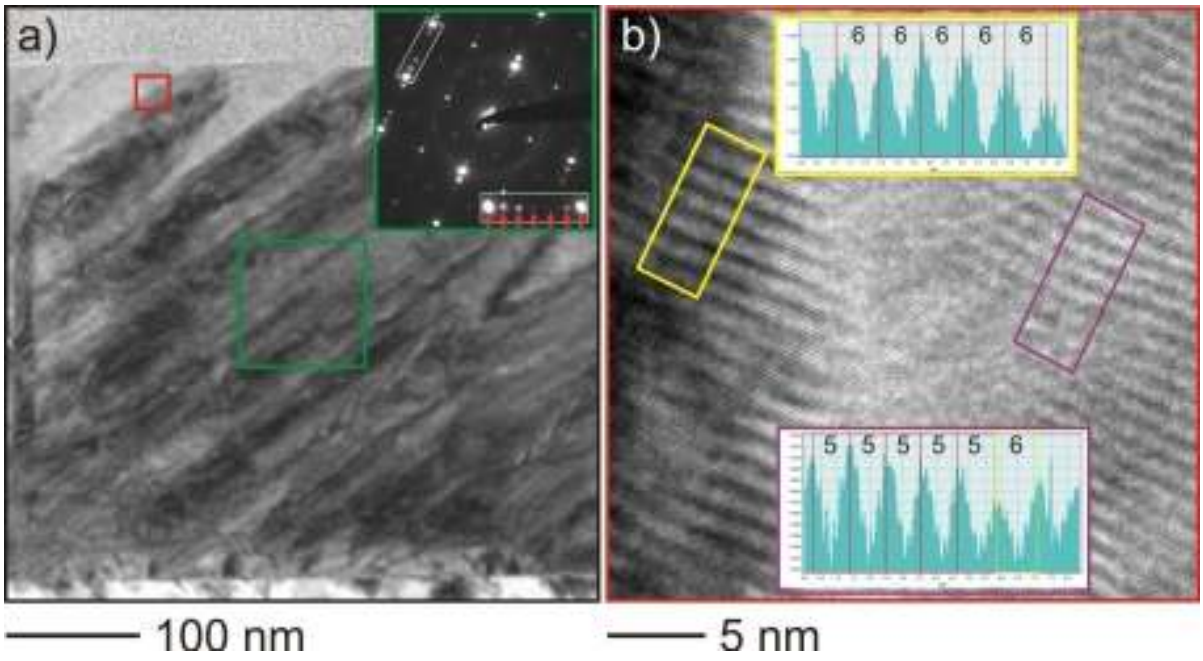

Figure 56: a) Bright field TEM image with inserted SAED pattern consistent with the 6M structure (top, right, with an inserted enlarged section). b) HRTEM micrograph recorded within the red square of a). Two inserted profiles from the marked areas in b) display a disordered array of layers with thicknesses according to 5M and 6M structures. All zone axis: $[111]_T$. (The image was originally published in reference 77).

Comparable behavior is observed for the regions displayed in the bright field image of Figure 57a. Similarly to the previous investigations, broad spots between the fundamental reflections are detected in the SAED pattern (Figure 57b, left, for zone axis $[201]_{7M}$). These six broad spots between the fundamental reflections indicate that the 7M modulated structure dominates in the depicted region. However, diffuse streaks indicate the presence of an additional disordering. The intensity profile calculated from the high resolution imaging shows this additional disorder, namely the various lamellar intergrowths (inset in Figure 57c). Again,

the numbers written on the profile plot specify the number of the shuffled $(010)_T$ layers, consisting of the layers establishing the 6M, 7M, and 8M structures. As in the previous results, the experimentally determined distances of consecutive peaks are ca. 1.30 nm, 1.50 nm, and 1.70 nm, as expected for the layers of 6M, 7M, and 8M structures, respectively. The SAED pattern matches very well with the simulations calculated from the 7M model,[79] as depicted in Figure 57b. Several satellite reflections are strongly excited in the experimental pattern; however, these reflections are not kinematically forbidden, but are very weak in intensity according to the simulated pattern. A rationalization for this discrepancy is based on multiple scattering effects, which are most prominent for reflections occurring adjacent to high-intensity peaks. Quantitative EDX point measurement shows that the composition is $Ni_{50}Mn_{35}In_{13}Co_2$.

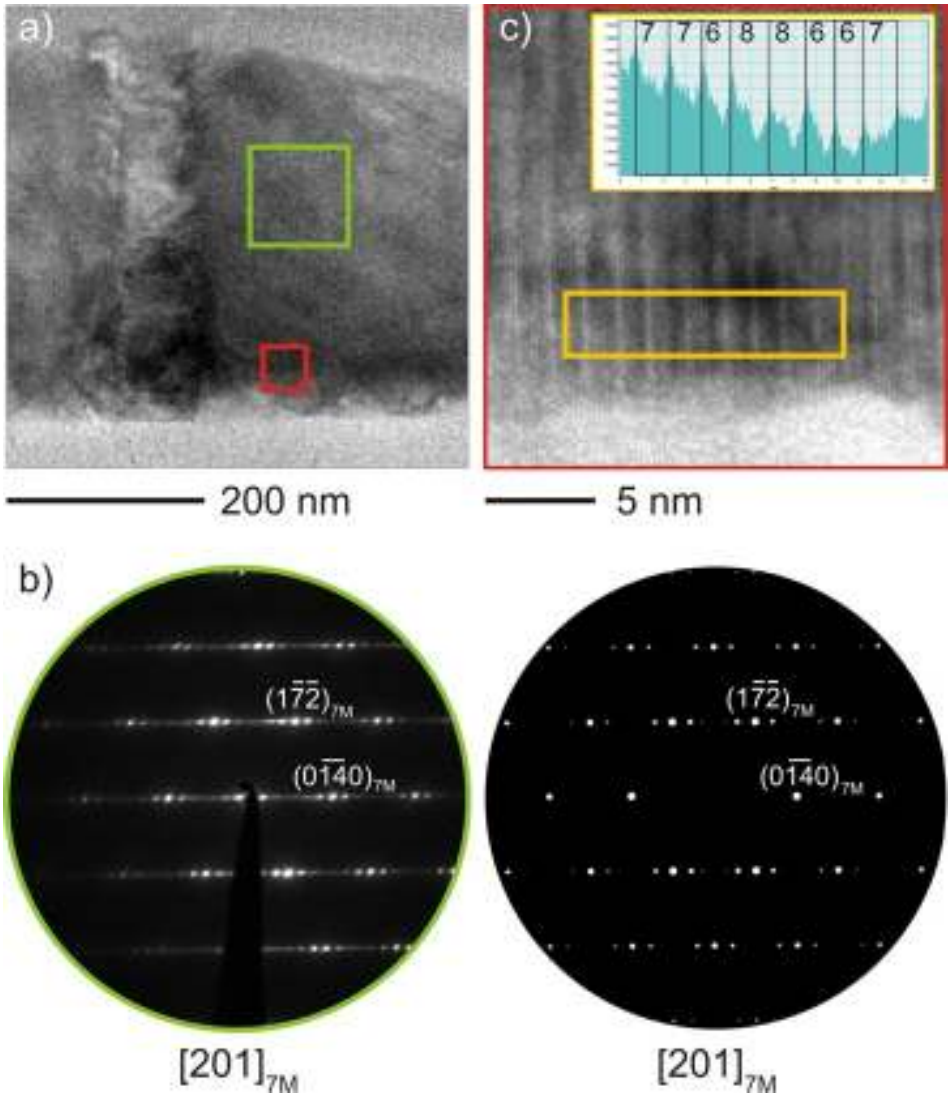

Figure 57: a) Bright field micrograph recorded on a modulated region, b) SAED (left) and simulated diffraction pattern (right) showing six broad spots between the fundamental reflections, indicating that the dominant structure is 7M. c) HRTEM micrograph recorded inside the red highlighted area in a). Inserted profile from the marked area in c) shows layered disordering of 6M, 7M, and 8M structural motifs. All zone axis: $[201]_{7M}$ (The image was originally published in reference 77).

Figure 58 depicts a bright field TEM image recorded on a non-modulated twinned region. Large martensitic variants (tetragonally distorted regions with a width of around 50 nm) with different orientation give rise to the formation of alternating dark and bright stripes in the bright field image. A different orientation of the domains is also visible via FFT analysis. The calculated FFT patterns from the square sections of the HRTEM micrograph presented in Figure 58b show the presence of similar structures, although these are mirrored at the $(11\text{-}2)_T$ planes. The cell parameters are determined as a_A = 5.23 A° and c = 6.77 A°. The FFT pattern of the entire HRTEM micrograph with involvements from both domains is consistent with the PED pattern shown in Figure 58c (All zone axis: $[201]_T$). In contrast to the previously observed region, no diffuse scattering is recognized in the PED pattern, thus no shuffling of the $(010)_T$ layers can be identified. The chemical composition is determined to be $Ni_{48(0.275)}Mn_{38(0.215)}In_{12(0.43)}Co_{2(0.06)}$ in this region.

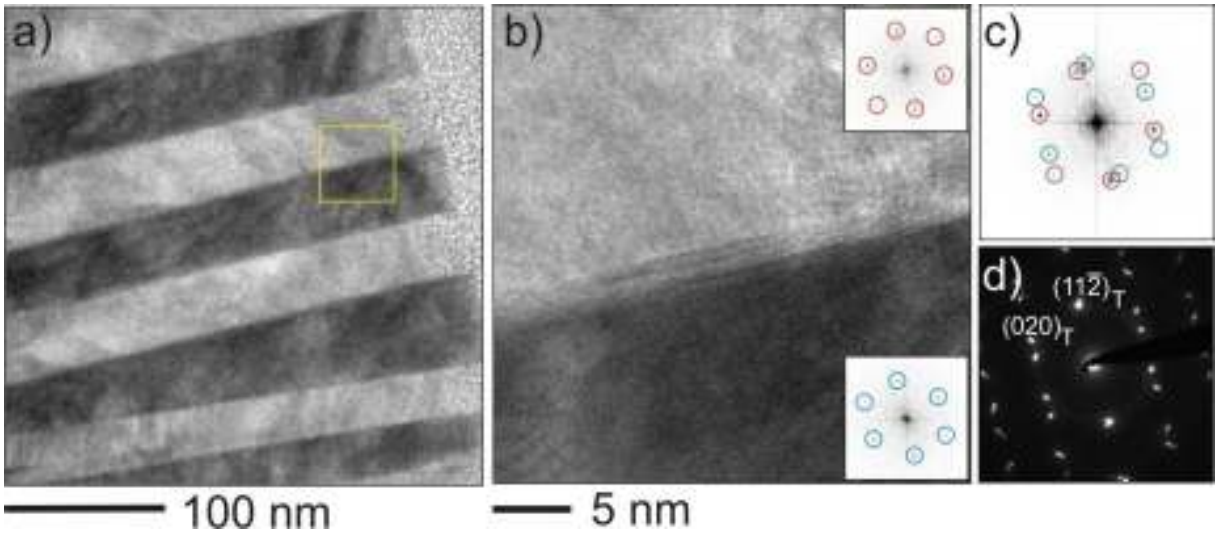

Figure 58: Non-modulated twinned structure. a) Bright field TEM image with stripes originating from diffraction contrast by twinning, b) HRTEM micrograph from the region marked in a) with FFTs calculated inside the adjacent lamellae, c) FFT of complete b) displaying a superposition pattern, and d) PED superposition pattern from a larger twinned area. All zone axis: $[201]_T$ (The image was originally published in reference 77).

In addition to the quaternary regions discussed previously, penternary areas were also identified next to the Cr adhesion layer; for example, the irregularly shaped precipitate with an average width of ca. 100 nm shown in Figure 53a (left, and in the enlarged section). Figure 59 summarizes the structural and chemical nature of the investigated area. The spatial distribution of all relevant elements identified by nanoprobe analysis is presented by the EDX elemental maps in Figure 59a. The SAED patterns recorded inside the precipitate and the Fourier analyses of the HRTEM micrographs indicate no satellite intensities, thus revealing a non-modulated tetragonal structure (zone axis $[201]_T$, [80]). Furthermore, the microstructure is twinned at $(11\text{-}2)_T$ planes(construction of the superposition pattern in Figure 59c). The experimental and the constructed patterns show a well-defined systematic for the splitting of the reflections in terms of twinning via reticular merohedry[81]. At a c_T/a_A ratio of

1.40 (a_A = 5.09 A°; c_T = 7.11 A°), the reflections within every third row parallel to $[-1-12]_T$* coincide exactly, while the density of reflections in the neighboring rows is doubled with constant reciprocal distances between the reflections. This finding is in good agreement with the simulated diffraction pattern shown in Figure 59c, as well as with the measured $(c/a)_T$ ratio. Applying the conversion $a_A = \sqrt{2}\, a_T$ to the measured a_T parameter and calculating the c/a_T ratio again, the c-axis is twice as large as is the a-axis $(c/a)_T$= 1.98). Thus, the face-centered sub-cell is pseudocubic in the tetragonal cell settings. The volume of the unit cells remains almost constant when two non-modulated twinned regions are compared (the regions represented in Figure 58a with volume (V_1), and in Figure 59a with volume (V_2)), although they have different c/a ratios, namely 1.29 and 1.40, respectively. Hence, the volume is conserved by the tetragonal distortion of the unit cell (V_1 = 185.2 A^3, V_2 = 184.2 A^3), which is the nature of diffusionless transformations. Note the absence of diffuse streaks along $[-1-12]_T$, indicating the absence of a polysynthetic twinning. Interestingly, the elemental map of the Cr adhesion layer matches very well with the In-poor/Co-rich region, while the PED pattern taken inside the precipitate reveals no sign of structural inhomogeneity in terms of an additional Cr phase. Thus, Cr from the adhesion layer diffuses into the Ni-Mn-In-Co thin film.

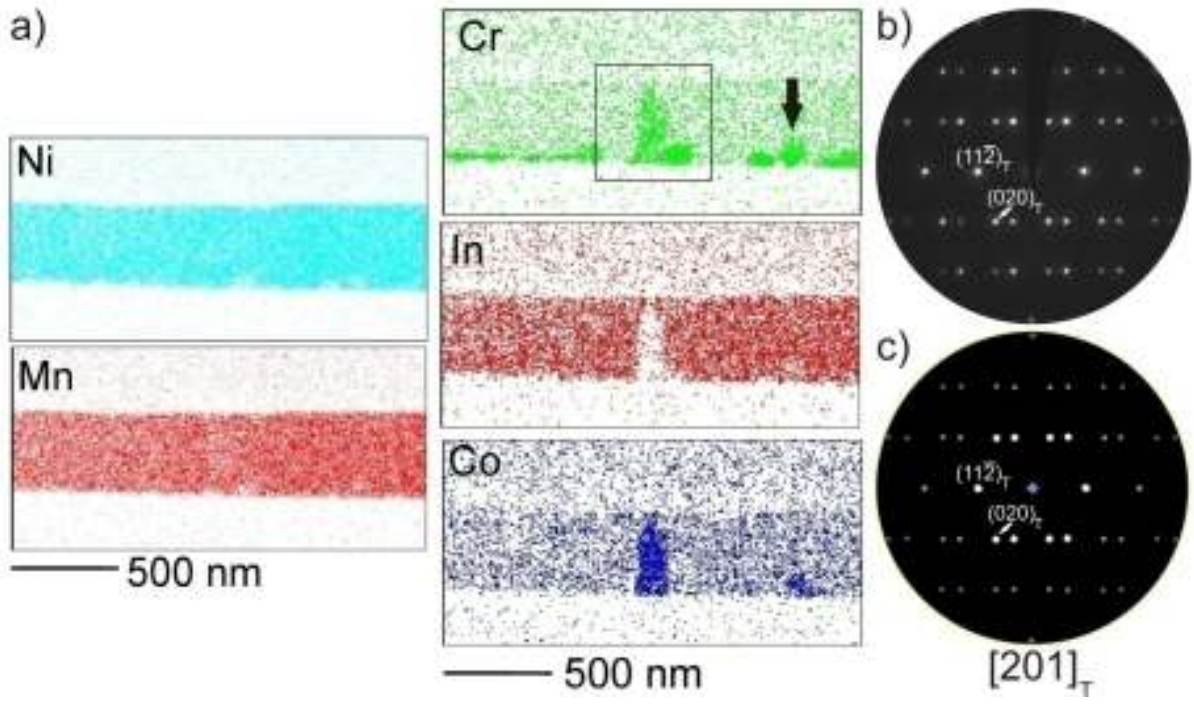

Figure 59: a) EDX elemental maps. The composition within the Co-poor region is $Ni_{49}Mn_{37}In_{12}Co_2$ b) SAED pattern recorded at Co-rich and Cr containing area (marked in a)) showing a disordered and twinned structure (zone axis $[201]_T$) with the composition $Ni_{46}Mn_{33}In_8Co_9Cr_4$ and corresponding electron diffraction simulation (c).(The image was originally published in reference 77).

The chemical composition is calculated to be $Ni_{46}Mn_{33}In_8Co_9Cr_4$ inside the precipitate, and $Ni_{48(0.07)}Mn_{37(0.55)}In_{13(0.195)}Co_{2(0.03)}$ in the neighboring region. This finding can be rationalized by

the substitution of In by Co and Cr, respectively. Note that the alloy remains Mn rich in comparison to the Ni_2-Mn-X stoichiometric composition, even in areas with interdiffusion.

Additional imperfections in the Cr adhesion layer are observed (right side of Cr elemental map, see arrow). These might play an important role in the removal of the Ni-Mn-In-Co film from the substrate, and might hinder the twin boundary motion.

4.3 Ni-Ti Shape Memory Alloys and Their Potential for Elastocaloric Devices

Ni-Ti-based SMAs have attracted significant attention as functional materials for industrial and medical applications, due to their remarkable shape memory effect (SME), pseudoelasticity, corrosion resistance, and biocompatibility[82,83,84]. Many investigations have focused on the SME and pseudoelasticity aspects, which are fundamentally associated with the reversible thermoelastic martensitic transformation. Since the martensitic transformation is explained by a transition from a highly symmetric cubic (austenite) to a low symmetric (martensite) phase without a diffusionless, isothermal change of enthalpy or a related adiabatic change of temperature, it can also be envisaged for those materials when a mechanical stress is applied or released (the so-called elastocaloric effect[85]). In the following section, the common phases that occur in the Ni-Ti system are briefly summarized, and the desired microstructure for the best cooling efficiency is subsequently discussed.

- **Austenite:** The high temperature austenite phase has an ordered B2 ($CsC^{86}l$ type) structure with a lattice constant of a = 0.3015 nm at room temperature[87].

- **Martensite:** Three types of martensites can be formed during the transformation, depending on the composition and thermal treatment of the alloy.

  **B 19`:** In fully annealed binary Ni-Ti alloys, direct transformation from B2 to B19` martensite phase is mostly observed[88]. The crystal structure of B19` is accepted to be monoclinic and crystallizes in space group $P2_1/m$[89,90,91].

  R- Phase: The so-called R-phase occurs between the transformation from B2 austenite to the B19´ martensite[37], and was first observed in electron diffraction studies by Hwang[92]. It is characterized by the superlattice reflections occurring in 1/3 position along <110>* and <111>* directions of B2 phase. Frick et al recently determined the space group of the R-Phase to be P3.

B19: A third type of martensite detected in Ni-Ti based alloys is called the B19 phase. It is observed mostly in Ni-Ti-Cu alloys where the Cu content is larger than 10%[93]. The structure of B19 martensite is orthorhombic with the space group Pmmb[94].

In binary Ti-Ni alloys with nickel exceeding 50.5 at%, the parent phase demixes by slow cooling or by aging at lower temperatures after quenching from high temperatures. The demixing products exhibit two metastable phases, Ni_3Ti_2, Ni_4Ti_3 and the stable Ni_3Ti phase.

- **Ni_3Ti_2:** Above 373 K, the high temperature phase is reported having a tetragonal structure (I4/mmm), while below this temperature, a low temperature phase occurs, exhibiting an orthorhombic structure with the space group Bbmm[95,96].

- **Ni_4Ti_3:** The Ni_4Ti_3 phase forms homogeneously in the early stages of aging at low temperatures, coherent with the matrix, as fine platelets[97]. The Ni_4Ti_3 phase Ti_3Ni_4 precipitates are characterized by the superstructure reflections located at the 1/7 position along <123>* reciprocal vectors of B2 type austenite in electron diffraction patterns.
  The size, morphology, and configuration of Ni_4Ti_3 precipitates in a bulk single-crystal of Ni–Ti alloy have been investigated by Schryvers and Eggeler et al. via two-dimensional transmission electron microscopy-based image analysis and 3D reconstruction from slice-and-view images obtained using focused ion beam/scanning electron microscopy. The Ni_4Ti_3 precipitates form 0.54 µm pockets of type B2 along the compression direction, and 1 µm perpendicular to the compression direction[98].

- **Ni_3Ti:** The stable Ni_3Ti phase has a hexagonal structure with an ordering of DO_{24} type[99].

Crystal structures of the important phases, characterized in the framework of this study, are presented in Figure 60 in order to give an overview thereof.

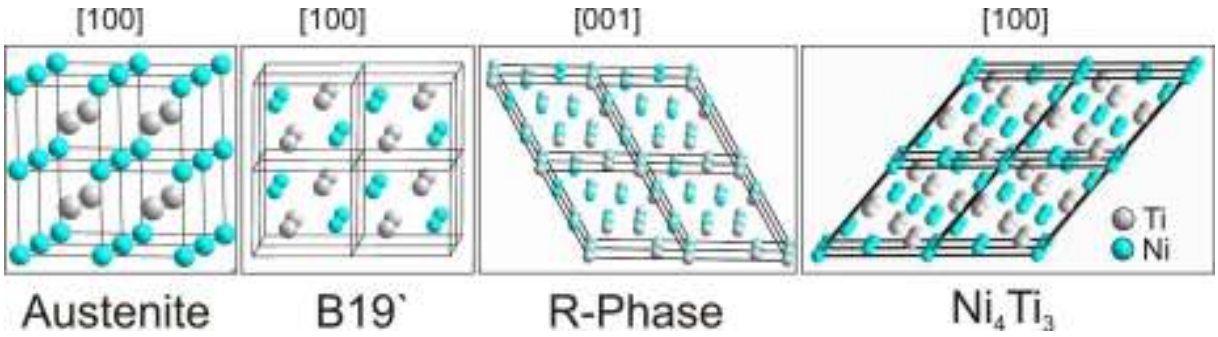

Figure 60: Crystal Structures of the prominent phases occurring in binary Ni-Ti system. Projections are given in close to [100] direction of the B2 austenite, B 19` martensite, Ni_4Ti_3 precipitate and in [001] direction for the R-Phase.

Efficient Cooling:

For the most efficient elastocaloric response, a complete transformation from austenite to martensite is necessary, since the maximum entropy change can be achieved in this way. The residual martensite or austenite will decrease the amount of ΔE (entropy), which reduces the cooling efficiency. Therefore, the volume fraction of untransformed retained martensite during cycling must be minimized, so that a large fraction of the material can transform repeatedly. Dislocations are known to hinder the reverse martensitic transformation, and are therefore a reason for untransformed retained martensite and remanent strains. Grain size also plays a role in the formation of untransformed retained martensite, since grain boundaries favor the martensitic transformation but obstruct retransformation[100].

A crucial topic of fundamental importance for elastocaloric cooling is the fatigue behavior of Ni-Ti based thin films, where repetitive temperature- or stress-induced martensitic transformations could provide an infinite lifetime[101]. Various investigations into fatigue behavior of bulk Ni-Ti is available in the literature, but studies on fatigue in thin films are lacking. Since the fatigue is decisively determined by microstructural and crystallographic factors (grain size, size, amount, distribution, and orientation of precipitates, film texture and, in relation to this, the direction of mechanical loading), these aspects need to be related to their influence on fatigue mechanisms in thin films. Grain size and precipitates can be adjusted by thermal annealing parameters; such as, the time-temperature profile and the applied mechanical stress. Eggeler et al. reported that the fatigue life is decreased in the event of complete austenite/martensite transformation[102]. Thermal and mechanical cycling processes create plasticity, which may be due to the effects of a moving martensite interface[103]. The accumulation of the dislocations modifies transformational behavior, resulting in changes in transformation temperatures, strain, and stress. In the case of thermal cycling/fatigue, extensive TEM studies have been carried out depending on the microstructural changes[104,105,106,107,108,109]. Pelton et al. showed that the dislocation density increases with the thermal cycling (after 100 cycles)[101] which is consistent with the in situ observations byMiyazaki et al.[110].

The TEM microstructure investigations on mechanically fatigued pseudoelastic slightly Ni-rich binary alloys showed that, after 10 cycles, the microstructure consisted of banded austenite with a high density of dislocations with <100>/{011} slip systems interspersed with retained deformed martensite[111]. These austenitic grains contain dislocations and subgrains with no apparent retained martensite, similar to the non-fatigued microstructures. It was accepted by all the authors that cyclic transformations between austenite and martensite are

more complicated than those predicted by continuum of crystallographic theories, and these behaviors have to be taken into consideration, particularly for the case of thin films.

Ternary Alloys:

The addition of a third element reveals even more possibilities for adapting binary NiTi thin films towards the more specific needs of applications. Although much work has been carried out on ternary bulk materials, systematic research on thin film materials using TEM is limited. One of the ternary thin film systems studied more frequently is Ni-Ti-Cu. The Cu content in Ti-Ni-Cu thin films has a significant effect on the martensitic transformation sequence. Ni-Ti-Cu films with a Cu content of <7.5 at% show a single-stage transformation from the B2 parent phase to the B19´ martensite phase, whereas Ni-Ti-Cu films with a Cu content in the range 7.5–9.5 at% show a two-stage transformation of B2 → B19 → B19´[104]. When the Cu content exceeds 10 at%, only the transformation from B2 to B19 takes place in Ni-Ti-Cu films[112]. When the Cu content is more than 10 at%, the Ni-Ti-Cu bulk alloys become brittle, and their workability deteriorates significantly[113]. A disadvantage of most Ni-Ti-Cu alloys is that the transformation temperatures do not decrease below room temperature. Alloys that are pseudoelastic at room temperature, but which have small hysteresis, can be obtained by alloying Cr or Fe.

a) Binary Ni-Ti Thin Films:

Two examples of binary sputtered films were investigated. A continuous deformation (a phase change from austenite to martensite) is needed for efficient cooling; thus two extreme cases were taken into account: an annealed sputtered film, and a similar sample that was subsequently mechanically cycled. The microstructural changes were investigated by TEM. The uncycled film was expected to be an austenic matrix with inside precipitations. The cycled film was expected to be a residual martensite, or a deformed austenite.

Figure 61a shows an overview image of the uncycled sample. The experimental and simulated SAED patterns recorded at the same region are given in Figures 61b and c, respectively. Fine, elliptical precipitates are visible inside the bright field image (the area marked in yellow in Figure 61a). The length of these precipitates varied from 30–75 nm.

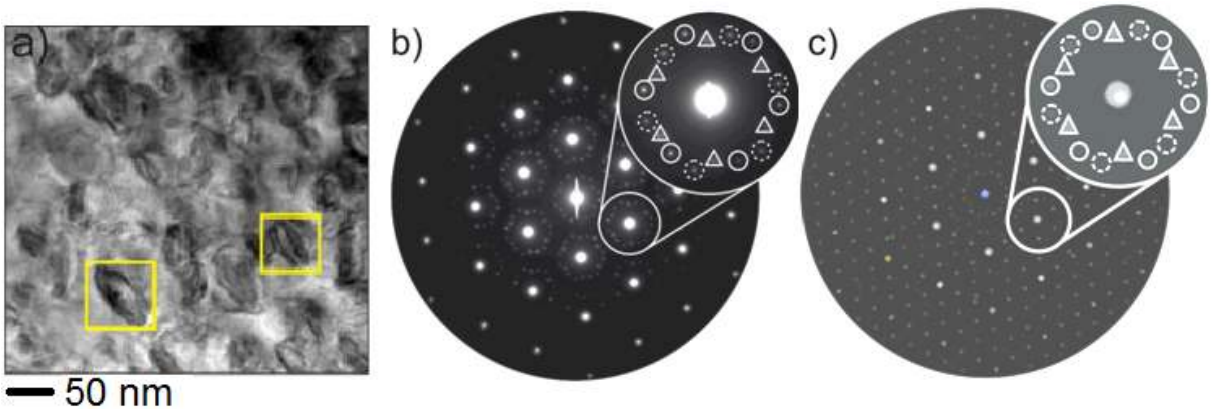

Figure 61: a) Bright field image of the uncycled sample, b) SAED pattern recorded at this region and c) simulated electron diffraction pattern. The reflections originating from the R-phase and Ni_4Ti_3 precipitates are marked with open triangles and circles, respectively.

The SAED pattern shown in Figure 61b indicates that three different phases are present in this region: austenite (B2), Ni_4Ti_3 precipitate, and the R-Phase. The zone axis of the SAED pattern is [111] with respect to the B2 phase. The Ti_3Ni_4 precipitates are distinguished from the superstructure reflections located at the 1/7 position along the <123>* reciprocal direction of the B2 type austenite, and are marked with open circles on the experimental pattern. The measured d-values are consistent with the data in the existing literature. These precipitates are twinned at the (1-21) interfaces. An R-phase can also be identified according to the characteristic superlattice reflections, occurring this time in the 1/3 position along the <110>*and <111>*directions of the B2 phase. The reflections originating from the R-phase are marked with open triangles in the enlarged section of Figure 61b. The simulated electron diffraction pattern is in good agreement with the experimental data (Figure 61c).

Further investigating of the specimen using SAED gave no indication of either a B19 or a B19` martensite phase. These results are encouraging from the caloric perspective, because a complete transformation from austenite to martensite is required for the most efficient cooling. Hence, no loss of entropy change should occur due to the presence of residual martensite. A microstructure for the complete martensite/austenite transformation without any loss is provided.

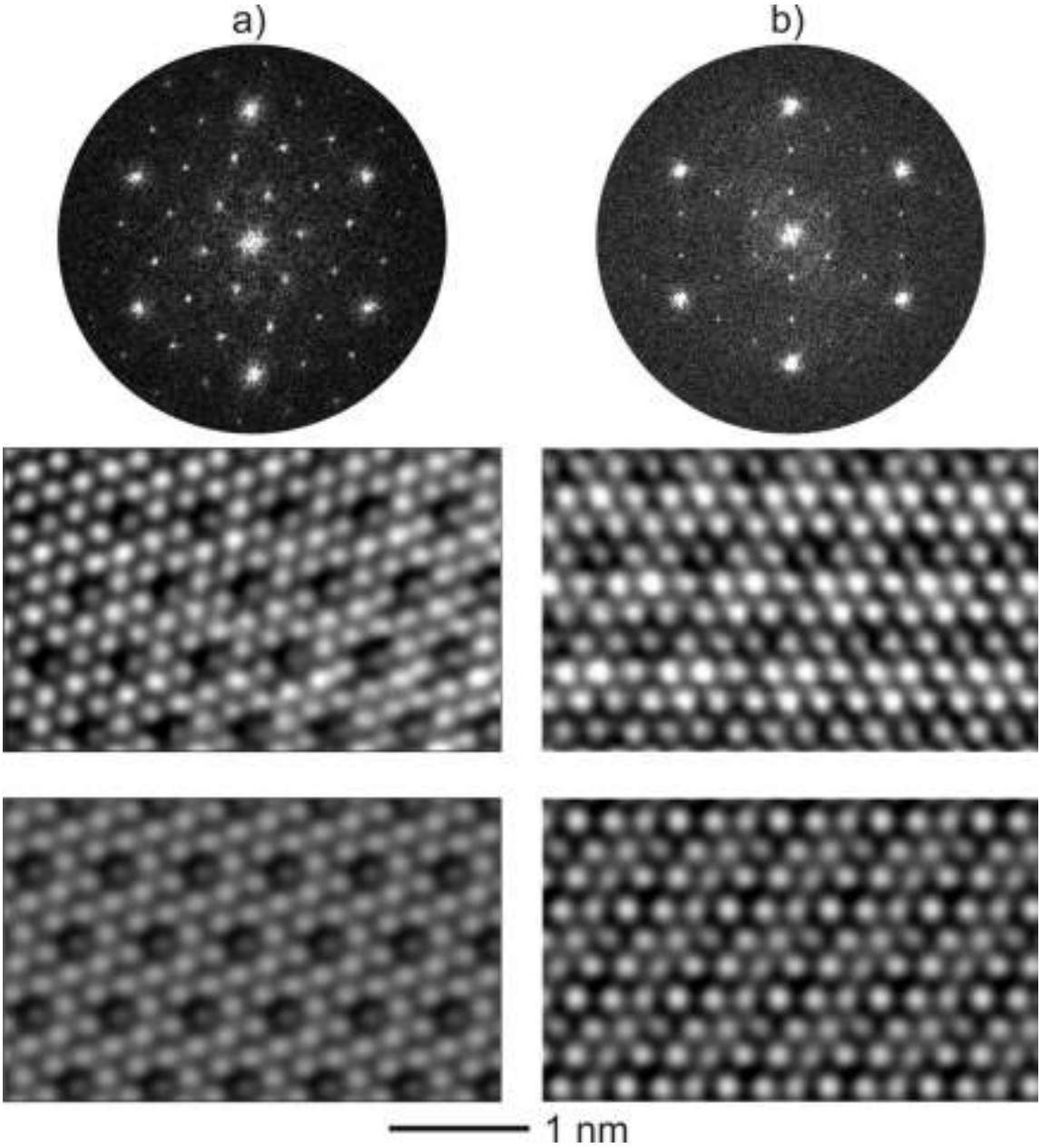

Figure 62: Column a) Top: Fourier transform calculated from a square selected area of a HRTEM micrograph, Center: experimental HRTEM micrograph, bottom: simulation (zone axis $[111]_{B2}$, Δf = 0 nm, t = 2.3 nm) for a precipitate of Ti_3Ni_4. Column b) Top: Fourier transform calculated from an HRTEM micrograph, s.o., Center: experimental HRTEM micrograph, bottom: simulation (zone axis [001], Δf = -75 nm, t = 10.7 nm) for a precipitate of the R-phase (The images were recorded by V. Duppel and L. Kienle in MPI-FKF, Stuttgart).

Figure 62 depicts the experimental and simulated HRTEM micrographs with calculated FFT patterns of Ni_4Ti_3 precipitate (a) and R-phase (b) observed in the uncycled Ni-Ti sample. Both experimental micrographs are in good agreement with the simulated ones. Again, the zone axes of the images are parallel to the [111] direction with respect to the B2 austenite. Although similar results have been reported in the literature, images of this quality, have to the best of our knowledge, not yet been produced.

The PED technique was also applied to the film in order to reduce the multiple scattering effects and to enhance kinematical diffraction. Note that the binary Ni-Ti samples are not fully adequate for PED investigations, since the reflections arising from the R-Phase are dynamically enhanced, and vanish when PED is used. On the other hand, one can clearly identify which reflections originate from dynamically scattering effects and which do not. This distinction is of fundamental importance for the interpretation of electron diffraction patterns that include structural disorder.

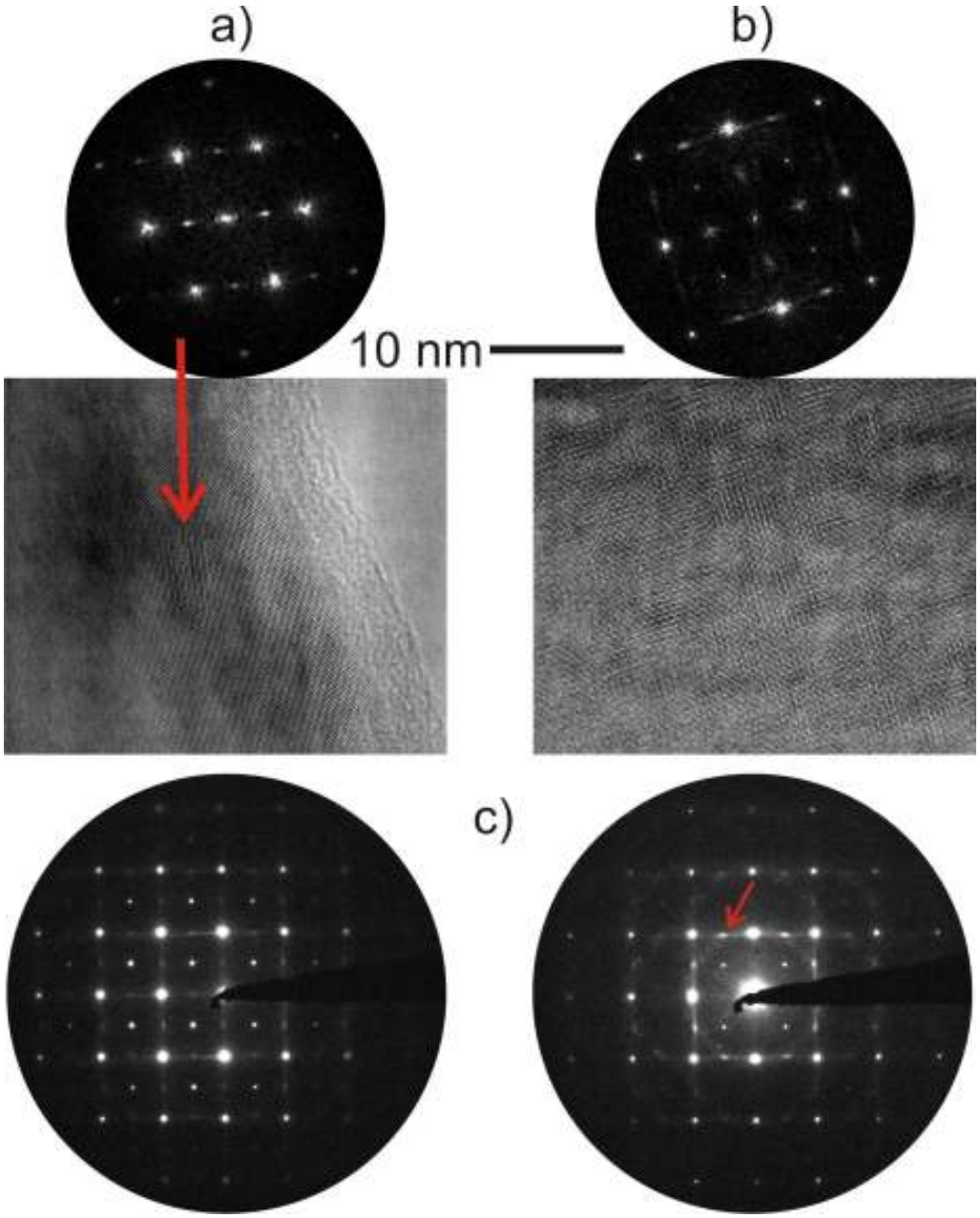

Figure 63: a) and b) are the HRTEM micrographs recorded on tweed-like microstructures, and corresponding FFT patterns recorded on two different zone axes. c) SAED and PED patterns show concentric spots located at ½ <110> positions. The application of PED makes those reflections more distinct.

Figure 63 displays the HRTEM micrograph recorded on the so-called tweed-like structure in the uncycled film. This contrast typically consists of irregular lines forming a kind of cross-hatched pattern. This microstructure is known as the premartensitic phase, and occurs due to the distortion of the austenitic lattice. Numerous systems show these tweed microstructures, and a variety of origins exist for the shear distortions, which are one of the two basic conditions that must be satisfied for this type of contrast to develop.

The conditions are:

1. A source of finely distributed centers of asymmetric strain.
2. An elastically anisotropic matrix phase.

Both conditions are fulfilled for the case of the binary Ni-Ti film. Since the film is annealed and cooled down to the room temperature, precipitates and an R-phase are formed, which serve as the anisotropic matrix and strain centers.

The weak reflections (marked with an arrow in the SAED pattern) are more strongly excited when applying PED. Hence, the intensities arising from this tweed structure exhibit a three-dimensional form, and are more strongly excited via nearly kinematical electron diffraction. This finding is in contradiction to the findings of Somsen et al, who applied tilting experiments in the SAED mode and assumed that these reflections were excited via double diffraction, since they vanished upon tilting. Our results show that tilting and rotating the primary beam by around 3° increases the relative intensity of the reflections on the ½ <100>* positions of the austenite lattice. The diffuse scattering is also enhanced via PED.

These results are also complemented by automated texture measurements (ACOM). This techniques allows the generation of orientation mappings of crystalline materials by collecting locally diffraction patterns, similarly to the EBSD (electron back scattering diffraction) technique. One of the main problems encountered when investigating the Ni-Ti alloys via electron microscopy is obtaining crystallographic information on a large scale. Of course, high resolution imaging and diffraction techniques provide sufficient information for phase identification; however, this is always restricted by the aperture size, or only works at high magnification. Local diffraction techniques, like convergent beam electron diffraction are also very effective approaches, but they are time consuming and the interpretation of the obtained patterns is not straightforward because the images depend heavily on the thickness and on the beam (convergent angle). Here, a new approach is presented. As previously explained in the methodology, a convergent beam is selected for the investigations in this technique. A calibrated external camera, mounted above the fluorescent screen recorded the local

diffraction patterns when the beam scanned the region of interest in STEM mode. The obtained patterns were then compared with the database.

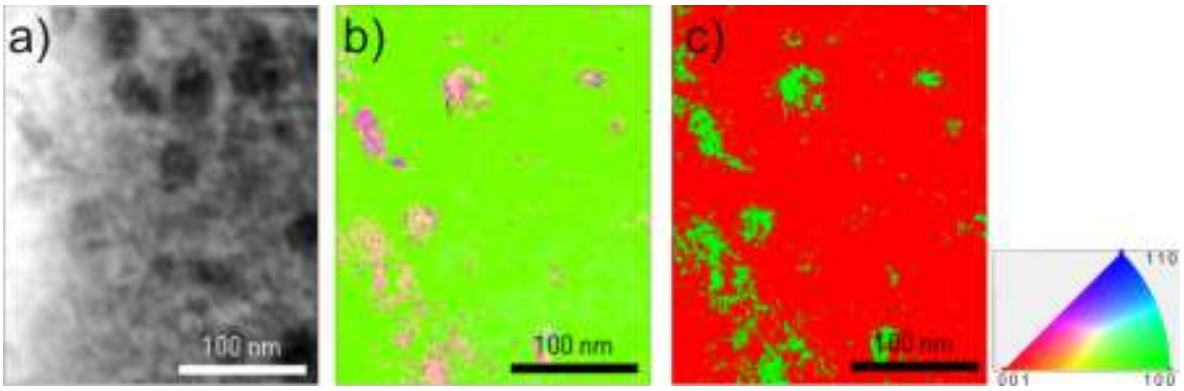

Figure 64: Automated orientation and phase mapping (ACOM) of a sputtered binary Ti-Ni thin film. a) Calculated virtual bright field image, b) phase map showing the distribution of Ti_3Ni_4 precipitates in austenite matrix (red: austenite, green: Ni_4Ti_3) and c) crystal orientation map regarding the phases depicted in b). The austenite phase exhibits uniform crystal orientation, while the orientation of the Ti_3Ni_4 precipitates varies.

Figure 64a depicts the virtual bright field image[3] of the studied region. Figure 64b and Figure 64c display the orientation maps for the region, using color-coding for the different orientations of Ni_4Ti_3 precipitations. All images show good correlation; however, small deviations are noticeable. On the left side of the virtual bright field image, the bright appearing regions do not match the orientation maps. There could be multiple reasons for this. Firstly, the beam size (probe size) is the most dominant factor affecting the diffraction patterns. Since the precipitates are small in size (less than 20 nm), the resolution of the patterns is sometimes insufficient to distinguish between the matrix and the precipitates. This problem can be resolved by decreasing the probe size. However, that introduces a new problem, as a decrease in the probe size also decreases the interaction of the beam with the specimen, leading to a decrease in the intensity of the individual reflections. Hence, the excitation probability of the characteristic reflections decreases, and identification of the phases becomes more difficult.

The second reason for the mismatch between the virtual bright field image and the orientation maps is the coherent growth of the precipitates inside the matrix. The main reflections for the matrix and the precipitates are located at the same position. Both patterns are differentiated with the additional reflections arising at the 1/7 position along <123>* reciprocal vectors of the B2 type austenite. These reflections can only be excited at the exact zone axis condition (excitation error = 0). For this reason, the reliability map calculated from

[3] Virtual bright field images are created by using a virtual diaphragm of predefined opening centered on the transmitted beam.

this area (not shown) is troubling, since both phases are very similar in terms of diffraction patterns.

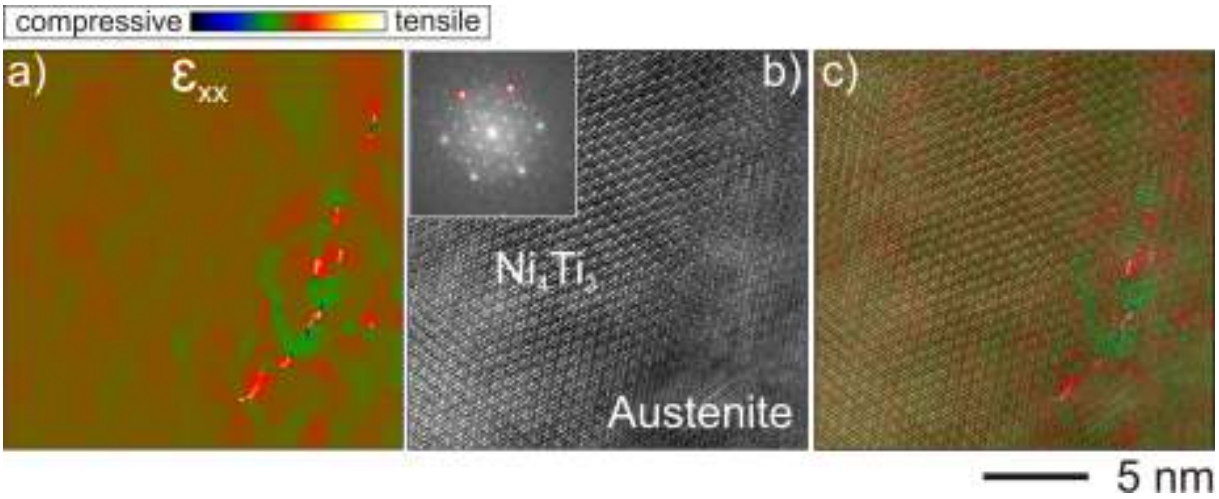

Figure 65: a) GPA map calculated from the austenite Ni_4Ti_3 interface. Local strains are visible at the interface, due to the nearly coherent growth of the precipitate inside the matrix. b) HRTEM micrograph with inserted FFT pattern. c) Overlaid images of a) and b), showing the exact position of the interface.

Figure 65a depicts the GPA map calculated from the austenite Ni_4Ti_3 interface. Figure 65b shows the HRTEM micrograph taken from the same area. The red circles in the FFT pattern inserted into the HRTEM micrograph mark the planes selected for the GPA calculation. Common lattice planes for both phases are selected in order to determine the possible strain phenomena. At the interface, local strains are visible due to the mismatching of both lattices. Various articles in the literature have reported that Ni_4Ti_3 grows completely coherently in the austenitic matrix. Our results do show tensile strain, (ε_{xx} map), which agrees with the results of Schyrivers et al., who also reported a compressive strain at the tip of the lens-shaped precipitate, although we did not detect this in our investigations. Rotation maps calculated similarly to the GPA maps did not show any remarkable effects. However, it is important to note that Cs-corrected electron microscopy is needed for quantitative interpretations. Figure 65c is the overlaid image of a and b, in order to show the exact position of the strain in the HRTEM micrograph.

Complementary TEM investigations were conducted with the cycled and uncycled samples. The cycled sample was pulled and pushed uniaxially, ex situ, 2000 times. A clear change in the microstructures was determined by high resolution imaging. Figure 66 depicts both microstructures with calculated FFT patterns. Stripes running horizontal to the micrograph are visible in the cycled sample (left). The reflections that arise in the FFT pattern are more smeared out in the cycled film. Both indications are in agreement with the previous results of Ren et al. After cycling, the same austenite matrix is deformed. With this deformation, the full transformation from austenite to martensite becomes impossible. After each cycle, less

energy is consumed. For this reason, these alloys do not show superelastic behavior. The additional reflections arising in the FFT patterns are possibly due to misaligned grains (the Moiré effect) and dynamical scattering effects, or are due to the strain bands.

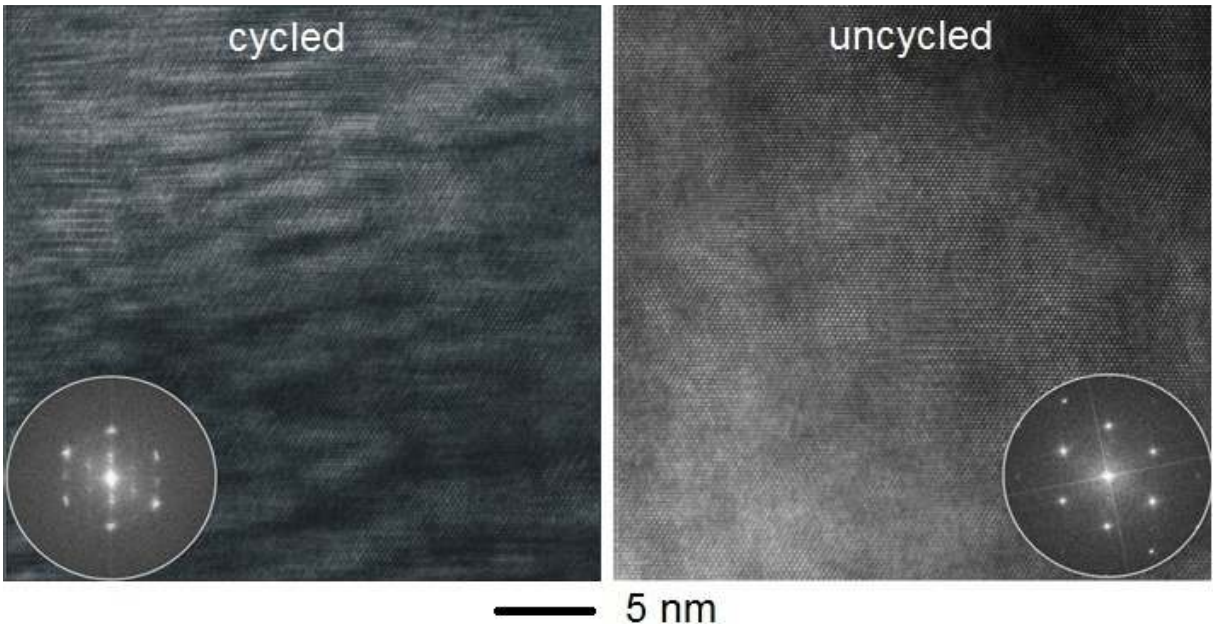

Figure 66: HRTEM micrographs recorded on the cycled (left) and uncycled (right) samples. A clear difference in the microstructure is visible in the images, as well as in the FFT patterns.

Another important deficiency in the literature is the lack of 3D visualization of the Ni_4Ti_3 precipitates in the matrix. The fine Ni_4Ti_3 precipitates increase the strength of the austenite, and limit the degree of plastic deformation during martensitic transformation under temperature or load cycling. Thus, it is possible to modify the Ms and the path by controlling the size and density of these precipitates. The effect of Ni_4T_{i3} precipitation on subsequent martensitic transformations has been further investigated by experimental efforts[114,115] that have dealt and the quantitative characterization of concentration and stress fields around coherent Ni_4Ti_3 precipitates. Schryvers et al. performed this type of investigation using a FIB microscope with a destructive method (sputtering off layers via an ion beam). However, similar TEM investigations were not carried out. One reason (or challenge) is the nearly coherent growth of the precipitates in the matrix; hence, the diffraction contrast, which is dominant in bright field imaging, is not sufficient for a 3D reconstruction. In the timeframe of this project, we tried to introduce an electron tomography approach. In contrast to the conventional tomography technique performed in the bright field mode, we performed this approach in the STEM mode, where the Z-contrast is the dominant contrast mechanism. In theory this eliminates the unwanted diffraction contrast and enhances the elemental specific imaging. However, there is still a slight contribution from the diffraction contrast in the Z-contrast images, because the scattered intensities with higher angles from different oriented

crystals are still collected by the HAADF detector. These effects were neglected in our interpretations.

However, other experimental difficulties could not be overcome. Since the precipitates are Ni rich and Ni has a high atomic number, the precipitates should appear to be bright in the STEM images (Z-contrast). However, they appear dark and their contrast did not change during tilting the sample; hence, the contrast is not orientation dependent. The nanoprobe EDX point measurements and the diffraction analyses revealed that the precipitates were in Ni_4Ti_3 in nature. The reason that the precipitates appear bright in the STEM images has to be the preferred etching process that occurred during the TEM specimen preparation. (This effect is described in the methodology section). For this reason, the precipitates appear as holes in the reconstructed images. Assuming that the holes fully represent the precipitates, we concluded that the lens shaped precipitates exhibit different widths and lengths. However, they are preferentially oriented with respect to the austenitic matrix $(001)_{Ni4Ti3} \parallel (111)_A$.

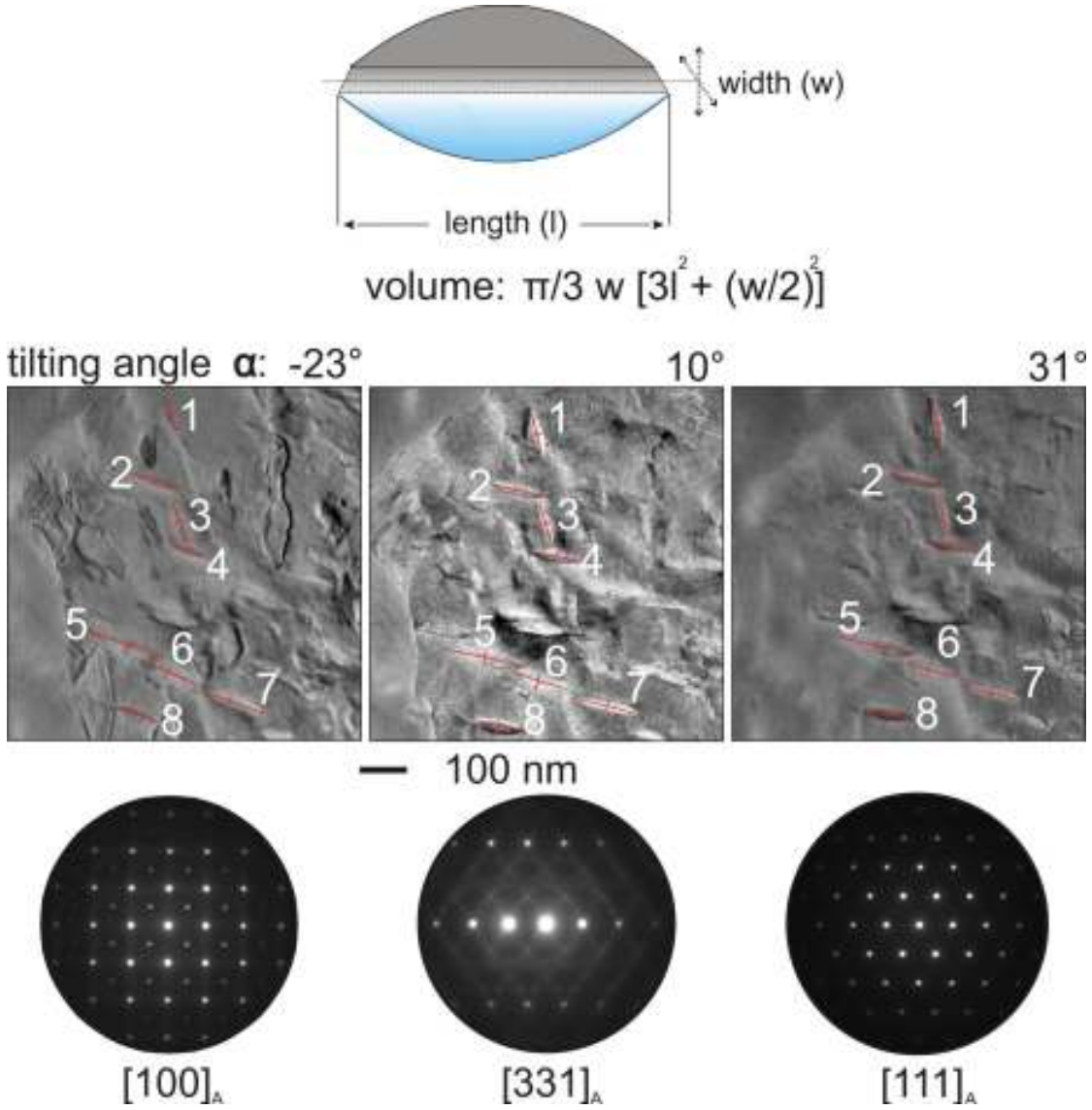

Figure 67: Ni_4Ti_3 precipitates dispersed in austenitic matrix (middle). The micrographs were recorded at three different zone axes (bottom). The length and the width of the precipitates are calculated from the given formula (top).

The average length and width of the precipitates were determined more precisely using a workaround technique, in addition to the electron tomography. One large grain was tilted to the three different zone axes, and the width and the length of each precipitate were measured. Figure 67 depicts the micrographs recorded on different zone axes. Assuming that the precipitates have a uniform lens shape, the average -or the most probable- volume was determined as changing between 5.1 * 10^5 nm^3 ,and 28.0 * 10^5 nm^3. Detailed data are provided in Table 7.

Table 7: Measured precipitate lengths and widths along different zone axes. The average Volume is calculated from these values.

Precipitate		1	2	3	4
Length (nm)	[100]	107,31	106,47	101,95	87,96
	[331]	101,56	91,41	93,74	72,97
	[111]	107,93	107,38	102,48	89,40
Width(nm)	[100]	37,48	21,60	22,10	23,27
	[331]	26,91	21,00	21,73	22,36
	[111]	27,59	21,05	23,79	23,11
Volume (nm^3)	[100]	$13,7*10^5$	$7,7*10^5$	$7,2*10^5$	$5,7*10^5$
	[331]	$8,8*10^5$	$5,5*10^5$	$6,0*10^5$	$3,8*10^5$
	[111]	$10,1*10^5$	$7,7*10^5$	$7,9*10^5$	$5,8*10^5$
Average Volume (nm^3)		$10,9*10^5$	$7,0*10^5$	$7,0*10^5$	$5,1*10^5$
Precipitate		5	6	7	8
Length (nm)	[100]	164,87	109,07	141,65	102,80
	[331]	155,92	103,63	126,81	93,29
	[111]	168,53	114,09	132,60	103,53
Width(nm)	[100]	34,12	39,19	25,50	28,15
	[331]	30,42	32,68	23,25	23,19
	[111]	35,20	37,96	26,57	24,35
Volume (nm^3)	[100]	$29,2*10^5$	$14,8*10^5$	$16,1*10^5$	$9,3*10^5$
	[331]	$23,2*10^5$	$11,1*10^5$	$11,7*10^5$	$6,3*10^5$
	[111]	$31,5*10^5$	$15,7*10^5$	$14,7*10^5$	$8,2*10^5$
Average Volume (nm^3)		$28,0*10^5$	$13,9*10^5$	$14,2*10^5$	$8,0*10^5$

Similar studies were performed on multiple grains from micrographs recorded at a lower magnification. More than 500 precipitates were taken into account, and the particle size distributions are given in Figure 68. The histograms show that the results are similar to those calculated from individual particles. The average length was 90 nm, and the width was 25 nm. These values gave a volume of $6.4 * 10^5$ nm^3.

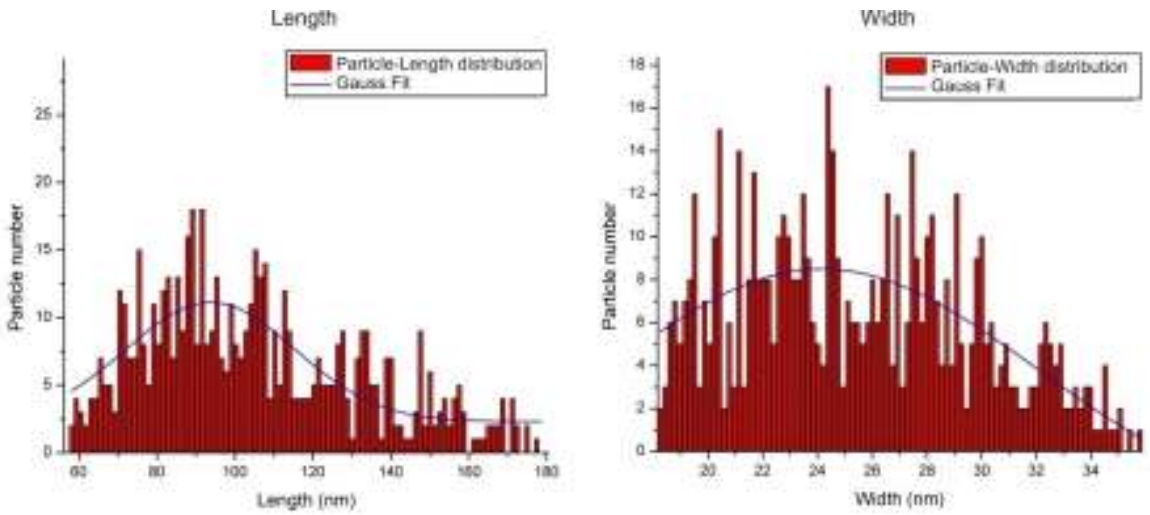

Figure 68: Particle-size distributions for the Ni_4Ti_3 precipitates. The most frequent length and width is determined as being 90 nm and 25 nm, respectively.

b) Ternary Ni-Ti-Cu Films:

In addition to the binary sputtered Ti-Ni films, ternary sputtered Ti-Ni-Cu films were investigated using TEM. Again, both cycled and uncycled specimens were investigated.

Figure 69a depicts the HAADF-STEM image and the elemental maps of the uncycled Ti-Ni-Cu film. The contrast in the HAADF-STEM images typically originates from the difference in the atomic number of the elements in the compound. The compound with a higher atomic number (Z) always shows higher intensity than a compound with a lower Z. Elemental maps recorded from the same region show an unequal distribution of the elements in the transmitted region, as expected from the HAADF-STEM image. The local chemical composition of the characteristic regions (numbered squares) is determined as being $(Ni_{0.75}Cu_{0.25})Ti$ (region 1), $(Ni_{0.45}Cu_{0.55})Ti_2$ (region 2), and $(Ni_{0.90}Cu_{0.10})Ti_2$ (regions 3 and 4).

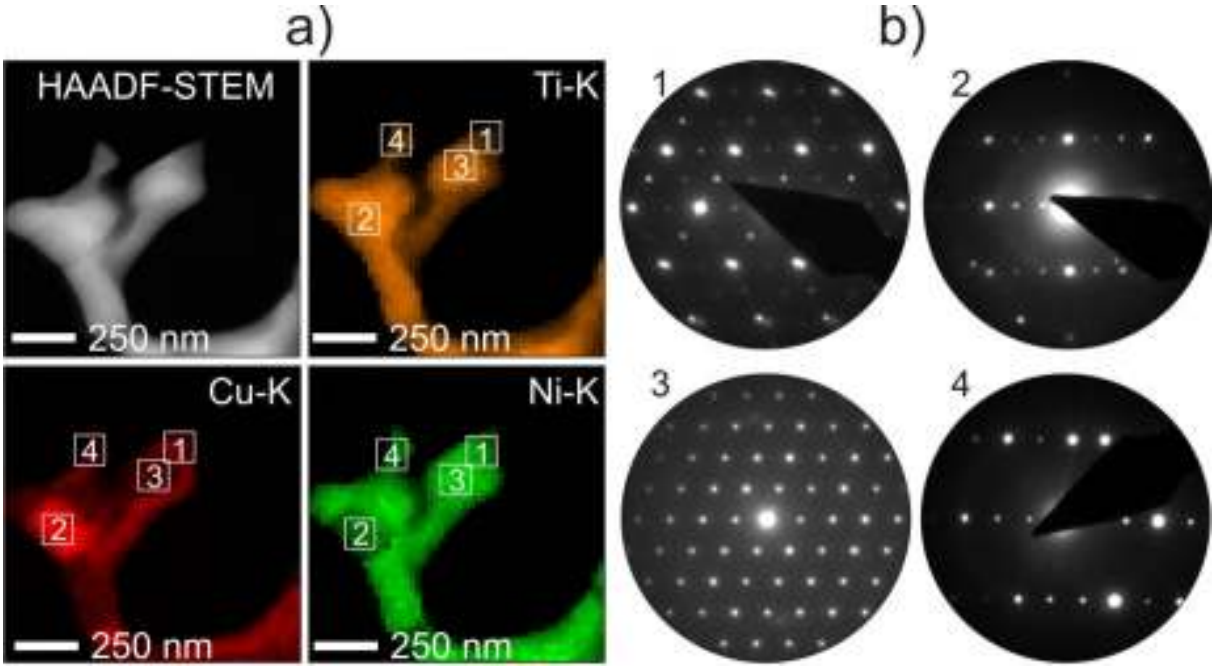

Figure 69: a) Chemical analysis of a Ti-Ni-Cu film by Z-contrast (top, left) and STEM-EDX elemental mapping. The local chemical composition was determined as: $(Ni_{0.75}Cu_{0.25})Ti$ (region 1), $(Ni_{0.45}Cu_{0.55})Ti_2$ (region 2), and $(Ni_{0.90}Cu_{0.10})Ti_2$ (regions 3 and 4). b) ED patterns recorded inside the regions, indicating different structures and/or orientations.

Holes inside the film are visible, arising from the selective etching of the specimen during TEM preparation. For this reason, a complete characterization of the film was not possible. Although the solvent for the jet polishing varied, this selective etching could not be avoided. Further specimens were prepared via the FIB lift out method.

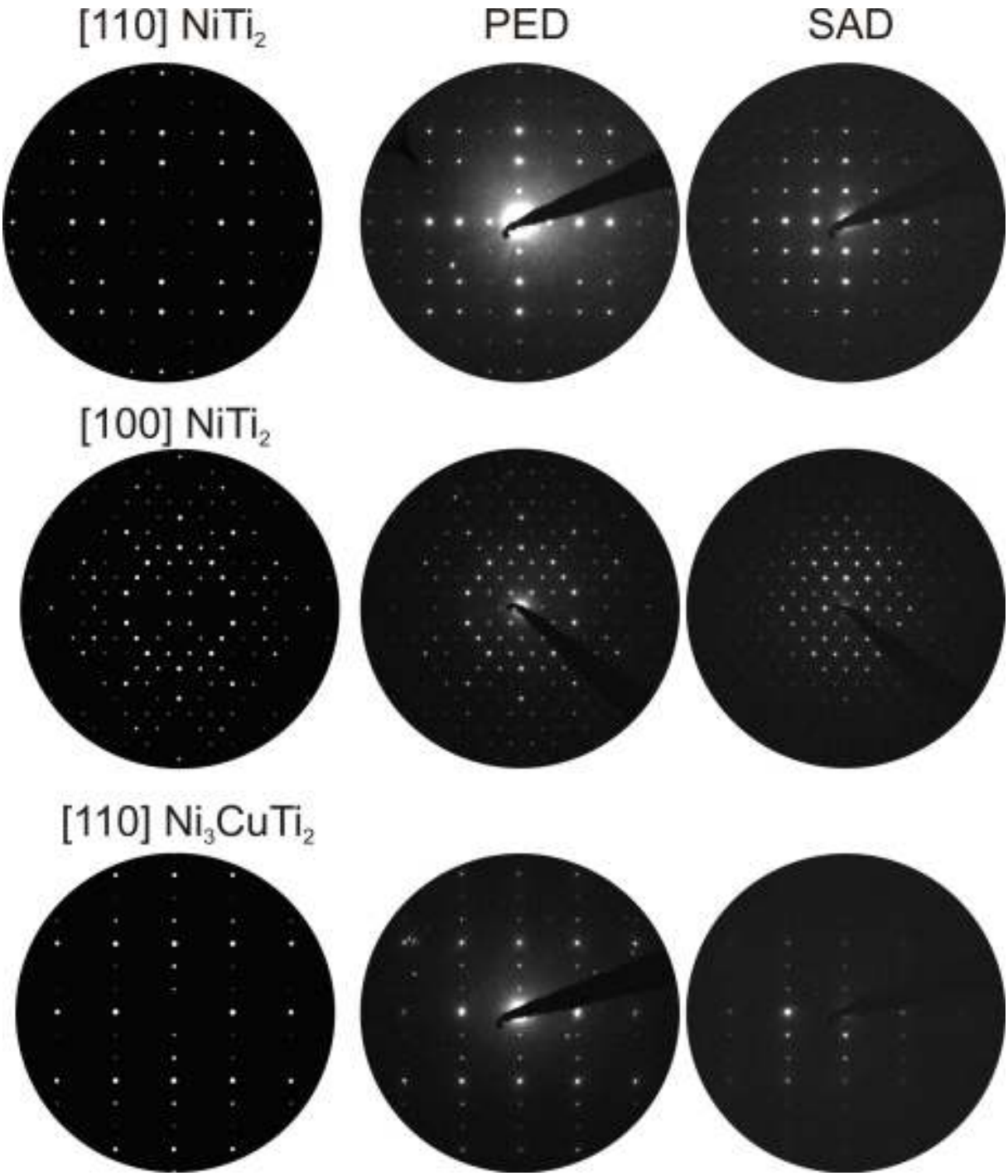

Figure 70: Different phases present in the Ni-Ti-Cu are identified via selected electron diffraction. Switching the PED mode, the patterns match very well with the simulated patterns (left column), because the dynamic scattering effects are eliminated.

The PED mode was also switched on for the uncycled ternary film. The PED pattern recorded from the $NiTi_2$ and Ni_3Cui_2 phases matched the simulated diffraction patterns very well, because the dynamic effects were reduced (Figure 70). The resolution was also enhanced when switching to the PED mode. The phases identified via electron diffraction are also in agreement with the EDX measurements.

The microstructure of the Ni-Ti-Cu alloy, mechanically cycled 2000 times is depicted in Figure 71a. Similar to the uncycled film, the cycled film consists of chemically and structurally different grains. Measured STEM-EDX elemental maps of Ni, Cu, and Ti show the inhomogeneous distribution of the elements (Figure 9 b-d.) The calculated Ti map shows a more or less a uniform contrast, whereas the Ni and Cu contents fluctuate in the same manner. The nanoprobe EDX measurements reveal that the regions are mostly Ti rich, exhibiting the composition of $(Ni_xCu_{1-x})Ti$ and $(Ni_x Cu_{1-x})Ti_2$.

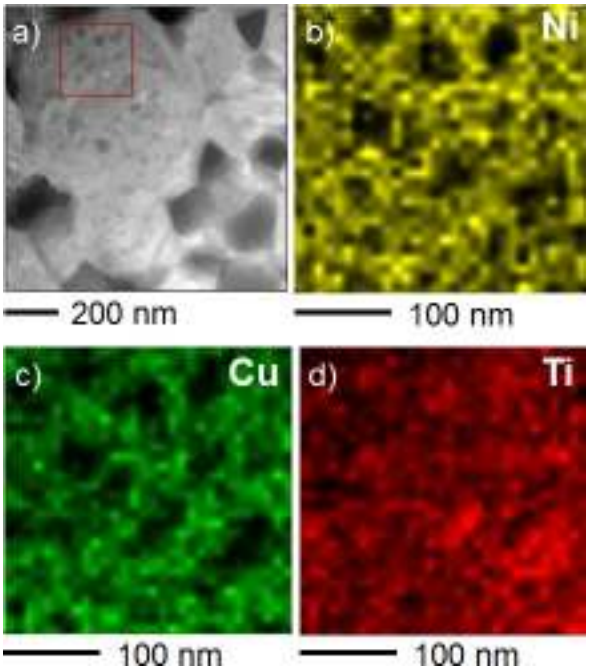

Figure 71: a) STEM image recorded on mechanically cycled Ti-Ni-Cu sputtered film and b)-d) EDX elemental maps from the region marked in a). Ni and Cu contents fluctuate in a correlated manner.

Although a one-to-one comparison between the cycled and pristine ternary films could not be made due to the differences in the TEM specimen preparation, similar results were obtained with respect to the grain size. No real change in the microstructures was observed. Thus, stable superelastic cycles of up to 2000 times were possible.

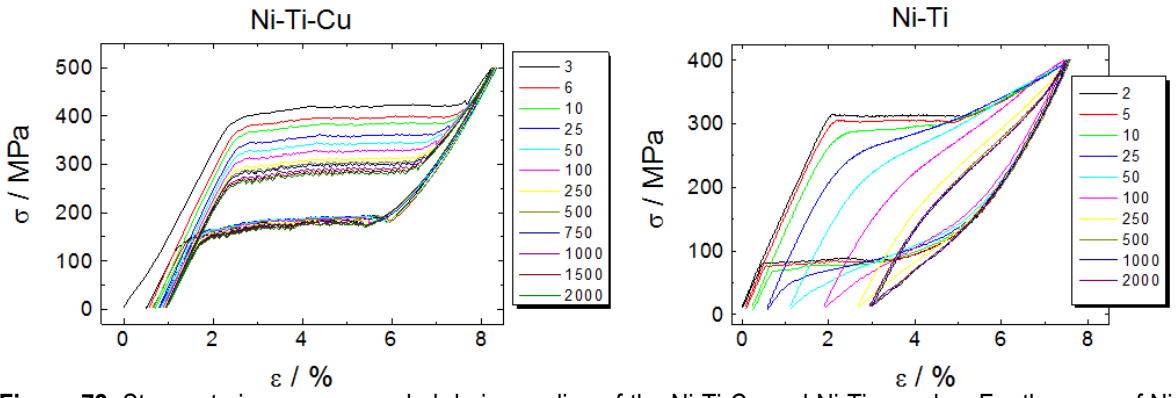

Figure 72: Stress-strain curves recorded during cycling of the Ni-Ti-Cu and Ni-Ti samples. For the case of Ni-Ti-Cu superelastic behavior was observed. After reaching 2000 cycles, the energy was consumed. For the binary case, the deformation of the austenitic matrix leads to unstable cycles[116].

Figure 72 displays the strain-stress curves of both binary and ternary sputtered thin films. The interrelation between the structure and the function is obvious. The ternary alloys showing no significant changes in the microstructure allow for stable mechanical cycles (high fatigue), whereas the binary alloys exhibit low fatigue due to the distortion of the matrix during cycling.

From the elastocaloric point of view, a high fatigue lifetime is necessary for the utilization of these films in the functional devices.

4.4 Summary and Conclusion

TEM techniques are demonstrated as a combined approach for the determination of structure and composition of the same nanoscale area. Thus, the interrelation of chemistry and structure can be analyzed using only one instrument, namely TEM. Advanced electron diffraction techniques, such as PED, offer enhanced potential for the identification of periodic modulations and structural disordering, by higher resolution and the imaging of intensities from higher order Laue zones.

As regards the choice of material, a 300 nm thick magnetocaloric Ni-Mn-In-Co film was investigated using TEM. Different regions with dissimilar structures and chemistry were observed. Here, modulated (nanotwinned) structures with different stacking periodicities (5M, 6M, 7M, and 8M) coexist with non-modulated structures that are twinned on a larger (microscopic) scale. The substantial variation in stacking sequences is also expected from the adaptive concept, and is predicted using diffraction simulation[117] for X-ray diffraction intensities. The Cr of the adhesion layer also diffuses into the functional layer so that, in

some spatially confined regions, In is replaced by Cr and Co when compared to the neighboring Cr-free regions.

Table 8 depicts the different compositions of the Ni-Mn-In-Co thin film and the observed structures.

Table 8: Composition-Structure interrelation in Ni-Mn-In-Co thin film

	Ni (%at.)	Mn (%at.)	In (%at.)	Co (%at.)	Cr (%at.)	Structure	Twinning
Region 1	50	36	12	2	-	modulated	Yes
Region 2	48	37	13	2	-	5M, 6M	No
Region 3	50	35	13	2	-	6M, 7M, 8M	No
Region 4	48	38	12	2	-	tetragonal	Yes
Region 5	46	33	8	9	4	tetragonal	Yes

Table 8 shows that the structure of the magnetocaloric Ni-Mn-In-Co thin film is strongly dependent on the chemical composition.

For the case of binary elastocaloric Ni-Ti thin films, the microstructure consisted of Ni_4Ti_3 precipitates and an R-Phase. The size of the precipitates was determined via electron tomography techniques and tilting. The length of the austenitic grains was measured as being several micrometers. Mechanical cycling of the specimen caused deformation of the austenitic matrix, which led to an incomplete transformation from austenite to martensite during cycling and to low fatigue, making these alloys unsuitable for functional caloric devices. On the other hand, the metals exhibiting a grain size of more than 1 μm showed a reduction in the fatigue endurance limit. In addition, the best possible size and volume of the Ni_4Ti_3 precipitates were determined using different techniques. Tilting the sample to a different zone axis allowed determination of the average distribution of the precipitates. These results were accompanied by challenging electron tomography measurements.

In contrast to the binary alloys, the ternary Ni-Ti-Cu films show stable mechanical cycles and a temperature change of 5 K is detected. These are encouraging properties for caloric devices and were correlated to the microstructure. TEM investigations showed that the grain sizes of the present phases are significantly smaller than are those of Ni-Ti films. Mechanical cycling did not cause a significant change in the microstructure. Small grain sizes minimize the generation of the dislocations inside the grains. The dislocations introduced during the cycling accumulate at the high energetic grain boundaries. Since the density of the newly introduced dislocations decreases and the glide movement of the grains is enhanced by smaller grain sizes, the number of stable mechanical cycles is also increased.

5. OUTLOOK

Although the results are encouraging for achieving SME in $Fe_{70}Pd_{30}$ thin films and for fabricating functional caloric devices based on magnetic or elastic responses, there is still further work to do.

A group in Leipzig has already achieved the development of a thick epitaxial $Fe_{70}Pd_{30}$ film exhibiting an fct phase via molecular beam epitaxy. The kinetics in the MBE chamber were definitely different from those in the sputtering chambers used in our research; however, a clear definition of kinetics is missing. The relaxation mechanism to reduce the stress during epitaxial growth is also not fully understood. One possible solution for understanding this phenomenon has been developed by Eibel et al., for the case of ferroelectrics. They sputtered metallic layers onto zigzag shaped, [100] oriented MgO substrates, and achieved a variable change of the in-plane lattice parameter along the entire substrate. A cross sectional TEM analysis of one sample will help to understand the relaxation mechanism inside these films. Since the strain varies continuously at the film-substrate interface, the possible relaxation at different regions can be monitored. Furthermore, the magnetic nature of the $Fe_{70}Pd_{30}$ thin films also needs to be investigated via Lorentz and electron holography techniques. For example, the magnetic nature of the domain walls in the transition area from single to polycrystalline regions needs to be studied in greater depth. The correspondence of the magnetic easy axis of the thin films with the martensite vector has to be determined in differently sputtered films (the martensite vector is determined as the direction of the short axis in the crystal[118]). Since the magnetic anisotropy in the films depends on many factors, such as thickness, crystal structure, and chemical composition, the research has to be systematically performed in order to understand the influence of each feature on the magnetism.

For ternary Fe-Pd-Pt films, ACOM measurements and Cs-corrected high resolution imaging experiments are scheduled, in order to understand the disordering phenomenon occurring during sample cooling.

Fabrication of functional caloric devices based on thin films will still require much work. The 5 K temperature change obtained here is remarkably insufficient for the required cooling in microsystem technology. New microstructures need to be developed by alloying and heat treatments, and must subsequently be characterized. The newly introduced TEM characterization technique, ACOM, has to be tuned for the binary Ni-Ti alloys. The parameter most influential for the ACOM measurements is the size of the precipitates. Since the technique is based on the collection of the local diffraction patterns, small precipitates are

sometimes not recognized in the calculated images. Using a focused beam for the measurements causes disc shaped reflections, which also decreases the visibility of the characteristic superstructure reflections inside the matrix. Hence, a convenient method needs to be found for the analyses performed on thin films containing small precipitates. One possible answer is to use the STEM mode in the analyses, in order to obtain a nanobeam. However, in so doing, the back focal plane of the objective lens also needs to be shifted towards the sample. This is not possible in conventional STEM, due to the design of the microscope and software. Additional current must be manually applied to the objective lens. We have agreed with C. Kübel to make these alignments at the Karlsruhe Institute of Technology.

Another challenging task arising during ACOM measurements is the double diffraction phenomenon, which occurs in the presence of the R-Phase in the matrix. The characteristic superstructure reflections of the R-Phase are not excited when working away from the specific zone axes. Hence, they cannot be compared with the databases. This means that each sample requires a specimen-specific alignment. The challenges in the tomography experiments were mentioned briefly in the previous sections. The main problem was the preferential etching of the precipitates, and thus their dark appearance in the STEM images. This problem can be reduced by converting the contrast in the software; however, the dark regions occurring due to the high thickness of the specimen are also converted into bright areas, and are subsequently constructed as precipitates. Careful specimen preparation is essential for a tomography approach.

For Ni-Ti-Cu films, a cycled film will be prepared via the FIB technique in order to make a direct comparison between cycled and uncycled samples.

.

REFERENCES

1 K. Otsuka, C. M. Wayman, Mechanism of shape memory effect and superelasticity, In: Otsuka, K. Wayman, C.M. (Eds.), Shape Memory Materials. Cambridge University Press, Cambridge, 1998, pp. 27–48.

2 A. Ölander, An electrochemical investigation of solid Cadmium-Gold alloy, J. Am. Chem. Soc., 54, 1932, pp. 3819-3833.

3 A. Ölander, The crystal structure of AuCd, Zeit für Kristal., 83, 1932, p.145.

4 S. Aksoy, T. Krenke, M. Acet, E. F. Wassermann, X. Moya, L. Mañosa and A. Planes, Tailoring magnetic and magnetocaloric properties of martensitic transitions in ferromagnetic Heusler alloys, Appl. Phys. Lett. 91, 2007, p. 241916.

5 V. K. Pecharsky, K. A. Gschneidner, Giant magnetocaloric effect in Gd5\(Si2Ge2\), Phys. Rev. Lett. 78, 23, 1997, pp. 4494-4497.

6 L. Manosa, D. Gonzales- Alonso, A. Planes, E. Bonnot, M. Barrio, J.-L. Tarnarit, S. Aksoy, M. Acet, Giant solid-state barocaloric effect in the Ni–Mn–In magnetic shape memory alloy, Nature Mater. 9, 2010, pp. 478–481.

7 R. Kainuma, Y. Imano, W. Ito, Y. Sutou, H. Morito, S. Okamoto, O. Kitakami, K. Oikawa, A. Fujita, T. Kanomata and K. Ishida, Magnetic-field-induced shape recovery by reverse phase transformation, Nature 439, 2006, pp. 957–960.

8 D. Bourgault, J. Tillier, P. Courtois, D. Maillard and X. Chaud, Large inverse magnetocaloric effect in $Ni_{45}Co_5Mn_{37.5}In_{12.5}$ single crystal above 300 K, Phys. Lett. 96, 2010, p.132501.

9 R. Niemann, O. Heczko, L. Schultz and S. Fähler, Metamagnetic transitions and magnetocaloric effect in epitaxial Ni–Co–Mn–In films, Appl. Phys. Lett. 97, 22, 2010, p. 222507.

10 M. Wuttig, L. Liu, K. Tsuchiya and R. D. James, Occurrence of ferromagnetic shape memory alloys, J. Appl. Phys., 87, 2000, p. 4707.

11 J. Cui, T.W. Shield and M. Wuttig, Magnetostriction of stress-induced martensite, Appl. Phys. Lett., 85, 9, 2004, pp. 1642-1644.

12 D. C. Lagoudas (ed.), Shape Memory Alloys, DOI: 10.2007/978-0-387-47685-8_1, Springer Science and Business Media, LLC 2008.

13 R. D. James and M. Wuttig, Magnetostriction of martensite, Phil. Mag. A 77, 1998, pp.1273–1299.

14 J. Cui, T. W. Shield and R. D. James, Phase transformation and magnetic anisotropy of an iron-palladium ferromagnetic shape-memory alloy, Acta Mater. 52, 2004, pp.35–47.

15 T. Sohmura, R. Oshima, F. E. Fujita, Trans. Jpn. Inst. Met., 1984, 14, pp. 885-886.

16 J. Cui, T. W. Shield, Ferromagnetic shape memory effects in an iron palladium alloy, Journal of Mechanics of Materials and Structures 2, 3,2007 pp. 505-528.

17 M. Sugiyama, R. Oshima, F. E. Fujita, Thermoelastic fcc-fct martensitic transformation in Fe–Pd alloy. Trans. Jpn. Inst. Met.,1984, 25, 858.

18 K. Otsuka, X. Ren, Recent Developments in the research of shape memory alloys, Intermetallics, 7, 5, 1999, pp. 511-528.

19 T. Fukuda, T. Sakamoto, T. Kakeshita, T. Takeuchi, K. Kishio, Rearrangement of martensite variants in iron-based ferromagnetic shape memory alloys under magnetic field, Materials Transactions, 45, 2, 2004, pp. 188-192.

20 H. Kato, Y. Liang, M. Taya, Stress-induced FCC/FCT phase transformation in Fe–Pd alloy, Scripta Materialia, 46, 6, 2002, pp. 471-475.

21 T. Kubota, T. Okazaki, Y. Furuya, T. Watanabe, Large magnetostriction in rapid-solidified ferromagnetic shape memory Fe–Pd alloy, Journal of magnetism and magnetic materials, 239, 1, 2002, pp. 551-553.

22 J. Buschbeck, I. Lindemann, L. Schultz and S. Fähler, Growth, structure and texture of epitaxial $Fe_{100-x}Pd_x$ films deposited on MgO(100) at room temperature: An x-ray diffraction study, Phys. Rev. B 76, 2007, p. 205421.

23 T. Edler, J. Buschbeck, C. Mickel, S. Fähler, S. G. Mayr, Mechanisms of stress generation and relaxation during pulsed laser deposition of epitaxial Fe–Pd magnetic shape memory alloy films on MgO, N. J. of Physics, 10, 2008, p. 063007.

24 E.C. Bain, The Nature of Martensite, Trans. Am. Inst. Miner. Met. Eng., 70, 1924, pp. 25-35.

25 J. Buschbeck, I. Opahle, M. Richter, U. K. Rößler, P. Klaer, M. Kallmayer, H. J. Elmers, G. Jakob, L. Schultz, S. Fähler, Full tunability of strain along the fcc-bcc bain path in epitaxial films and consequences for magnetic properties, Phys. Rev. Lett., 103, 2009, p. 216101.

26 K. H. J. Buschow, P. G. van Engen, R. Jongebreur, J. of Magnetism and Magnetic Mat. 38, 1983. pp. 1-22.

27 D. B. Williams and C. B. Carter, Transmission Electron Microscopy: A Textbook for Materials Science, Springer, New York, 1996- 2009.

28 J. C. H. Spence, Experimental high-resolution electron microscopy, Oxford U. Press, New York, ISBN0-19-505405-9, 1988.

29 R. Kilaas, Optimal and near-optimal filters in high-resolution electron microscopy, J. Microscopy, 190, 1998, pp. 45-51.

30 A. V. Crewe, J. Wall and J. Langmore, Visibility of single atoms, Science, 168, 1970, p. 1338.

31 J. Goldstein, Scanning Electron Microscopy and X-Ray Microanalysis, Springer, ISBN 978-0-306-47292-3, 2003, Retrieved 26 May 2012.

32 A. L. Bendersky and F. W. Gayle, Electron diffraction using transmission electron microscopy, Journal of Research of the National Institute of Standards and Technology, 106, 2001, pp. 997– 1012.

33 P. Oleynikov, S. Hovmöller, X. D. Zou, Precession electron diffraction: Observed and calculated intensities, 107, Issues 6– 7, 2007, pp. 523–533.

34 www.nanomegas.com

35 E. F. Rauch, J. Portillo, S. Nicolopoulos, D. Bultreys, S. Rouvimov, P. Moeck, Automated Nano crystal orientation and phase mapping in the TEM on the basis of PED, Precession Electron Crystallography, 225, 2- 3, pp. 103-109.

36 M. J. Hÿtch, E. Snoeck and R. Kilaas, Quantitative measurement of displacement and strain fields from HREM micrographs. Ultramicroscopy, 74, 1998, pp.131–146.

37 W. Tirry, D. Schryvers, Linking a completely three-dimensional nanostrain to a structural transformation eigenstrain, Nature Mater. 8, 9, 2009, pp. 752- 757.

38 S. Bals, W. Tirry, R. Geurts, Z. Yang and D. Schryvers, High-quality sample preparation by low kv fib thinning for analytical tem measurements, Microscopy and Analysis, 13, 02, 2007, pp. 80- 86.

39 Sven Hamann, Ph.D. Thesis, Ruhr University Bochum, 2013.

40 J. D. Griffiths, Introduction to Quantum Mechanics, Second Edition, pp. 207- 210.

41 S. Chikazumi, Physics of Magnetism, 2nd edn., John Wiley, New York, 1964.

42 S. Bobbio, Electrodynamics of Materials, Academic Press, San Diego, 1999.

43 F. G. West, Uniaxial anisotropy due to magnetoelastic energy in constrained polycrystalline films, J. Appl. Phys., 35, 1964, p. 1827.

44 P. Zeeman, Über einen einfluss der magnetisirung auf die natur des von einer substanz emittieten lichtes, Verhandlungen der Physikalischen Gesekkschaft zu Berlin, 1992, p. 127.

45 S. Weinberg, The quantum Theory of Field, vol. 2, Chap. 23, Cambridge University Press, 1995.

46 K. Wasa**,** I. Kanno**,** H. Kotera, Handbook of Sputtering Technology (Second Edition), Elsevier Inc., 2012, ISBN: 978-1-4377-3483-6.

47 L. E. Tanner, R. Gronsky, A. R. Pelton, Tweed- The microstructure of pretransformation state, Journal of Metals, 37, 11, p. A16.

48 M. E. Gruner and P. Entel, Impact of local lattice distortions on the structural stability of Fe-Pd magnetic shape-memory alloys, Physical Review B 83, 2011, p. 214415.

49 S. Kauffmann-Weiss, M. E. Gruner, A. Backen, L. Schultz, P. Entel and S. Fähler, magnetic nanostructures by adaptive twinning in strained epitaxial films, Phys. Rev. Lett. 107, 2011, p. 206105.

50 T. Edler, S. G. Mayr, Film lift–off from MgO: Freestanding single crystalline fe–pd films suitable for magnetic shape memory actuation– and beyond, Adv. Mat. 22, 44, 2010, pp. 4969- 4972.

51 L. Kühnemund, T. Edler, I. Kock, M. Seibt, S. G. Mayr, Epitaxial growth and stress relaxation of vapor-deposited Fe–Pd magnetic shape memory films, New J. Phys, 11, 2009, p. 113054.

52 Y. S. Toluloukian, R. W. Powell, Thermophysical Pop of Matter, vol. 10, IFI/Plenium, New York, 1975, p. 82.

53 E. Dologlou, Estimation of diffusion coefficients of Cr and Ga in MgO at temperature of the earth`s lower mantle, Int. J. Scientific and Eng. Res., 4, 1, 2013, p. 1.

54 S. Kauffmann- Weiss, B. Erkartal, L. Schultz, L. Kienle, S. Fähler, Influence of kinetics on the phase formation in epitaxial Fe-Pd films, Scr. Mater. 68, 6, 2013, pp. 412- 415.

55 C. Bechtold, A. Lotnyk, B. Erkartal, L. Kienle, E. Quandt, Structural characterization of sputtered $Fe_{70}Pd_{30}$ thin films during ex situ and in situ TEM heating, Adv. Eng. Mater. 14, 8, 2012, pp. 716- 723.

56 S. Fähler, H. U. Krebs, Calculations and experiments of material removal and kinetic energy during pulsed laser ablation of metals, Appl. Surf. Sci., 96- 98, 1996, p. 61.

57 Z. Wang, T. Iijima, G. He, T. Takahashi, K. Oikawa, Y. Furuya, Properties of sputter-deposited Fe-Pd thin films, Proc. SPIE 4234, Smart Materials, 284, 2001, doi:10.1117/12.424418.

58 K. Tsuckiya, T. Nojiri, H. Ohtsuka, M. Umemeto, Effect of Co and Ni on martensitic transformation and magnetic properties in Fe-Pd ferromagnetic shape memory alloys: Structural and functional control of materials through solid-solid phase transformations in high magnetic field, Mater. Trans. JIM, 44, 12., 2003, pp. 2499-2502.

59 R. Oshima, M. Sugiyama, F. E. Fujita, Tweed structures associated with fcc-fct transformations in Fe-Pd alloys, Metallurgical Transactions A, 19A, 1988, p. 803.

60 Y. Ma, A. Setzer, J. W. Gerlach, F. Frost, P. Esquinazi, S. G. Mayr, Freestanding single crystalline Fe–Pd ferromagnetic shape memory membranes – Role of mechanical and magnetic constraints across the martensite transition, Adv. Func. Mat. 22, 12, 2012, pp. 2529- 2534

61 E. Warburg, Magnetische untersuchungen. Ueber einige wirkungen der coërcitivkraft, Ann. Phys., 249, 1981, p. 141– 164.

62 S. Fähler, U. K. Rößler, O. Kastner, J. Eckert, G. Eggeler, H. Emmerich, P. Entel, S. Müller, E. Quandt, K. Albe, Caloric effects in ferroic materials: New concepts for cooling, Adv. Eng. Mat., 14, Issue 1- 2, 2012, pp. 10– 19.

63 K. A. Gschneidner Jr., V. K. Pecharsky, A. O. Pecharsky and C. B. Zimm, Recent developments in magnetic refrigeration. Materials Science Forum, 69– 76, 1999, pp. 315– 317.

64 O. Tegus, E. Brück, F. R. de Boer, K. H. J. Buschow, Transition-metal-based magnetic refrigerants for room-temperature applications, Nature 415, 6868, 2002, pp. 150– 152.

65 J. K. Allafi, A. Dlouhy, G. Eggeler, Ni_4Ti_3 precipitation during aging if NiTi shape memory alloys and its influence on martensitic phase transformation, Acta Mat., 50, 2002, pp. 4255- 4274.

66 A. Sozinov, A. A. Likhachev, N. Lanska, K. Ullakko, Giant magnetic-field-induced strain in Ni-Mn-Ga seven-layered martensitic phase, Appl. Phys. Lett., 80, 10, 2002, pp. 1746- 1748.

67 R. W. Overholser, M. Wuttig, D. A. Neumann**,** Chemical ordering in Ni-Mn-Ga Heusler alloys, Scr. Mater., 40, 10, 1999, pp. 1095- 1102.

68 V. V. Kokorin, V. V. Martynov, V. A. Chernenko, Stress-induced martensitic transformations in Ni_2MnGa, Scr. Metall. Mater., 26, 2, 1992, pp. 175- 177.

69 V. A. Chernenko, E. Cesari, V. V. Kokorin, I. N. Vitenko**,** The development of new ferromagnetic shape memory alloys in Ni-Mn-Ga systems, Scr. Metall. Mater., 33, 8, 1995, pp. 1239- 1244.

70 J. Enkovaara, A. Ayuela, A. T. Zayak, P. Entel, L. Nordström, M. Dube, J. Jalkanen, J. Impola, R. M. Nieminen, Magnetically driven shape memory alloys, Mater. Sci. Eng. A, 378, 2004, pp. 52- 60.

71 P. J. Webster, K. R. A. Ziebeck, S. L. Town, M. S. Peak, Magnetic order and phase transformation in Ni_2MnGa, Philos. Mag. B, 49, 1984, pp. 295- 310.

72 J. Pons, V. A. Chernenko, R. Santamarta, E. Cesari, Crystal structure of martensitic phases in Ni-Mn-Ga shape memory alloys, Acta Mater. 48, 2000, pp. 3027-3038.

73 L. Righi, F. Albertini, L. Pareti, A. Paoluzi, G. Calestani, Commensurate and incommensurate 5M modulated crystal structures in Ni-Mn-Ga martensitic phases, Acta Mater., 55, 2007, pp. 5237- 5245.

74 L. Righi, F. Albertini, E. Villa, A. Paoluzi, G. Calestani, V. Chernenko, S. Besseghini, C. Ritter, F. Passaretti, Crystal structure of 7M modulated Ni-Mn-Ga martensitic phase, Acta Mater., 56, 2008, pp. 4529- 4535.

75 S. Kaufmann, U. K. Rößler, O. Heczko, M. Wuttig, J. Buschbeck, L. Schultz, S. Fähler, Adaptive modulations of martensites, Phys. Rev. Lett, 104, 2010, p. 145702.

76 A. G. Khachaturyan, S. M. Shapiro, S. Semenovskaya, Adaptive phase formation in martensitic transformation, Phys. Rev. B, 43, 13, 1991, pp. 10832- 10843.

77 B. Erkartal, V. Duppel, R. Niemann, L. Schultz, S. Fähler, U. Schürmann, L. Kienle, Structure and composition of magnetocaloric Ni-Mn-In-Co thin films on the nanoscale-A TEM study, Adv. Eng. Mater., 14, 8, 2012, pp. 710- 715.

78 S. Kaufmann, R. Niemann, T. Thersleff, U. K. Rößler, J. Buschbeck, B. Holzapfel, L. Schulz, S. Fähler, Modulated martensite: Why it forms and why it deforms easily, New J. Phys., 13, 2011, 053029.

79 D. Y. Cong, Y. D. Wang, P. Zetterstrom, R. L. Peng, R. Delaplane, X. Zhao, L. Zuo, Determination of crystal structure and crystallographic characteristics in Ni-Mn-Ga ferromagnetic shape memory alloys, Mat. Sci. Tech. Minerals and Mining, 2005, p. 21.

80 A. Chakrabarti and S. R. Barman, Theoretical prediction of shape memory behavior and ferrimagnetism in Mn_2NiIn, Appl. Phys. Lett., 94, 2009, p.161908.

81 L. Kienle and A. Simon, Polysynthetic twinning in $RbIn_3S_5$, J. Sol. State Chem., 167**,** 2002, p. 1.

82 K. Otsuka, X. Ren, Recent developments in the research of shape memory alloys, Intermetallics, 7, 1999, pp. 511– 528.

83 S. K. Wu, H. C. Lin, Recent development of TiNi-based shape memory alloys in Taiwan, Mater. Chem. Phys., 64, 2000, pp. 81– 92.

84 J. V. Humbeeck, Non-medical applications of shape-memory alloys, Mater. Sci. Eng. A 273– 275, 1999, pp. 134–48.

85 E. Bonnot, R. Romero, L. Manosa, E. Vives and A. Planes, Elastocaloric effect associated with the martensitic transition in shape-memory alloys, Phys. Rev. Lett.,100, 2008, p.125901.

86 C. P. Frick, A. M. Ortega, J. Tyber, K. Gall, H. J. Maier, Multiscale structure and properties of cast and deformation processed polycrystalline NiTi shape memory alloys, Metall. Mater. Trans. A, 35A, 2004, pp. 2013- 20205.

87 T. V. Philip and P. A. Beck, Transactions of the American institute of mining and metallurgical society of AIME, 209, 1957, pp. 1269- 1271.

88 J. Beyer, Recent Advances in the martensitic transformations of Ti-Ni Alloys, J. de Physique IV, 5, 1995, p. 433.

89 R. F. Hehemann and G. D. Sandrock, Relations between the premartensitic instability and the martensite structure in TiNi, Scripta Metallurgica, 5, 9, 1971, pp.801- 806.

90 K. Otsuka, T. Sawamura and K. Shimizu, Crystal structure and internal defects of equiatomic TiNi martensite, Physica Status Solidi A, 5, 2, 1971, pp. 457- 470.

91 Y. Kudoh, M. Tokonami, S. Miyazaki and K. Otsuka, Crystal structure of the martensite in Ti-49.2 at. %Ni alloy analyzed by the single crystal X-ray diffraction method, Acta Metallurgica, 33, 11, 1985, pp. 2049- 2056.

92 C. M. Hwang, M. Meichle, M. B. Salamon, C. M. Wayman, Transformation behaviour of a $Ti_{50}Ni_{47}Fe_3$ alloy II. Subsequent premartensitic behaviour and the commensurate phase, Philos. Mag. A, 47, 1983, pp. 31- 62.

93 T. Tadaki, C. M. Wayman, Electron microscopy studies of martensitic transformations in $Ti_{50}Ni_{50-x}Cu_x$ alloys. Part I. Compositional dependence of one-third reflections from the matrix phase, Metallography, 15, 1982, p. 247.

94 P. L. Potapov, A. V. Shelyakov, D. Schryvers, On the crystal structure of Ti-Ni-Cu martensite, Scripta Mater., 41, 2001, p. 1.

95 M. Nishida and C. M. Wayman, Proc. ICOMAT '86, (Japan Inst. of Metals, 1987) pp. 653- 658.

96 T. Hara, T. Ohba, K. Otsuka, M. Nishida, Mater. Trans. JIM, 38, 1997, pp. 277- 284.

97 M. Nishida, C. M. Wayman and T**.** Honma, Precipitation processes in near-equiatomic TiNi shape memory alloys, Met. Trans. 17A,1986, pp. 1505- 1513.

98 S. Cao, C. Somsen, M. Croitoru, D. Schryvers, G. Eggeler, Focused ion beam/scanning electron microscopy tomography and conventional transmission electron microscopy assessment of Ni_4Ti_3 morphology in compression-aged Ni-rich Ni–Ti single crystals, Scripta Materialia 62**,** 2010, pp. 399– 402.

99 A. Taylor, R. W. Floyd, Precision measurements of lattice parameters of non-cubic crystals, Acta Crystall., 3, 1950, p. 285.

100 F. J. Gil, J. M. Manero and J. A. Planell, Effect of grain size on the martensitic transformation in NiTi alloy, J. Mater. Sci., 30, 1995, 10, pp. 2526- 2530.

101 J. Pelton, Nitinol Fatigue: A review of microstructures and mechanisms, J. of Materials Eng. and Perf., 20, 4- 5, 2011, pp. 613- 617.

102 G. Eggeler, E. Hornbogen, A. Yawny, A. Heckmann and M. Wagner, Structural and functional fatigue of NiTi shape memory alloys, Mater. Sci. Eng., A, 378, 1- 2, 2004, pp. 24- 33.

103 R. M. Tabanli, N. K. Simha, and B. T. Berg, Mean stress effects on fatigue of NiTi, Mater. Sci. Eng. A,, 273– 275, 1999, pp. 644– 648.

104 S. Miyazaki, A. Ishida, Martensitic transformation and shape memory behavior in sputter deposited TiNi-base thin films, Mater. Sci. Eng. A, 273– 275, 1999, pp.106– 133.

105 K. Yamazaki, S. Kajiwara, T. Kikuchi, K. Ogawa, S. Miyazaki, Super-high strength shape memory thin films, J. Phys. IV, 112, 2003, pp. 841– 844.

106 M. Tomozawa, H. Y. Kim, S. Miyazaki, Microactuators using R-phase transformation of sputter-deposited Ti-47.3Ni shape memory alloy thin films, J. Intell. Mater. Syst. Struct.,17, 2003, pp. 1049– 1058.

107 A. Ishida, M. Sato, S. Miyazaki, Mechanical properties of Ti-Ni shape memory thin films formed by sputtering, Mater. Sci. Eng. A, 273– 275, 1999, pp. 754– 757.

108 K. Yamazaki, S. Kajiwara, T. Kikuchi, K. Ogawa, S. Miyazaki, Mechanical properties of parent phase of sputter-deposited shape memory thin films of Ti-rich Ti-Ni-Cu alloys, Trans. Mater. Res. Soc. Jpn., 26, 2001, pp. 299– 302.

109 A. Ishida, M. Sato, Philos. Mag.,1478– 6443, 2007, pp. 5523– 5538.

110 S. Miyazaki, Y. Igo and K. Otsuka, Effect of thermal cycling on the transformation temperatures of Ti-Ni Alloys, Acta Metall., 1986, 34, pp. 2045– 2051.

111 K. N. Melton and O. Mercier, Fatigue of NiTi thermoelastic martensites, Acta Metall., 27, 1979, pp. 137– 144.

112 T. H. Nam, T. Saburi, K. Shimizu, Shape memory characteristics and lattice deformation in Ti-Ni-Cu alloys, Mater. Trans. JIM, 31, 1990, p. 959.

113 K. Otsuka, X. Ren, Physical metallurgy of Ti-Ni-based shape memory alloys, Prog. Mater. Sci., 50, 2005, pp. 511- 678.

114 Z. Q. Yang, W. Tirry, D. Schryvers, Analytical TEM investigations on concentration gradients surrounding Ni_4Ti_3 precipitates in Ni-Ti shape memory material, Scripta Mater., 52, 2005, pp.1129- 1134.

115 W. Tirry, D. Schryvers, Quantitative determination of strain fields around Ni_4Ti_3 precipitates in NiTi, Acta Mater., 33, 2005, pp. 1041- 1049.

116 C. Bechtold, C. Chluba, R. Lima de Miranda, E. Quandt, High cyclic stability of the elastocaloric effect in sputtered TiNiCu shape memory films, Applied Physics Letters, 101, 9, 2012, p. 091703.

117 A. Ustinov, L. Olikhovska, N. Glavatska, I. Glavatskyy, Diffraction features due to ordered distribution of twin boundaries in orthorhombic Ni-Mn-Ga crystals, J. Appl. Cryst., 42, 2009, pp. 211- 216.

118 Y. Murakami, D. Shindo, T. Sakamoto, T. Fukuda, T. Kakeshita, Magnetic domain structure in the presence of very thin martensite plates: Electron holography study on a thin-foil Fe31.2at. %Pd alloy, Acta Materialia 54, 2006, pp. 1233- 1239.

Acknowledgments

Foremost, I would like to express my appreciation to my Doktorvater Prof. Dr. Lorenz Kienle for his continuous support, encouragement, and supervision during my journey. He is a constant source of enthusiasm and positive energy, which helped me greatly during many difficult periods. I thank him for introducing me to the reciprocal world and to the world of perfectionism.

I would like to thank also Deutsche Forschungsgemeinschaft (DFG) for the funding within the project SPP 1239.

I am particularly grateful to my friend and colleague, Dr. Ulrich Schürmann, for helping and guiding me in all possible ways during this journey. I would like to thank him for his priceless advice and suggestions, which helped me to improve the thesis in order for it to reach its present form. The discussions regarding different aspects of crystallography in general and TEM in particular were a learning experience for me.

I would like to also thank to Prof. Dr. Jeffrey McCord for his guidance during my Ph.D. and for his patience during the discussions when I was evaluating my results. The long hours spent in his office and in the lab really paid off in the end. I am also grateful to my friend, Onur Urs, and to Dr. Mikael Kustov for their time during our discussions, and for their in-depth knowledge of magnetism.

Furthermore, I am truley thankful to Prof. Dr. Eckhard Quandt, Dr. Christoph Bechtold, and Ahmed Zayed for their collaboration during my thesis. Without them, my research on shape memory alloys would not have been possible.

I would like to extend my gratitude to Viktor Hrkac, the friend with whom I started the Ph.D. mission and with whom I will possibly also complete it. I appreciate the time I spent with him in the office, in front of the microscope, and in der Blaschke.

A special thanks goes to Mrs. Viola Duppel and to Prof. Dr. Dr. A. Simon for their support with the TEM.

I would also like to acknowledge the past members of the Synthesis and Real Structure research group, Dr. Kiran Chakravadhanula and Dr. Andriy Lotnyk, for their valuable help in the research environment and for the introduction to TEM. Thank you for your great support.

I would also like to acknowledge Dr. Sebastian Fähler, Sandra Kaufmann-Weiß, and Robert Niemann from the IFW Dresden for giving me the opportunity for collaboration. Their exceptional ideas during our research and our fruitful discussions made this work possible. I would also like to thank Dr. Sven Hamann and Prof. Dr. Alfred Ludwig for their collaborative work and for their deep insight.

The KNMF at the Karsruhe Institute of Technology is also gratefully acknowledged, particularly Dr. Christian Kübel and Aaron Kobler for their time in front of the TEM.

I would also like to thank Christin Szillius and to Dr. Cristiane Zamponi for explaining to me and performing the sample preparation and characterization techniques from the beginning of my thesis research. I want to thank Katrin Brandenburg for the paperwork she has done for me during the past four years.

I will always be grateful to Mao Deng and Torben Dankwort for the wonderful time in the office with them. I am really thankful to Jason Worley for his English revision of my thesis.

I would also like to thank my friends in Kiel – Kadir Sentosun, Erdem Yarar, Emre Kizilkan, and Mert Kurttepeli – for providing stress-free Friday talks and delicious food. I would like to thank my other friends – Dr. Burcu Ögüt, Irmak Kocabas, Ekin Simsek, Cetin Akman, and Umut Sanli – for their mental support and enjoyable times.

Lastly, I would like to express my deepest love to my faculty and family members, particularly my girlfriend Anke Hollenberg for her encouragement and patience and my brother Bugra Erkartal for his support. I respect them for their love and care.

Selbstständigkeitserklärung

Der Verfasser erklärt, dass er die vorliegende Arbeit selbständig, ohne fremde Hilfe und ohne Benutzung anderer als der angegebenen Hilfsmittel angefertigt hat. Die aus fremden Quellen (einschließlich elektronischer Quellen) direkt oder indirekt übernommenen Gedanken sind ausnahmslos als solche kenntlich gemacht. Die Arbeit ist in gleicher oder ähnlicher Form oder auszugsweise im Rahmen einer anderen Prüfung noch nicht vorgelegt worden.